Improving the structural dynamics of slender beam-like structures

A Ph.D. thesis
by
Christopher Stuart Anderson

Supervised by Dr S. Eren Semercigil
and Dr Özden F. Turan

Victoria University of Technology
School of the Built Environment
Footscray Park Campus
Melbourne Victoria Australia

Summary and Significance

This project explores a novel technique for the vibration control of slender beam-like flexible structures. For this purpose, a new method is developed based on minor structural modifications. Three applications are chosen to demonstrate the new method. The first is the sensing wire oscillations of a hot-wire probe. The second application is the problem of tool chatter due to milling tool vibration, while the third application is the bending of an arrow as it is released from a bow. Although these applications sound quite different, they are in fact similar problems dynamically. They are related to the forced transverse structural vibrations of slender beams. For all applications, the external force input is of a broadband nature in frequency, similar to a white noise excitation. This force excites the slender beams into large amplitude resonance which in the case of a hot-wire probe, causes measurement inaccuracies, for milling, causes rough surface finish and slower machining times, whereas for archery causes reduced accuracy. The choice of the particular problems to demonstrate the effectiveness of the technique is due to the current research interests and available expertise in this area in the School of the Built Environment at Victoria University. However, the methods developed through the course of this research are general methods applicable to all other slender beam-like structures with step changes in cross sectional geometry, such as flexible robotic arms or power transmission cables.

ACKNOWLEDGMENTS

I would like to thank a number of people for their contribution, assistance and support.

Firstly to my parents, you made me who I am and for that I thank you. I thank my wife Fiona for her support and understanding. My brother, Jeremy also offered valuable support and experience after completing his own PhD.

My Grandfather-in-law, Ken, gave me inspiration and an enthusiastic thirst for knowledge. I knew him for 9 years before he passed away. I am grateful to have known him and thankful for his interest in my research.

Victoria University of Technology provided me a platform of resources, staff and experience for me to conduct my research. The Postgraduate studies unit provide valuable support to all postgraduate students. The staff within the School of the Built Environment were all extremely helpful.

I received an Australian Postgraduate Award scholarship to conduct my research and am grateful for this financial support.

Finally, I would like to sincerely thank my supervisors. Dr S. Eren Semercigil and Associate Professor Özden F. Turan were ideal supervisors. They gave me the direction I needed whilst allowing me the freedom I desired. Their experience and knowledge was an asset. I can only hope that some of it wore off onto me.

Christopher S. Anderson

TABLE OF CONTENTS

LIST OF TABLES

LIST OF FIGURES

Chapter 1

INTRODUCTION

This thesis investigates a new type of vibration control technique that involves imposing multiple coincident natural frequencies to reduce the excessive contribution of the fundamental mode, and hence, to reduce the excessive vibrations of slender beams. The technique proposed here is a unique one. No published results exist in the literature to control vibration in beams by imposing multiple coincident frequencies. Furthermore, the first of the three problems under analysis here, hot-wire probe sensing-wire vibration, has had little or no attempts made at reducing its undesirable oscillations.

1.1 Existing Forms of Vibration Control

Current vibration control methods can be classified broadly as: (i) vibration isolation, (ii) use of vibration absorbers, (iii) introduction of damping, and (iv) active vibration control. Alternatively, the first three can be grouped under the name of passive vibration control, indicating that there is no feedback between the controller and the system to be controlled.

Vibration isolation involves the introduction of an additional path between a structure and its mounting surface or vibration source. The resilient components are tuned to provide vibration isolation over a frequency range of concern. This approach is most commonly used to protect a particular component from an adjacent structure or to inhibit vibrations of a machine from reaching the structure it is mounted onto. In Hain et al. [1], the general procedure of using the vibration isolation technique is summarised.

Vibration absorption requires the attachment of an auxiliary oscillator to the system to be protected. Vibration absorbers are tuned to eliminate specific frequencies of concern, [2]. The auxiliary oscillator is generally tuned to have the same natural frequency as the system. Although vibration absorbers are effective in reducing vibration amplitude at their tuning frequency, they are ineffective for broadband excitation conditions, unless additional damping elements are incorporated in the absorber.

Dampers of various characteristics can be used for vibration reduction by converting energy from the system into heat or sound, which is dissipated. In Panossian [3], the existing methods of using damping for vibration reduction are summarised. An example is a shock absorber on a car suspension system. These methods are not adaptable to problems where physical constraints do not allow damping elements to be included in the geometry.

An active vibration control may involve a feedback mechanism that effectively varies the mass, stiffness and damping characteristics of the system to achieve the desired vibration reduction under different conditions. An alternative active control approach uses actuators to apply the required control forces [4]. The disadvantage of this method is that it may increase the size of the system. It is generally quite complex and, of course, expensive.

Again, this method is not appropriate for problems where constraints may prohibit secondary systems being attached. Also, problems where the component to be controlled is moving, present difficulties such as an arrow in free flight.

In summary, conventionally recognised control techniques may all be effective, provided that certain conditions are satisfied for their performance. Being able to attach additional components is a primary condition, which may be practically impossible to satisfy for a class of vibration control problems. This difficulty arises from the fact that there is simply no room for these components without interfering with the intended function. Examples of three such cases are specifically addressed in this thesis.

Local structural modification is a relatively new technique that has been gaining attention in recent years. This technique involves changing the structure so that its mass, stiffness and damping properties are redistributed locally to give improved vibration response characteristics [5]. Cha and Pierre [6], investigated the possibility of imposing nodes to the natural modes of beams. They achieved success by the addition of a chain of mass-spring oscillators to a beam. They showed that a node could be imposed at any point, for many natural mode shapes, depending on how many oscillators were attached. The effect of 'node' – 'anti-node' cancellation using the unit-rank method was more recently investigated by Mottershead and Lallement [7]. This work showed that slight structural modifications could yield coincident nodes and anti-nodes. This passive form of vibration control presents promise for vibration problems that cannot be controlled using the previously discussed more conventional methods.

The vibration control technique discussed in Chapter 2 has a similar approach to that of earlier local structural modification studies. However, quite different than other works, the objective here is to suppress the contribution of the fundamental mode of vibrations. Being the most flexible mode, fundamental mode is either the sole source of the problem, or it is a very significant contributor. Hence, its effective control is critically important. This technique is appropriate for problems where the displacement amplitude is of critical importance.

Chapter 2 of this thesis outlines the principles of the suggested control procedure. The following three chapters discuss applications to three different problems. Each of these three chapters are presented independently with their relevant literature review and conclusions.

Control of excessive vibrations of the sensor of a hot-wire probe is discussed in Chapter 3. Hot-wire anemometry is a flow measurement technique widely accepted in fields of both science and industry. A very thin wire, in the order of 5 μm diameter, is kept at a constant temperature at the CTA (Constant Temperature Anemometry) mode. Then, the cooling effect of the oncoming fluid flow is compensated by the accompanying instrumentation to maintain this constant temperature. The amount of compensation effort is calibrated and interpreted as the velocity of the flow. One implicit assumption in this procedure is that the sensing wire is stationary and the relative velocity of the flow with respect to the wire can be assumed to be the absolute velocity. Sensing wire, of course, is prone to excessive vibrations, which may lead to measurement errors.

A comprehensive study to analyse the dynamics of a sensing wire numerically, is presented first in Chapter 3. Laboratory observations are given to check the validity of the numerical predictions using a scaled-up prototype. Then, a procedure is described to manufacture the suggested designs. Flow measurements, comparisons and interpretations of possible measurements anomalies, which may arise when unsuitable sensor geometries are used for measurements, are given to conclude this application.

The second application presented in Chapter 4 is related to manufacturing. Design modifications in the form of an add-on solution, are suggested to enhance the chatter resistance of a cantilevered end milling cutting tool. Tool chatter in end milling is the self-excited resonance of the structure leading to excessive oscillations, accelerated tool wear, unacceptably high noise levels and poor surface finish of the work piece. Hence, efforts to reduce the proneness to chatter are well worthwhile. Both numerical predictions and laboratory observations are given to indicate the potential benefit of the control procedure.

The last application given in Chapter 5, is only of preliminary nature, and it applies to the bending vibrations of an arrow in free flight. Problem of concern here is the loss of accuracy at the target due to excessive oscillations. Numerical predictions to suggest control are discussed in Chapter 5. However, experimental verification is left for a future study to extend the work presented in this thesis.

Chapter 6 summarises the contribution of this thesis. Appendix A presents the purpose written Matlab® code used to perform the numerical investigations of this thesis. Examples and descriptions of how to use the software are given in this appendix.

Chapter 2

PROPOSED CONTROL TECHNIQUE

2.1 Introduction

This chapter discusses the vibration control technique developed in this thesis. To this end, numerical predictions and associated trends are presented to illustrate the effectiveness of the suggested procedures.

The inspiration for this study is credited to the work by Turan et al. [8]. It was shown that some slender beam geometries were less susceptible to large amplitude vibration under broadband excitation. It was also reported that the favourable geometries had relatively close first and second natural frequencies. Further investigations by the candidate demonstrated the reasons for this trend [9]. The reason why some slender beams are less susceptible to excessive vibrations can be related to the particular shape that a beam assumes when excited at a resonance frequency. Figure 2.1(b) shows the first two mode shapes of the fixed-fixed, uniform beam shown in Figure 2.1(a). The second resonance mode has a point of zero amplitude in the mid-span, where the first resonance mode has a point of maximum amplitude. When the first two natural frequencies are close, or coincident, these two mode shapes should have equal opportunity to contribute to the resulting response of the beam.

In Figure 2.1(b), the dashed line represents the shape obtained by spatially averaging the first two mode shapes, assuming that both have an identical contribution. The resulting shape has a node at about 1/3 distance from one end, on the side where the second mode happens to be out-of-phase with the first mode. The actual phase difference between the two modes is immaterial, due to the particular shape of the second mode. This node, however, is unstable, since the value of the second natural frequency will always be somewhat larger than that of the first natural frequency. As a result, the node will travel towards the middle, and then, to the other side of the beam, before it turns back to assume the location shown in the figure. A structure with slightly different natural frequencies will exhibit a beating phenomenon.

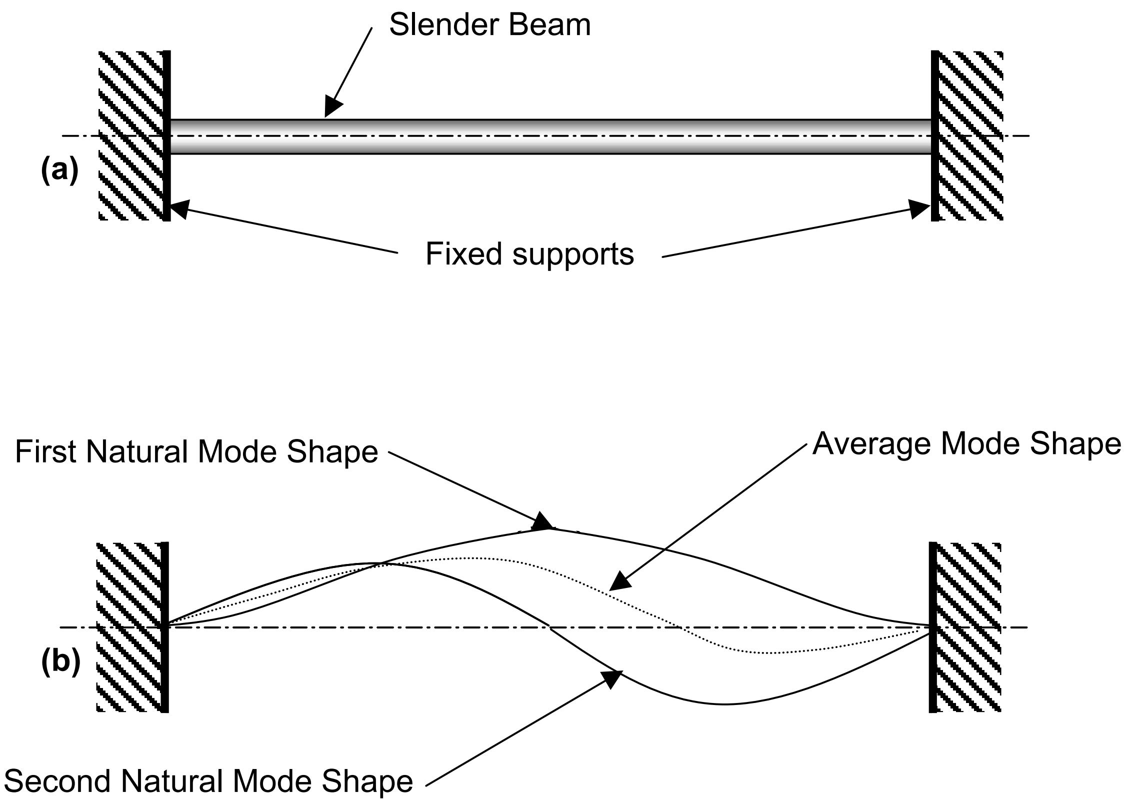

Figure 2.1. **(a)** The fixed-fixed beam model, and **(b)** its first two bending mode shapes.

If a beam is designed to have virtually coincident natural frequencies of the first two modes, then neither of the two natural modes will be able to establish themselves. For such a design, the node of the second mode will effectively suppress the response of the more critical fundamental mode.

In the argument above, it is possible to include fixed-free geometries such as those of a drill bit or a milling cutter, as illustrated in Figure 2.2, by removing the right hand constraint. The average shape in Figure 2.2(b), again represents the strong interference of the out-of-phase characteristics of the second mode on the in-phase first mode. Such interference may result in reduced magnitudes of the beam oscillations as compared to the case where the first mode of the vibrations is free to dominate the dynamic response.

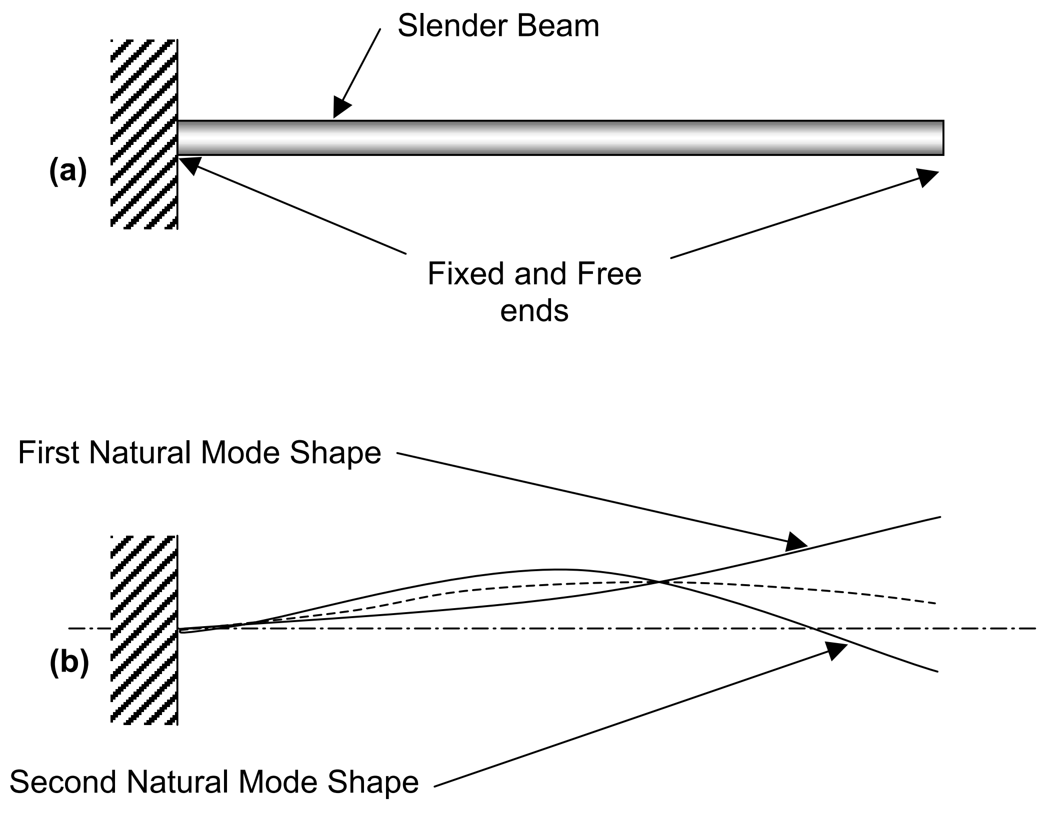

Figure 2.2. **(a)** The fixed-free beam model, and **(b)** its first two bending mode shapes.

The argument of the preceding paragraph can also be extended to free-free geometries, such as that of an arrow upon release from an archer's bow. The average mode shape in Figure 2.3(b), represents the suppression effect of the second bending mode on the first one.

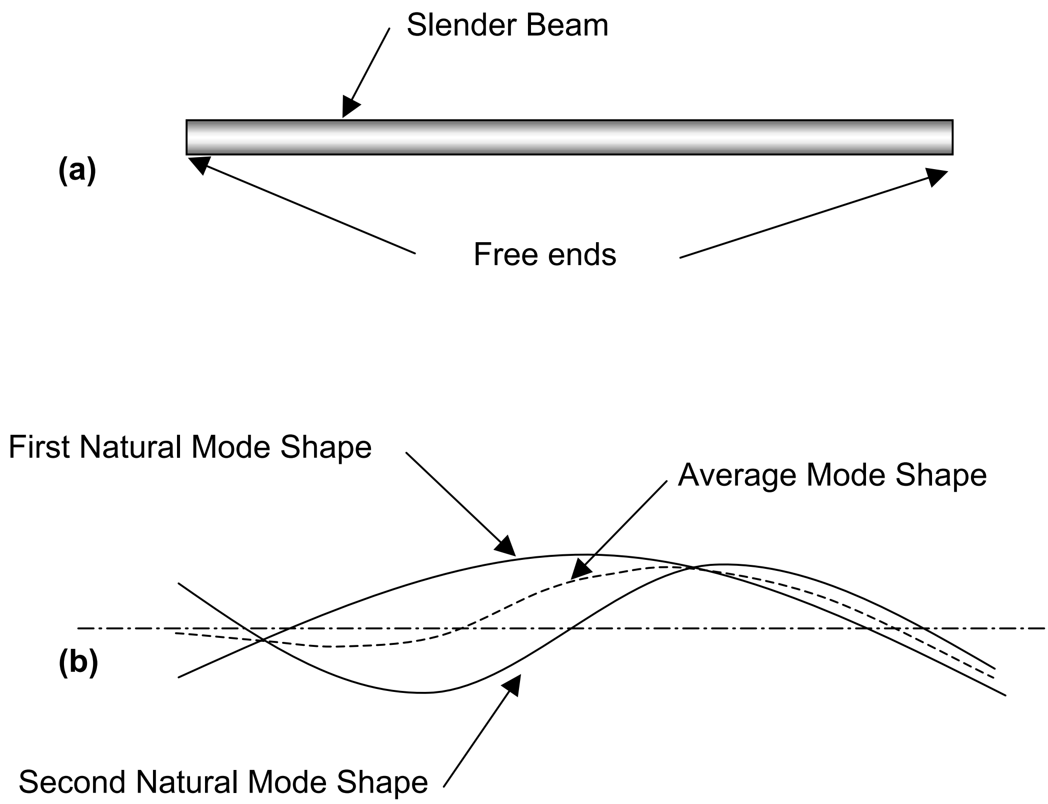

Figure 2.3. **(a)** The free-free beam model, and **(b)** its first two bending mode shapes.

For all three cases, the second mode shape has a nodal point either at or close to the largest amplitude of the first mode. Hence, in all three cases, when the two mode shapes attempt to coexist, reduction of vibration amplitude should be possible.

The control technique suggested in this section may be achieved by modifying the problem geometries locally, instead of incorporating additional control structures. As such, there are some significant advantages. Control may be achieved without adding mass. Control may be possible for a variety of excitation conditions that involve a predominant displacement in the fundamental mode. Finally, the suggested control may be the only form of vibration control possible for problems where the constraints of the system disallow existing forms of vibration control to be implemented. Applications presented in Chapters 3 to 5 are examples of such problems.

The next section in this chapter presents the numerical analysis procedure for a number of different beam geometries. Section 2.3 discusses scaling methods for the presented results and section 2.4 outlines conclusions drawn from this chapter. The first practical application investigated in this thesis is sensing wire vibrations of hot-wire probes, as discussed in Chapter 3. Hence, the beam dimensions discussed in this chapter relate to the dimensions of these sensing wires. Larger scale applications, such as those of milling cutters and arrows, are discussed in Chapters 4 and 5, respectively.

2.2 Numerical Analysis of Slender Beam Geometries

To illustrate the effectiveness of the control technique introduced in the previous section, finite element predictions are presented next. The numerical model for a beam having fixed-fixed boundary conditions is shown in Figure 2.4. In this figure, the middle section has d and L for diameter and length, respectively; whereas d_g, L_g and L_o represent respectively the diameter and length of the thicker ends and the total length. The beams were modelled numerically using standard Euler-Bernoulli finite beam elements in Matlab® [10]. These classical elements used for thin beam theory disregard the effects of rotary inertia and shear deformation and have a single node at each end. Thirty beam elements were used across the beam length, a sufficient number to provide a smooth representation of the first five natural mode shapes of interest. The solution to the resulting eigenvalue problem provided the natural frequencies and the mode shapes of the beam geometry.

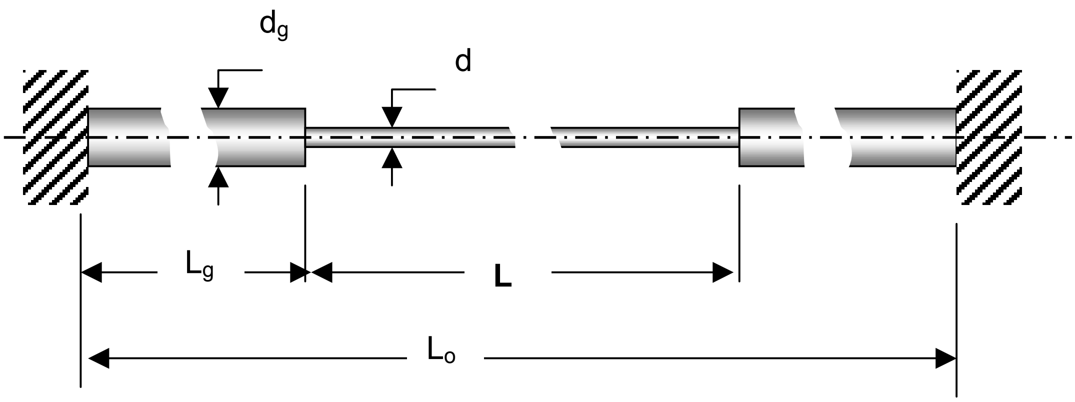

Figure 2.4. Schematic representation of the numerical beam model used for the fixed-fixed beam example.

Here, the investigation of beam geometries has been limited to three different cross sections as shown in Figure 2.4, and to the three boundary conditions shown in Figures 2.1 to 2.3. Therefore, there are 10 different cases, as shown schematically in Figure 2.5. Uniform cross section beams are not included here, since they have well separated natural frequencies.

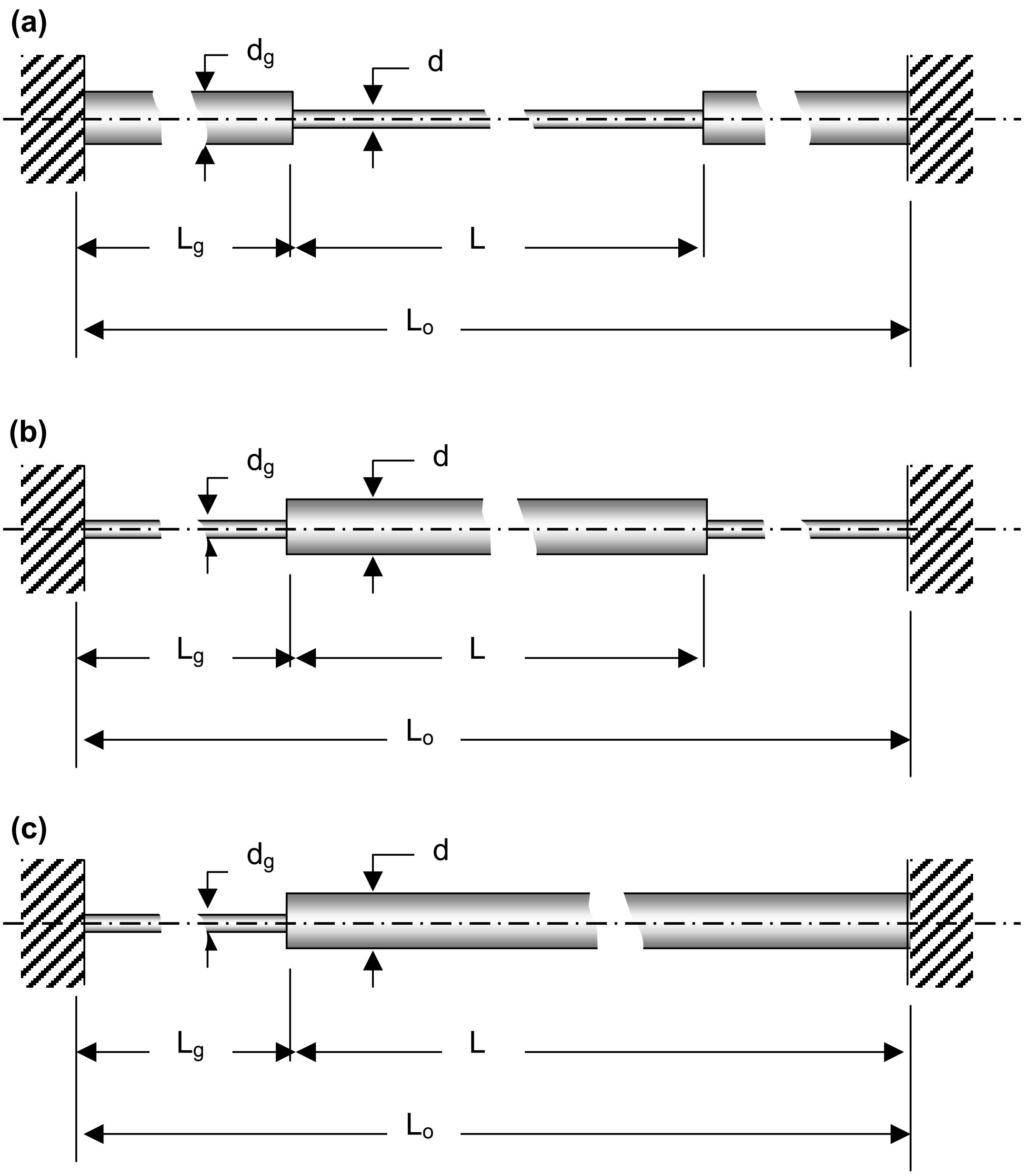

Figure 2.5. Ten different types of three basic beam geometries for **(a)**, **(b)** and **(c)** fixed-fixed; **(d)**, **(e)**, **(f)** and **(g)** free-free; and **(h)**, **(i)**, and **(j)** fixed-free boundary conditions. (Continued over page).

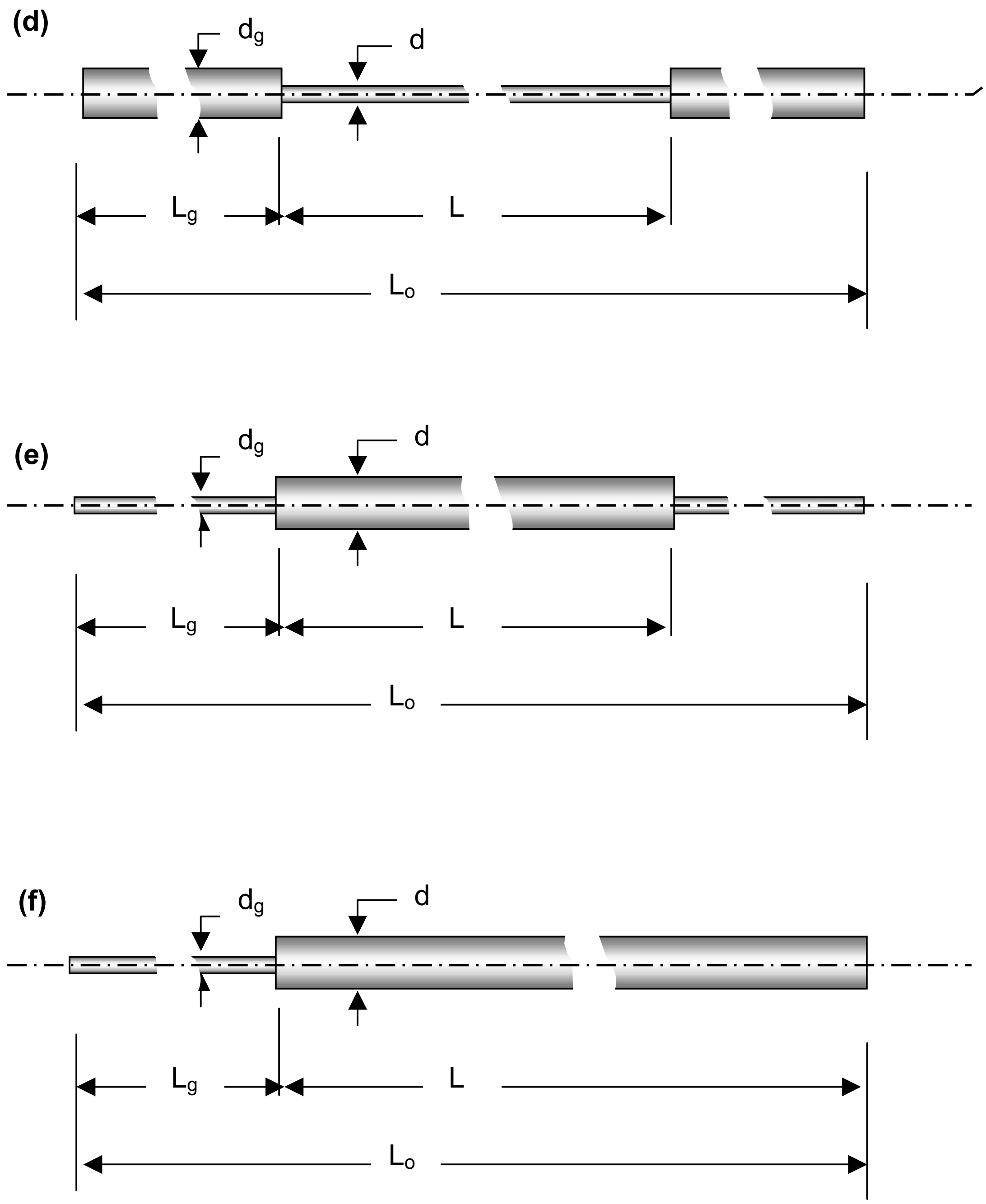

Figure 2.5. Ten different types of three basic beam geometries for **(a)**, **(b)** and **(c)** fixed-fixed; **(d)**, **(e)**, **(f)** and **(g)** free-free; and **(h)**, **(i)**, and **(j)** fixed-free boundary conditions. (Continued over page).

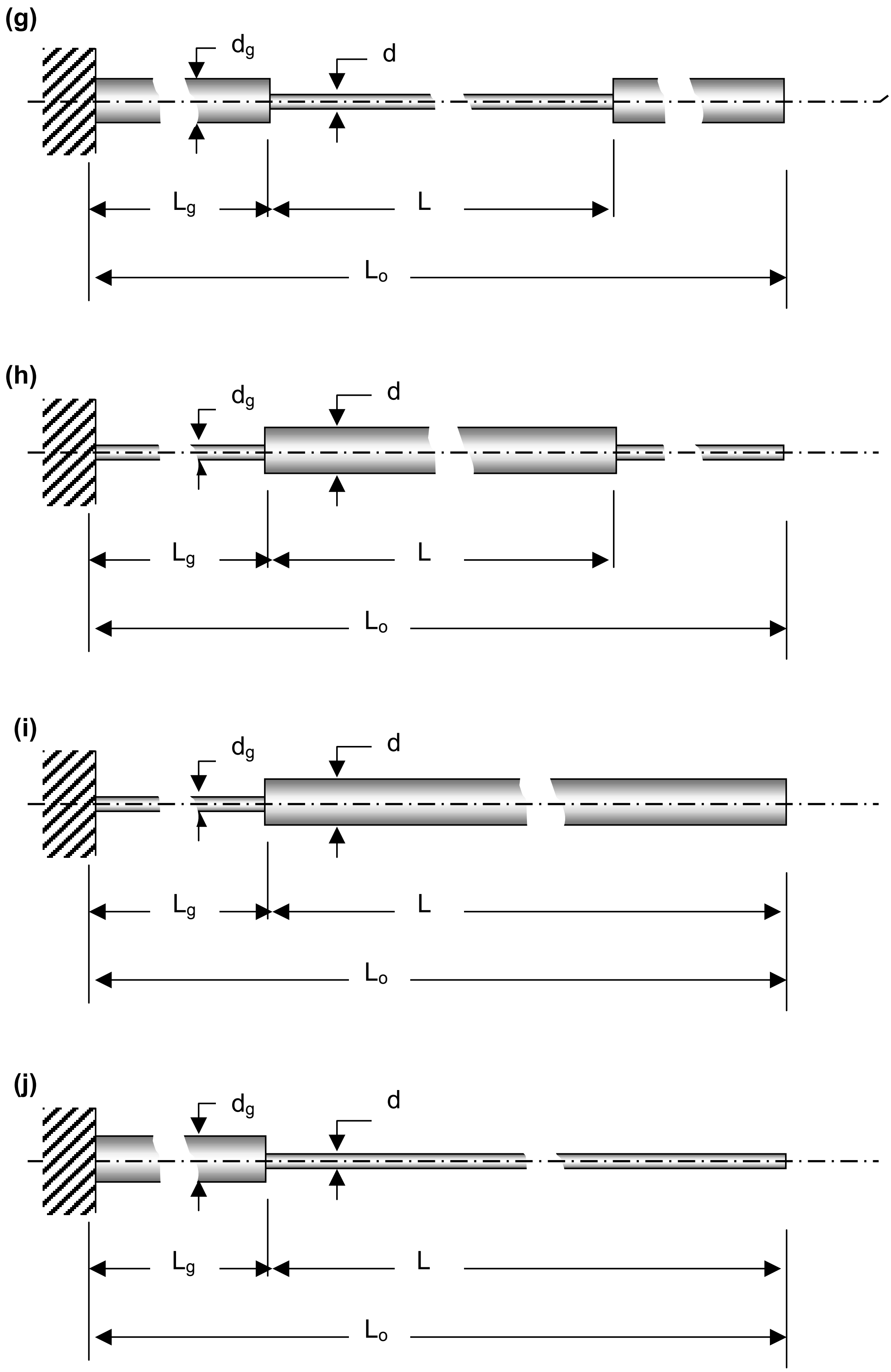

Figure 2.5. Ten different types of three basic beam geometries for **(a)**, **(b)** and **(c)** fixed-fixed; **(d)**, **(e)**, **(f)** and **(g)** free-free; and **(h)**, **(i)**, and **(j)** fixed-free boundary conditions.

For each of the types shown in Figure 2.5, the ratio of L_g to L was varied from 0 to 4. An L_g/L of zero corresponds to the entire length consisting of diameter, d; whereas an L_g/L of 4 corresponds to L_g being four times as large as L. Also, the effect of relative slenderness was investigated by varying the end diameter d_g and the overall length L_o. The following figures show how these design parameters can modify the natural frequency separation.

Figure 2.6 shows how the natural frequency separation changes with L_g/L for a fixed-fixed beam, having d_g=30μm, L_o=3mm and d=5μm, as illustrated in Figure 2.5(a). The thick ends are gold, for better electrical conductivity, while the middle section is tungsten with Young's modulus of elasticity values of 60 GPa and 407 GPa, respectively. This geometry has been chosen as an example, since it represents a hot-wire probe sensing wire, the application discussed in Chapter 3.

In Figure 2.6, the vertical axis is the frequency in kHz, while the horizontal axis is the ratio of the end length to the middle (sensitive) length, L_g/L. The blue line represents the first natural frequency, while the cyan, green, yellow and red lines represent the second, third, fourth and fifth natural frequencies, respectively. Any vertical line drawn on the figure would indicate the first five natural frequencies, at the intersection with the five curves, for a single geometry. Since the total length is fixed at 3mm, the effect of moving from the left to the right on the horizontal axis is to increase the end length while decreasing the sensitive length, resulting in an increase in L_g/L. An L_g/L of 1 corresponds to end and sensitive lengths of 1mm. An L_g/L of zero represents a uniform sensing wire of 3 mm in length where the length of the L_g section has been reduced to zero so that the total wire length consists solely of the L section.

Inspection of Figure 2.6 reveals that the first and second natural frequencies, corresponding to the blue and cyan lines, can be pushed relatively close, around L_g/L equal to one. Furthermore, geometries could be chosen to have the third natural frequency either in close proximity or far away from the second natural frequency.

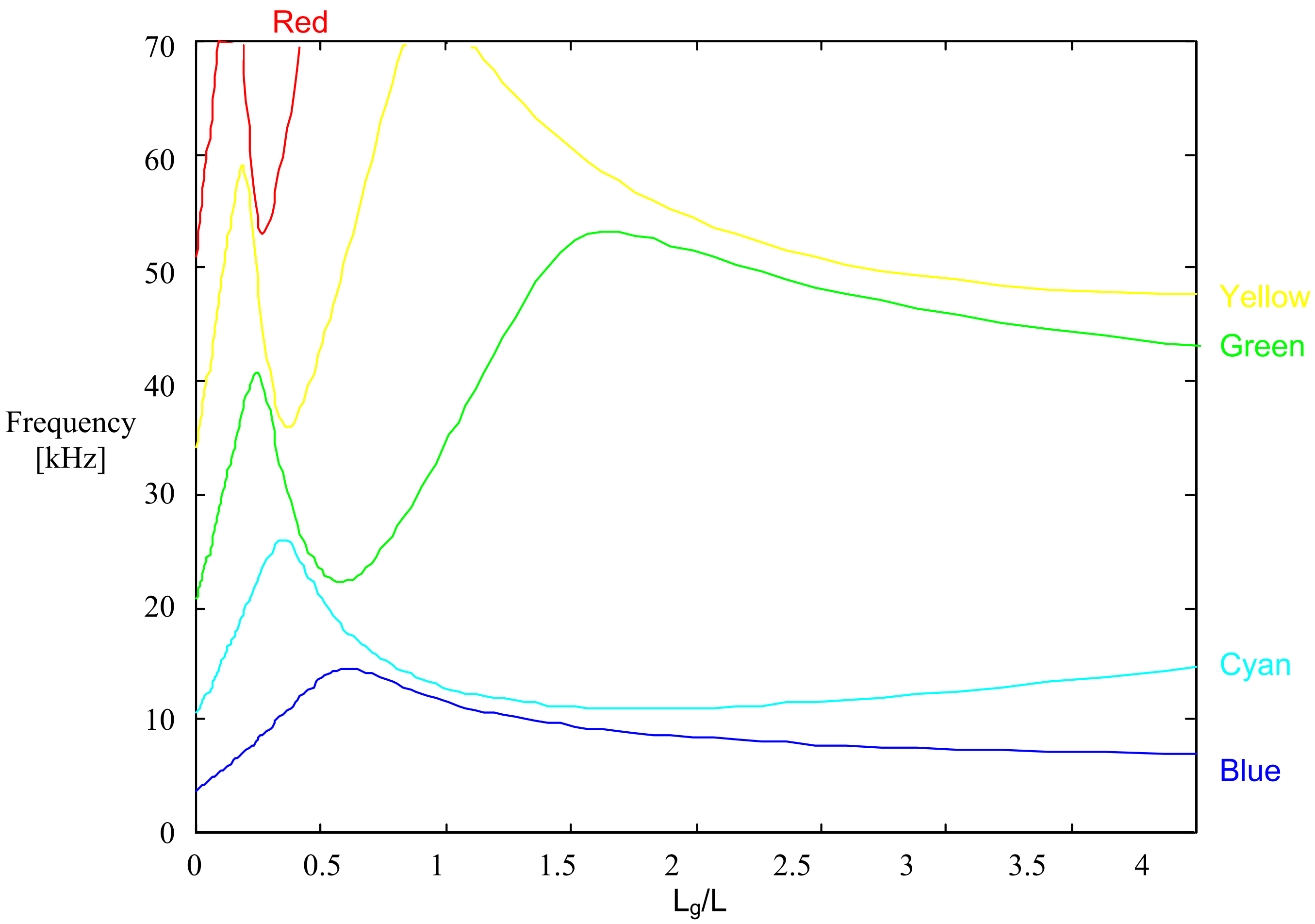

Figure 2.6. Frequency against L_g/L for a probe having a total length, L_o, of 3mm, end diameter, d_g, of 30μm and a sensitive diameter, d, of 5μm. The blue line represents the first natural frequency. The cyan, green, yellow and red lines represent the second, third, fourth and fifth natural frequencies, respectively.

Figure 2.7 shows the frequency plots for a range of total lengths and end diameters for the same geometry as in Figure 2.6. The axes, which are the same as in Figure 2.6, are not displayed here due to space limitations. When the plots are displayed collectively in this manner, trends can be identified. Firstly, increasing the overall length, L_o, has the effect of reducing the relative stiffness of the wire, giving a noticeable reduction in the magnitudes of the natural frequencies, moving from the left to the right in a row. Secondly, decreasing the end diameter, d_g, has the effect of decreasing the relative stiffness, again clearly visible moving down in a column. The bottom row, for d_g of 15 μm, has no region where the first and second natural frequencies are particularly close. Here, closeness is assumed to be within 10%. Therefore, it is expected that these geometries would be susceptible to large amplitude vibration. The row corresponding to a d_g of 20 μm shows promising geometries for L_g/L of between 1 and 2, for overall lengths of 3 and 3.5 mm. All the other subplots shown have promising regions of L_g/L between 1 and 2.

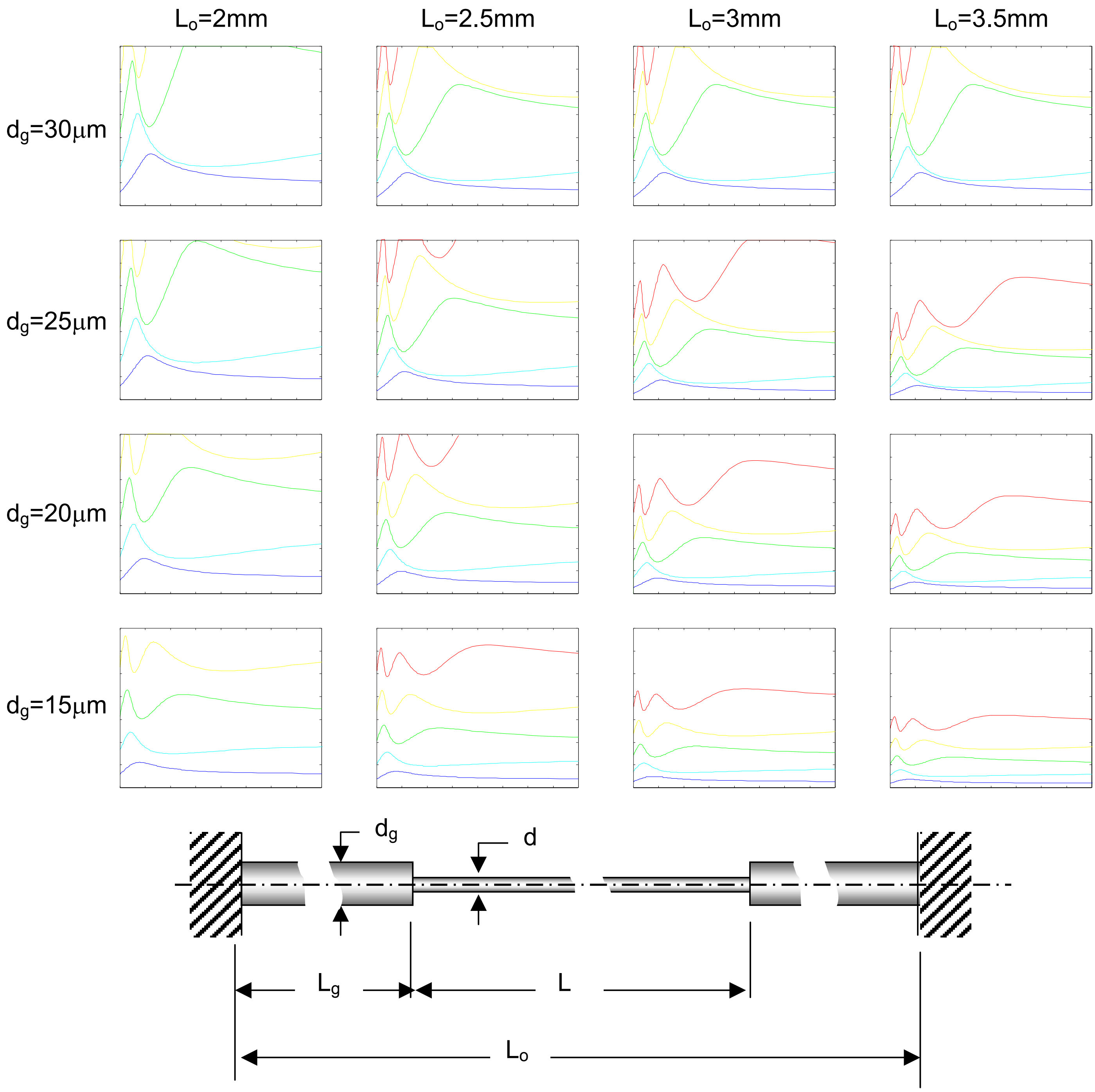

Figure 2.7. Frequency plots for fixed-fixed beam type, Figure 2.5(a), repeated here for clarity. The vertical and horizontal axes of each subplot are the same as in Figure 2.6. Each column has a different total wire length, and each row has a different end diameter, as shown.

Similar frequency plots can be generated for the other nine beam types presented in Figure 2.5. Here, Figures 2.8 to 2.16 correspond to beam types (b) to (j), respectively. The frequency plots in Figure 2.8 show regions were the third and fourth modes are pushed close together, such as for L_g/L of 1 with L_o=2.5 mm and d_g=30 μm, but not the first and second. Therefore, beam type (b) is not a promising geometry. The frequency plots in Figure 2.9 show more promising results towards the upper right hand corner, and therefore, a stepped beam of type (c) would benefit from having a large diameter ratio and a larger overall length with L_g/L of around 0.5.

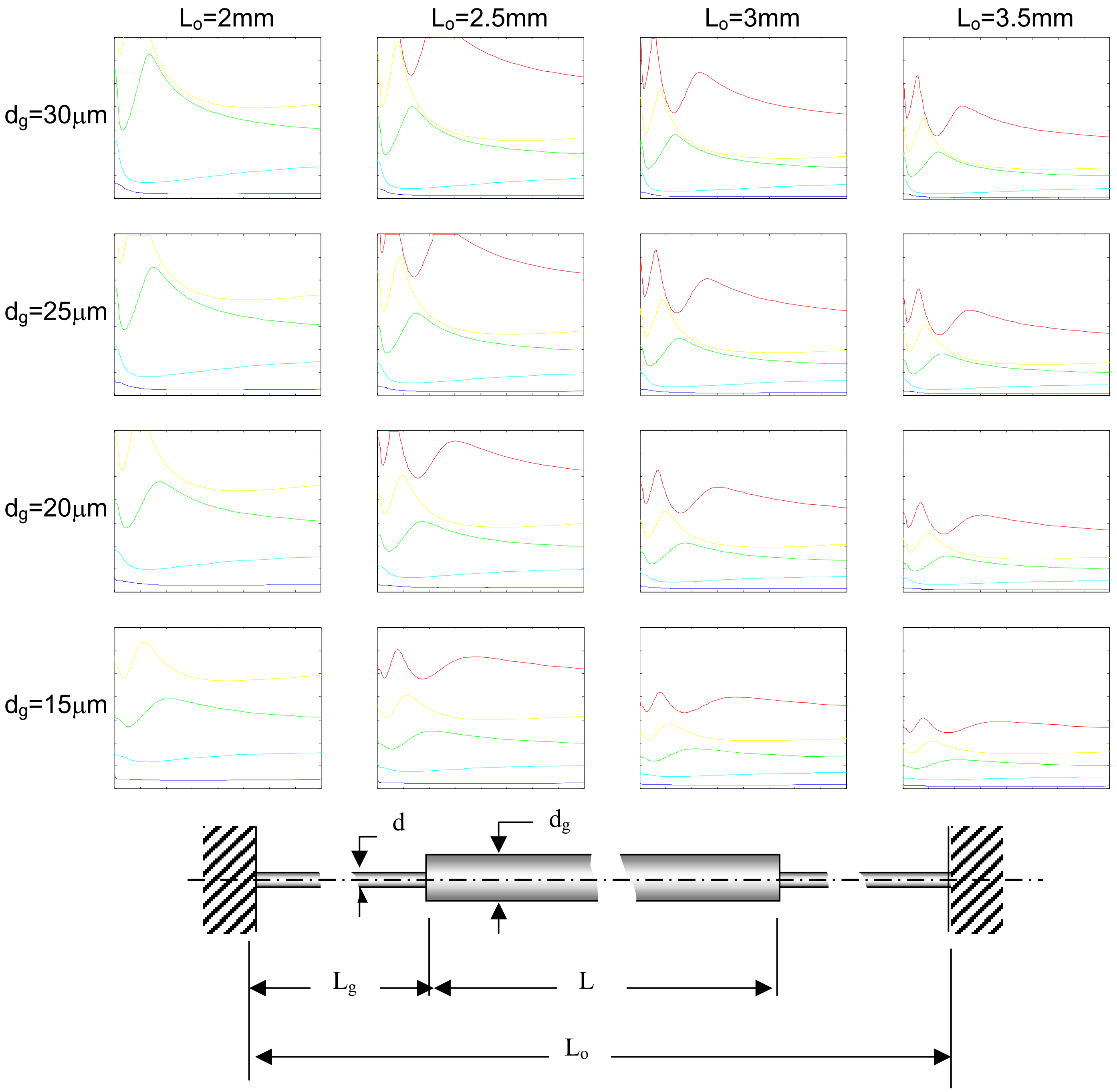

Figure 2.8. Frequency plots for the beam type shown in Figure 2.5(b), repeated here for clarity. The axes are the same as in Figure 2.6.

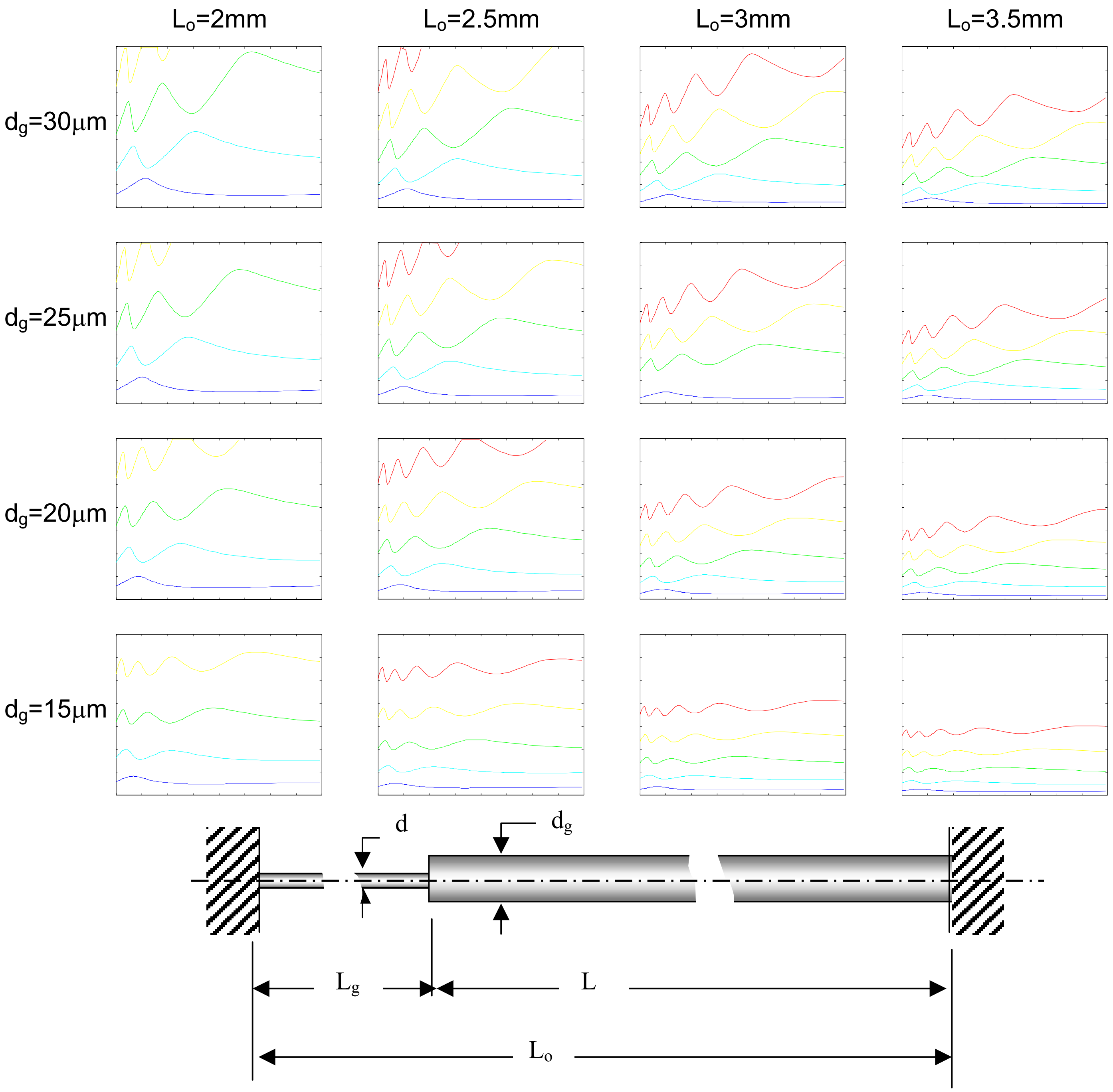

Figure 2.9. Frequency plots for beam type (c) as shown in Figure 2.5(c).

Figure 2.10 is the first of the free-free geometries. For these free-free cases, the first two natural frequencies calculated by the solution of the eigenvalue problem are zero, corresponding to rigid body modes where the beam is translating or rotating about an axis. This is simply the result of having no boundary constraints and can safely be excluded. Hence, for these free-free cases, the first natural bending frequency, corresponding to the third eigenvalue, is shown in green. For this geometry, there are no promising results presented.

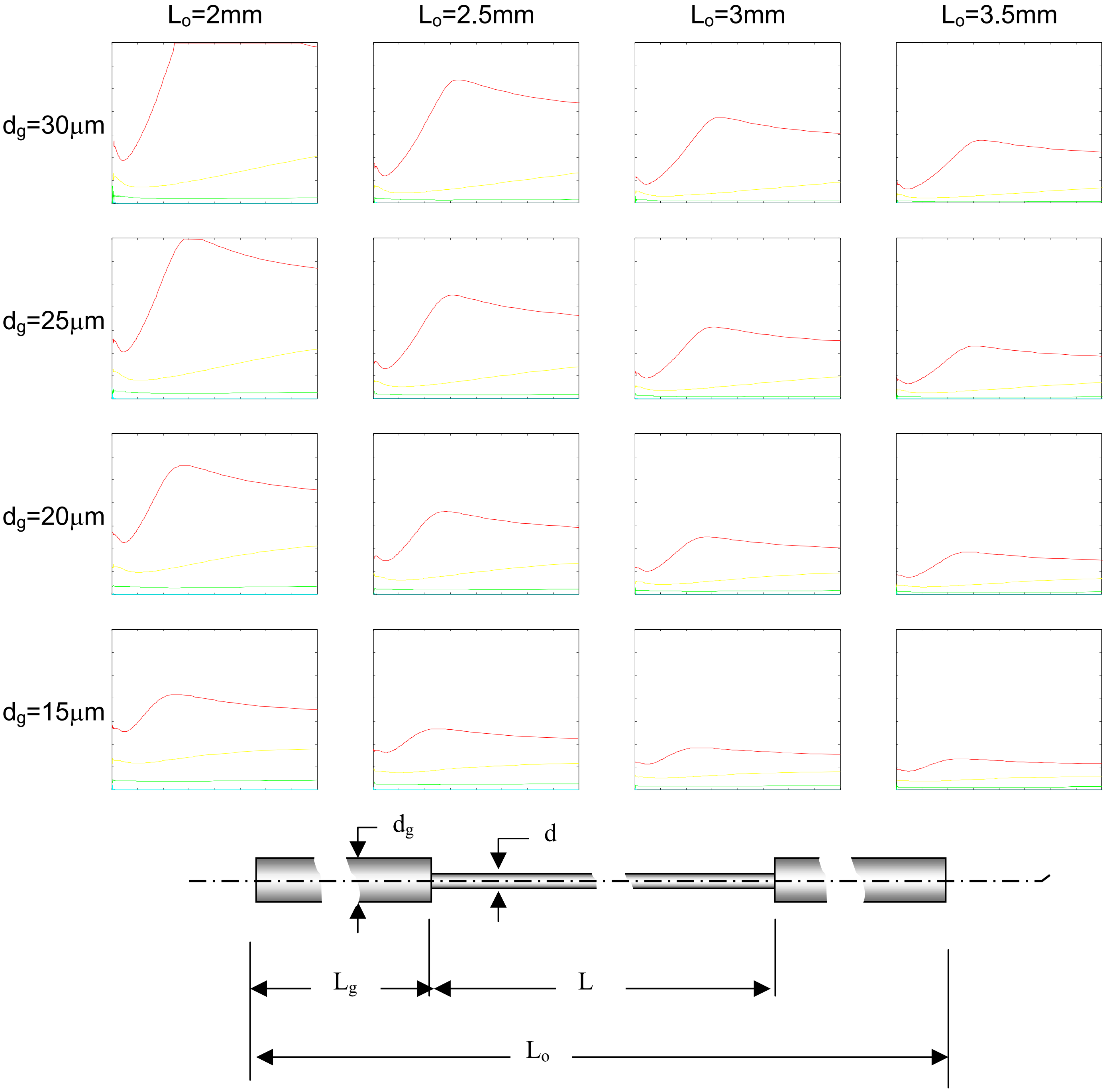

Figure 2.10. Frequency plots for beam type (d) from Figure 2.5(d).

Figure 2.11 for beam type (e) does, however, show some promise, in the top left hand corner for $L_g/L=0.5$, $d_g=30\mu m$ and $L_o=2mm$. Hence, a free-free beam having this stepped geometry would be less susceptible to large amplitude vibration. Modifying the overall length gives no apparent benefit here. In Figure 2.12, beam type (f), also shows some promising geometries, this time in the top right hand corner for L_g/L of around 3.5, suggesting that a larger overall length along with a large diameter ratio is expected to be beneficial.

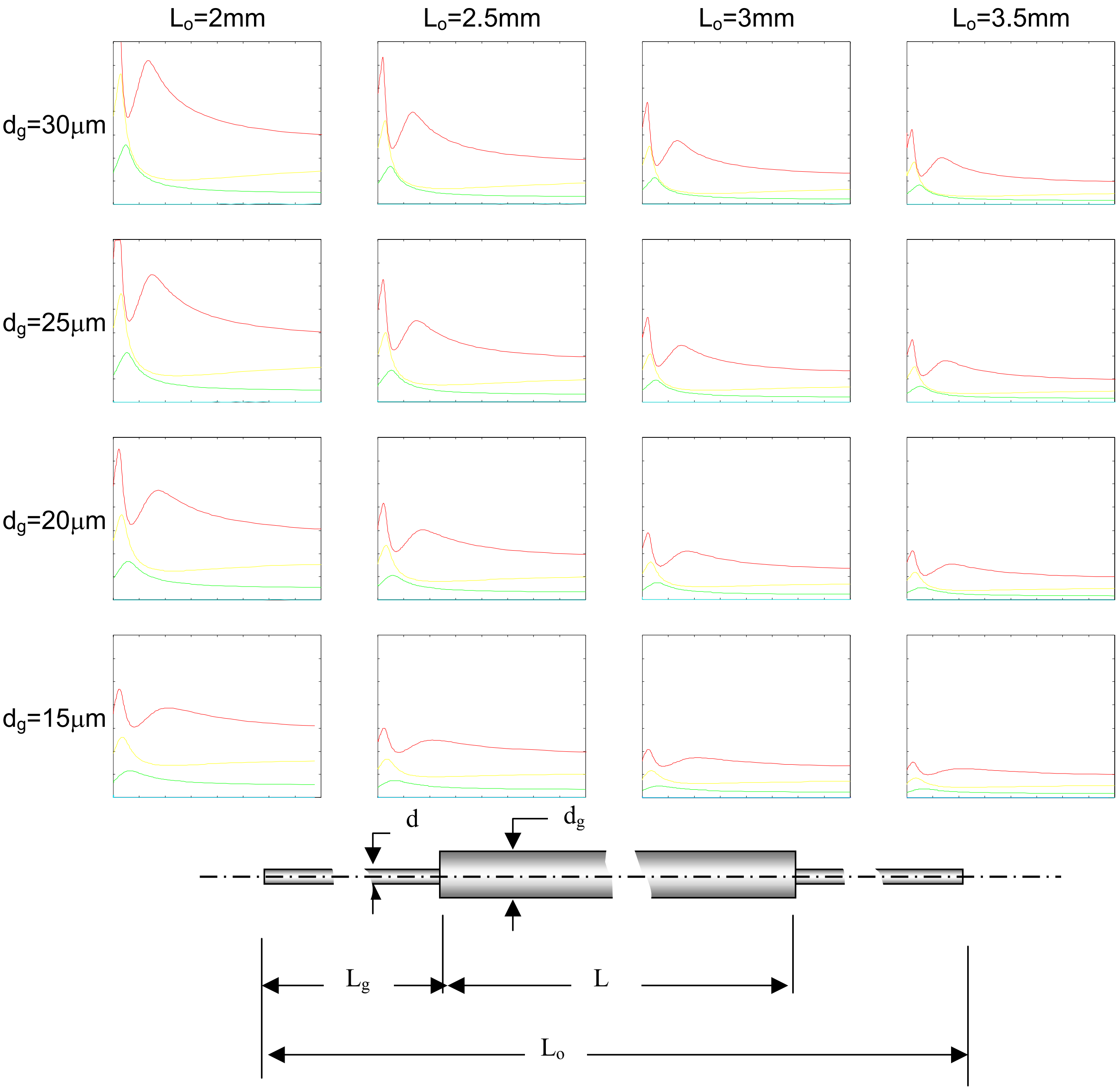

Figure 2.11. Frequency plots for the beam type (e) as shown in Figure 2.5(e).

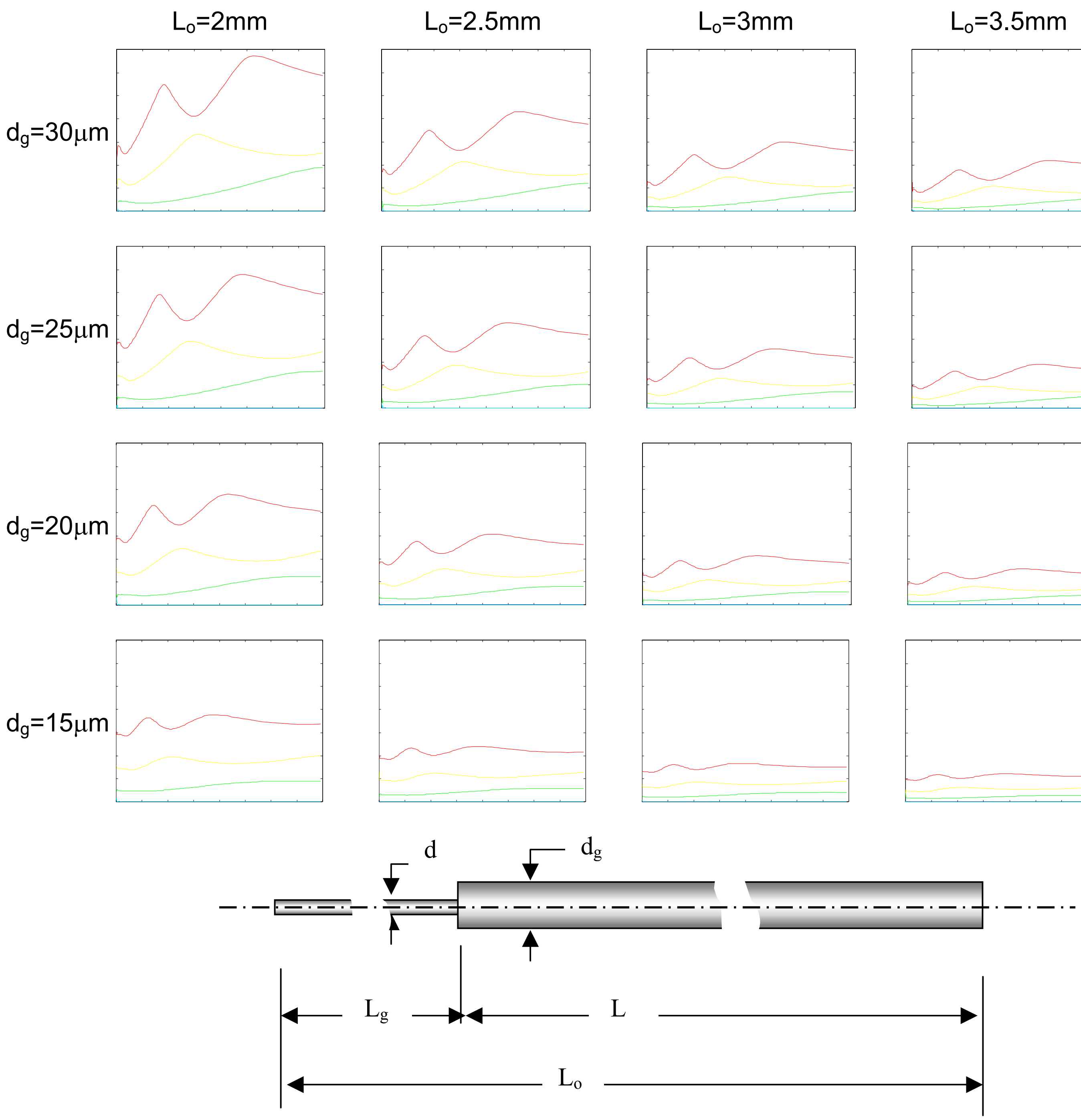

Figure 2.12. Frequency plots for beam type (f) from Figure 2.5(f).

Figure 2.13, the first of the fixed-free geometries, shows no regions where the first and second natural frequencies are close. Similarly, for Figures 2.14 and 2.15, no promising geometries are present. These results are included here for completeness. However, Figure 2.16, for beam type (j) does show some promising geometries, for L_g/L between 1.5 and 2.5, in the top two rows of the frequency plots corresponding to d_g values of 30 and 25 μm. This trend suggests that large step changes in the cross sectional diameters will be of benefit, for any overall length.

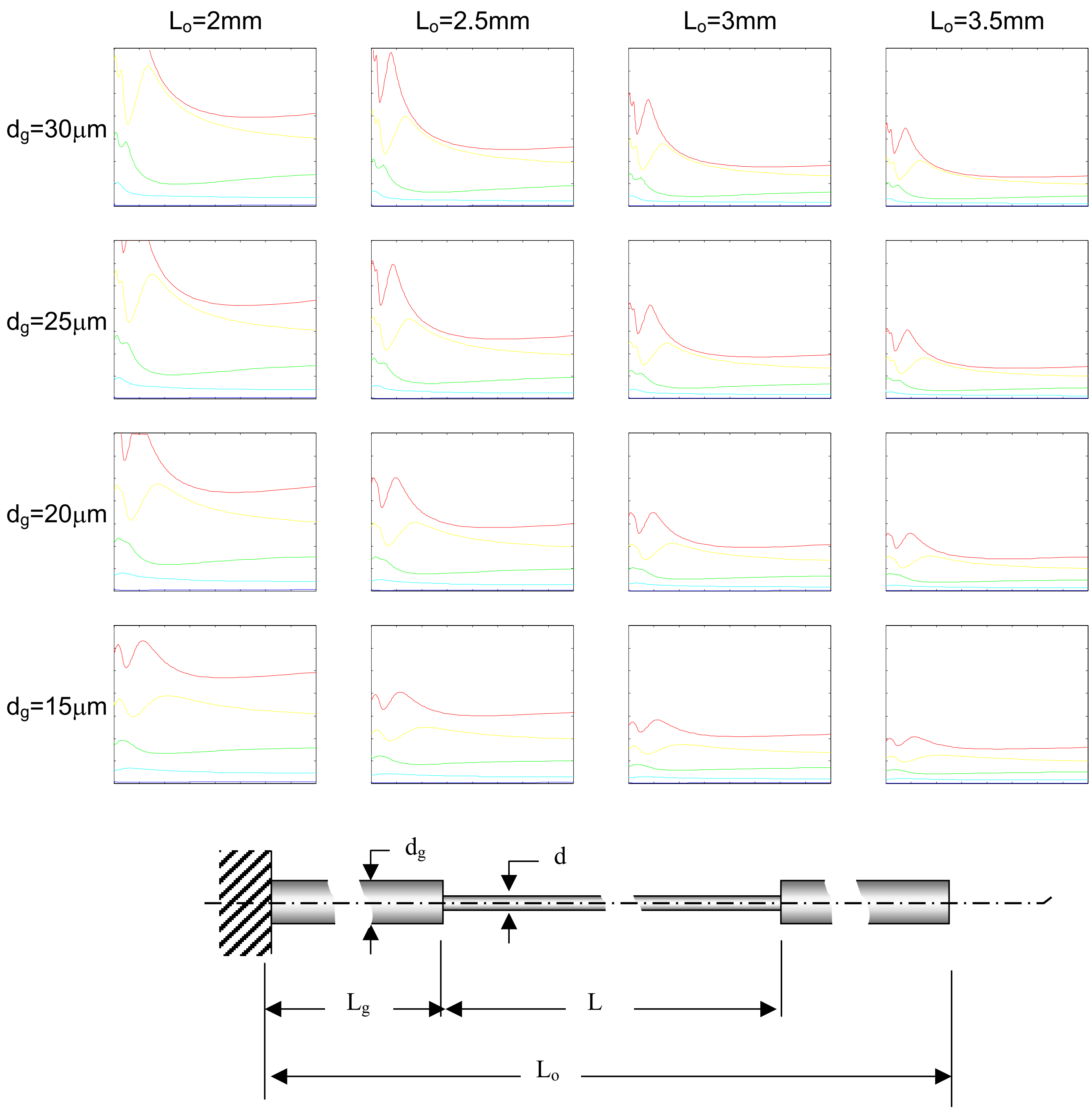

Figure 2.13. Frequency plots for beam type (g) in Figure 2.5(g).

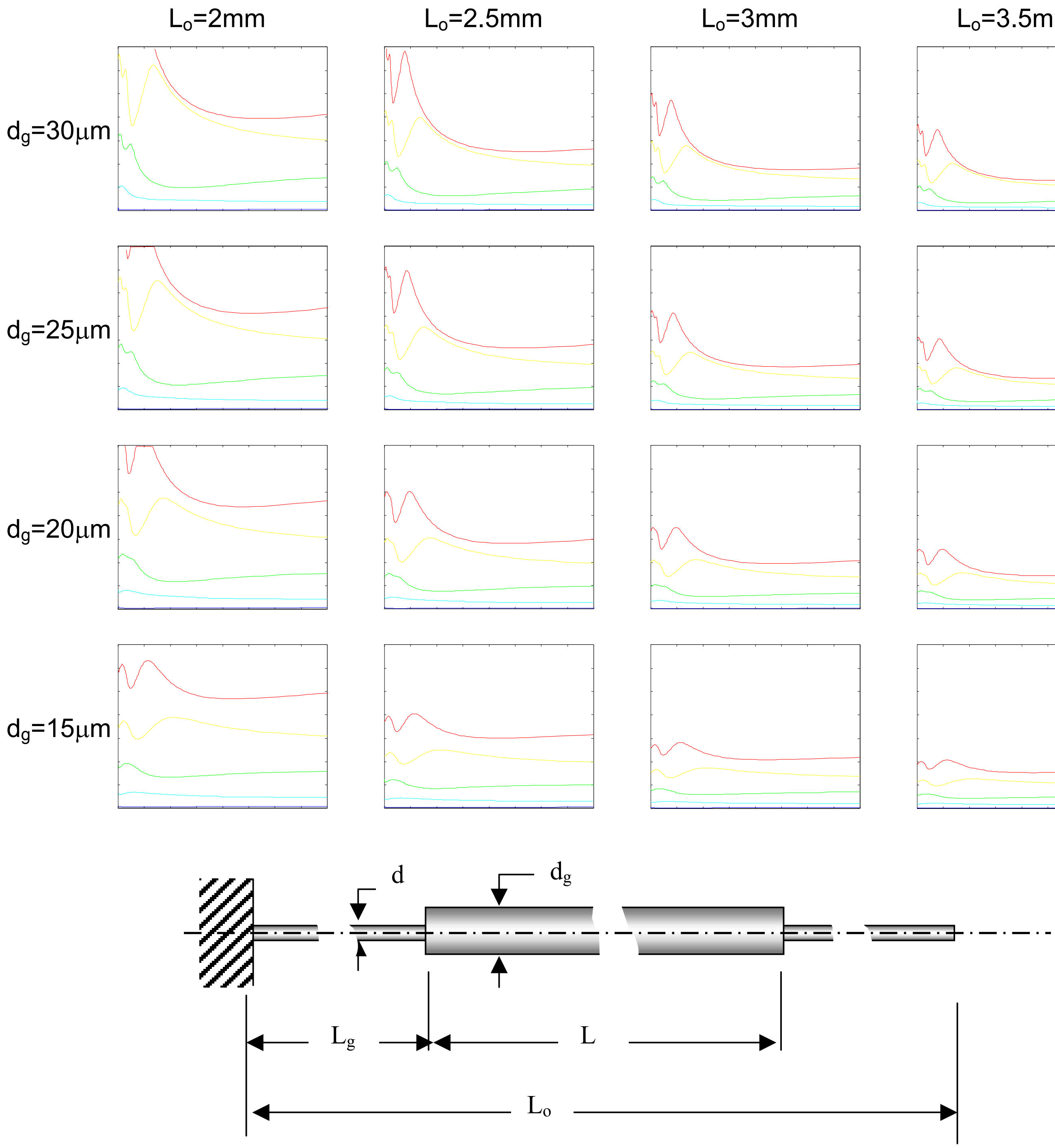

Figure 2.14. Frequency plots for beam type (h) as shown in Figure 2.5(h).

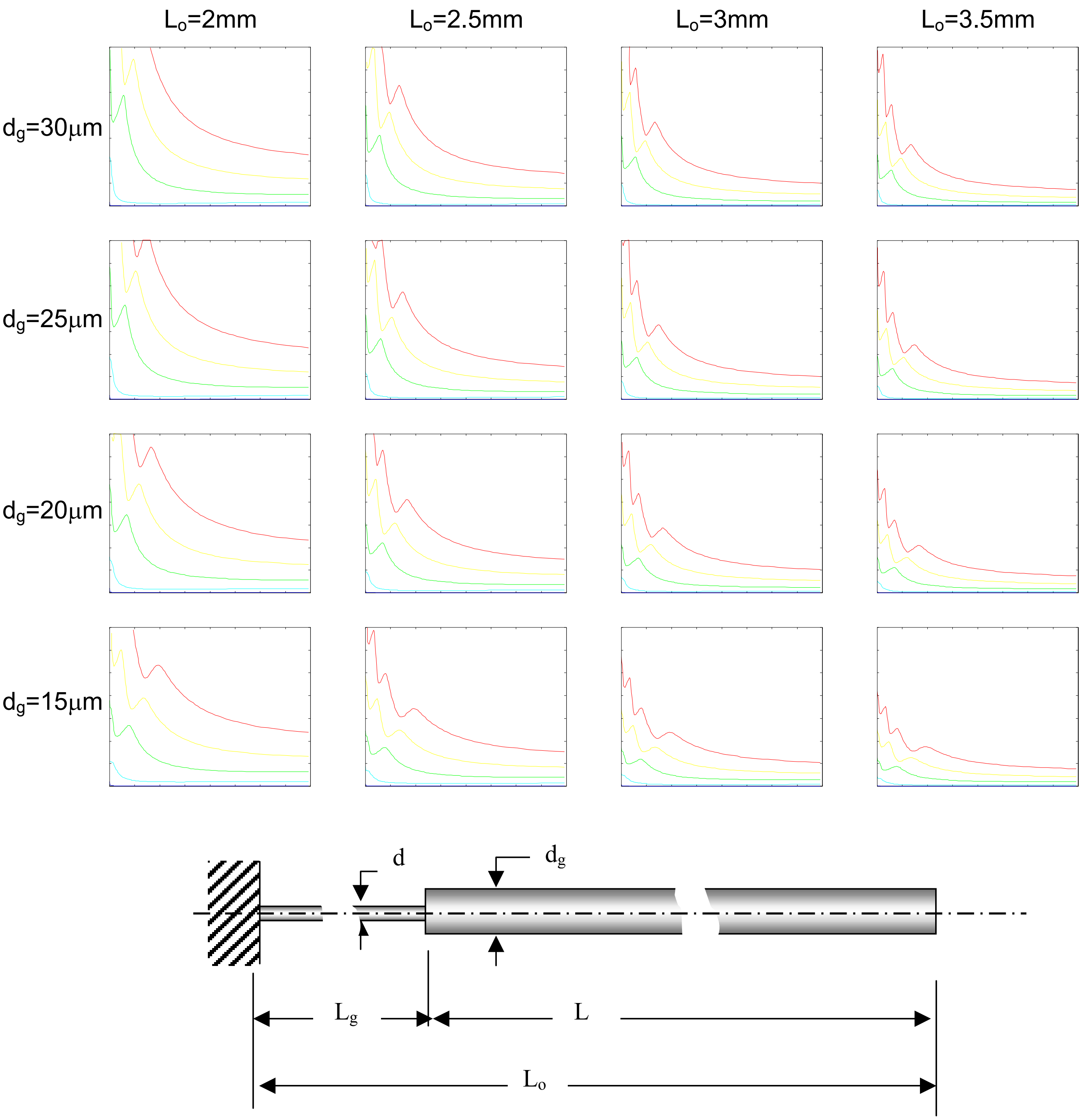

Figure 2.15. Frequency plots for beam type (i) as shown in Figure 2.5(j).

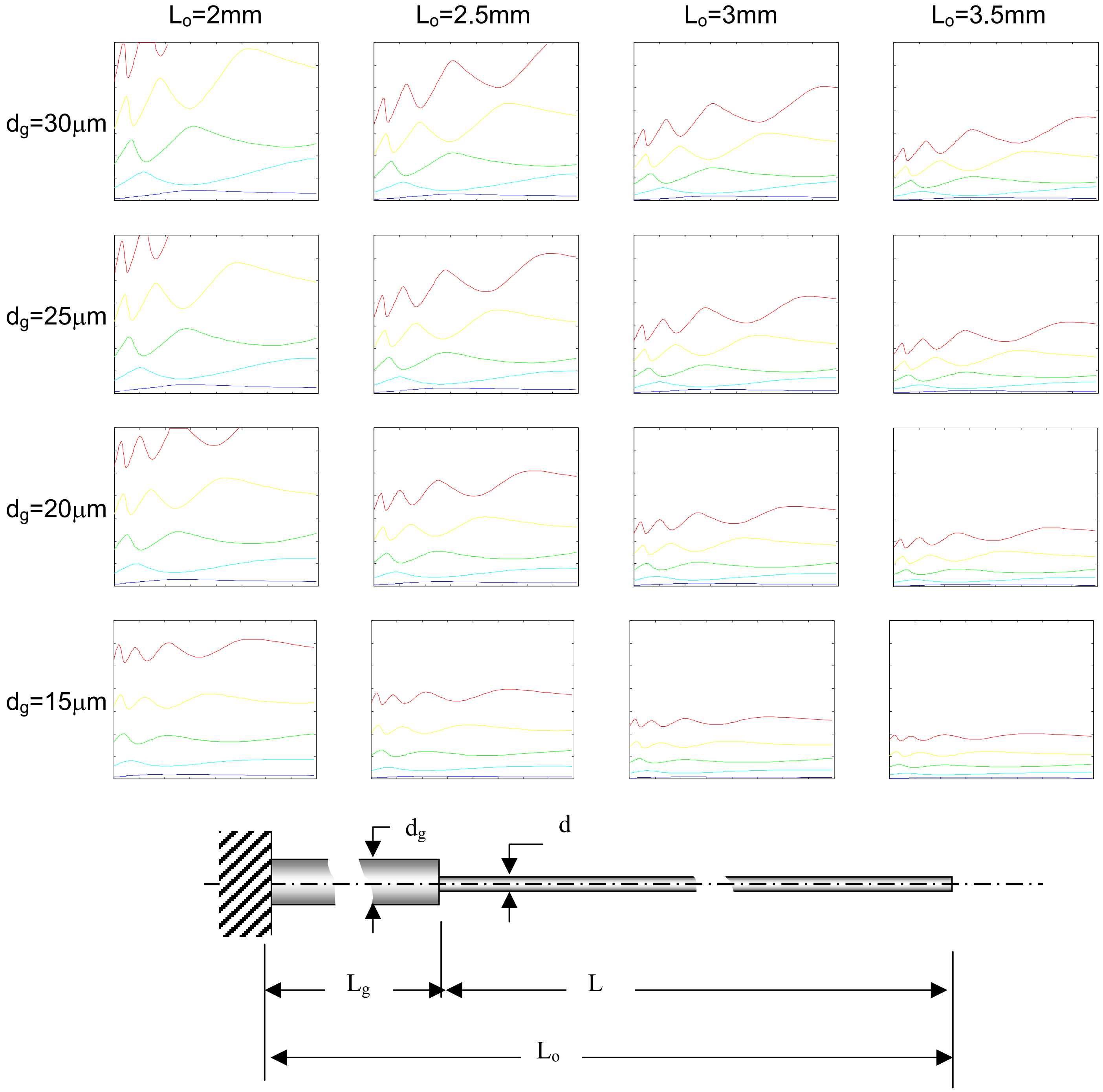

Figure 2.16. Frequency plots for beam type (j) as shown in Figure 2.5(j).

Examination of Figures 2.7 to 2.16 reveals similarities in the frequency patterns. In any of these figures, moving down in a column seems to repeat the characteristic shapes of the natural frequency curves, only to ‘push’ them down to lower values. On the other hand, moving from left to right in a row, seems to both ‘lower’ the curves and ‘zoom out’ to present a wider view. These similarities lead to the search for scaling parameters. The similarities, along with attempts to establish scaling parameters, are discussed in the next section. Scaling parameters would reduce the need to generate so many plots in the early stages of the analysis, saving time.

2.3 Discussion of Scaling in Frequency Plots

The following discussion is based on fixed-fixed beams, only. However, it also applies to the other two boundary conditions. Hence, taking beam (a) of Figure 2.5 as an example, Figure 2.7 shows a selection of frequency against L_g/L plots for different hot-wire probe geometries. The individual plots in Figure 2.7 are arranged in such a way that each plot represents a small change in parameters from those of its neighbours. The plots in the top left and bottom right do not, at first glance, appear to be similar. However, by observing the plots that exist in between, similarities can be established.

Figure 2.17 presents a similar case to those given in Figure 2.7 with an end diameter of 35μm and total length of 3.5mm. The first trend of interest is the way particular natural frequencies converge, for example the blue, corresponding to f_{n1}, and cyan, corresponding to f_{n2}, lines at L_g/L=0.75, and then diverge again as L_g/L increases. This trend is also clearly observed for all other combinations of neighbouring natural frequencies, such as f_{n3} and f_{n4} at L_g/L of 1.5.

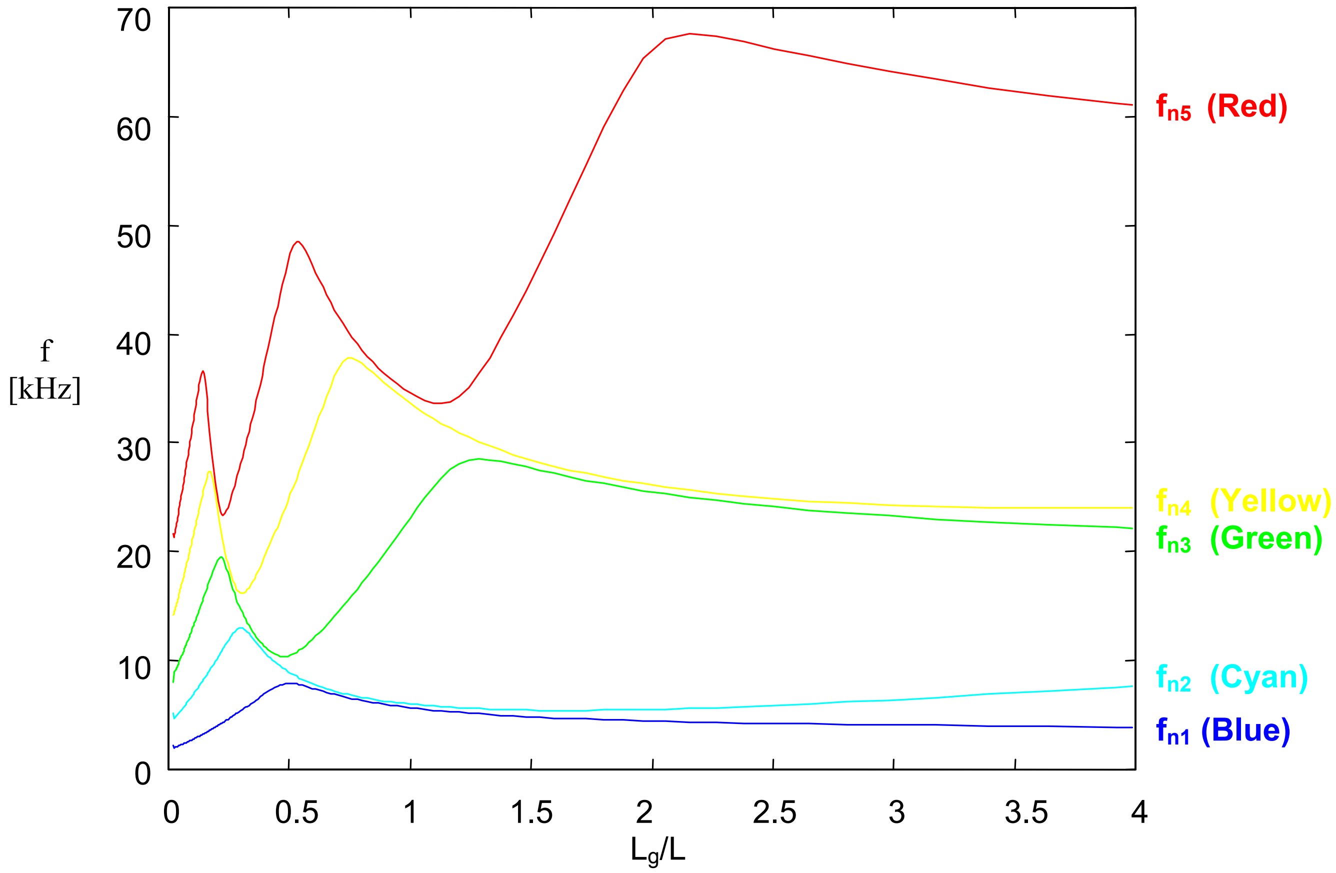

Figure 2.17. Frequency versus L_g/L plot for a wire having d_g=35μm and total length, L_o=3.5mm.

Another point of interest is the location of L_g/L=0.5, in relation to the f_{n2} (cyan) line. As the f_{n1} (blue) line approaches the f_{n2} (cyan) line around L_g/L=0.5, the f_{n3} (green) line separates. It appears that only two natural frequency lines can be in close proximity at any given time. When a third natural frequency approaches to the earlier two, from below, the higher of the earlier two seems to separate as the value of L_g/L increases. This trend is also present at other locations, such as for L_g/L=1.25 for the third, fourth and fifth natural frequencies.

The third point of interest is the apparent grouping of natural frequencies, within the frequency range of interest. The first and second natural frequencies have only one peak, whereas the third and fourth have two peaks. Following with this pattern, the fifth and sixth (not shown here) have three peaks. This trend continues for higher modes.

Each of the frequency plots shown in Figure 2.7 exhibit these discussed trends. Some of the plots, particularly those with small end diameters, appear to be stretched versions where the clarity of the trends is ‘diluted’. The existence of such clear trends has led to the search for scaling parameters. A group of non-dimensionalised parameters to scale the plots would negate the need for hundreds of trial cases to be explored. Rather, one frequency plot would ideally show the entire spectrum of possible results. The search for non-dimensionality has yielded only two partially successful mapping techniques. These are discussed in the following two sections.

2.3.1 Scaling Using Mass

The first successful scaling technique relates to the equivalent mass of each particular geometry. Two frequency plots can be generated where the geometries have identical end conditions and material properties except for density. Then, the first can be scaled into the second by the square root of the ratio of the two densities.

$$\omega_1 = \omega_2 \times \sqrt{\frac{\rho_2}{\rho_1}} \tag{2.1}$$

where ω_1 and ω_2, *and* ρ_1 *and* ρ_2, are the first natural frequencies and densities of the first and second geometry, respectively, and ρ_1 and ρ_2 are the densities of the two geometries. The origin of this relationship is from the solution of the natural frequencies of uniform cross sectioned standard Euler-Bernoulli beams [2]:

$$\omega = (\beta L)^2 \sqrt{\frac{EI}{\rho A L^4}} \tag{2.2}$$

where: ω is the natural frequency,

β is a constant relating to the boundary conditions and the particular mode of interest,

E is the Young's modulus of the beam,

I is the moment of inertia of the beam,

ρ is the density of the beam,

A is the cross sectional area, and

L is the length of the beam.

The usefulness of this scaling is that by varying the density, the absolute values of the frequencies can be changed rather than the relative distributions, provided that densities corresponding to real materials are chosen. Since both geometries here have the same E, I, A, L and β, the relationship in Equation 2.2 reduces to Equation 2.1. It follows that the other parameters in Equation2.2 can be scaled in the same manner.

$$\omega_1 = \omega_2 \sqrt{\frac{\left(\dfrac{E_1 I_1}{\rho_1 A_1 L_1^4}\right)}{\left(\dfrac{E_2 I_2}{\rho_2 A_2 L_2^4}\right)}}$$

$$\omega_1 = \omega_2 \sqrt{\frac{E_1 I_1 \rho_2 A_2 L_2^4}{E_2 I_2 \rho_1 A_1 L_1^4}} \qquad (2.3)$$

Hence, after generating one frequency plot, another can be generated for a new geometry with identical end conditions using equation 2.3. The limitation of this scaling technique is that all sections of the beam must be uniform for the parameter analysed. That is, each section of the stepped beam needs to have the same material properties. For example, a steel beam can be geometry 1, and an aluminium beam could be geometry 2. Geometry 2 cannot have aluminium end sections with, for instance, a tungsten middle section.

2.3.2 Scaling Using Individual Standard Beam Equations

Perhaps the most interesting of all trends in the frequency plots presented in Figure 2.7, is seen clearly only by modifying Figure 2.17. Rather than different colours being used for each of the natural frequency lines shown in Figure 2.17, Figure 2.18 has all the lines drawn in the same colour. Now, a pattern can be recognised in the way that the 'first peak' of each line is positioned. A line, possibly a hyperbola, can be superimposed onto the plot so that it covers the 'first negative gradient portion' of all five of the natural frequency lines. A similar line can be drawn covering the 'second negative gradient portions' of the third, fourth and fifth natural frequency lines. A third

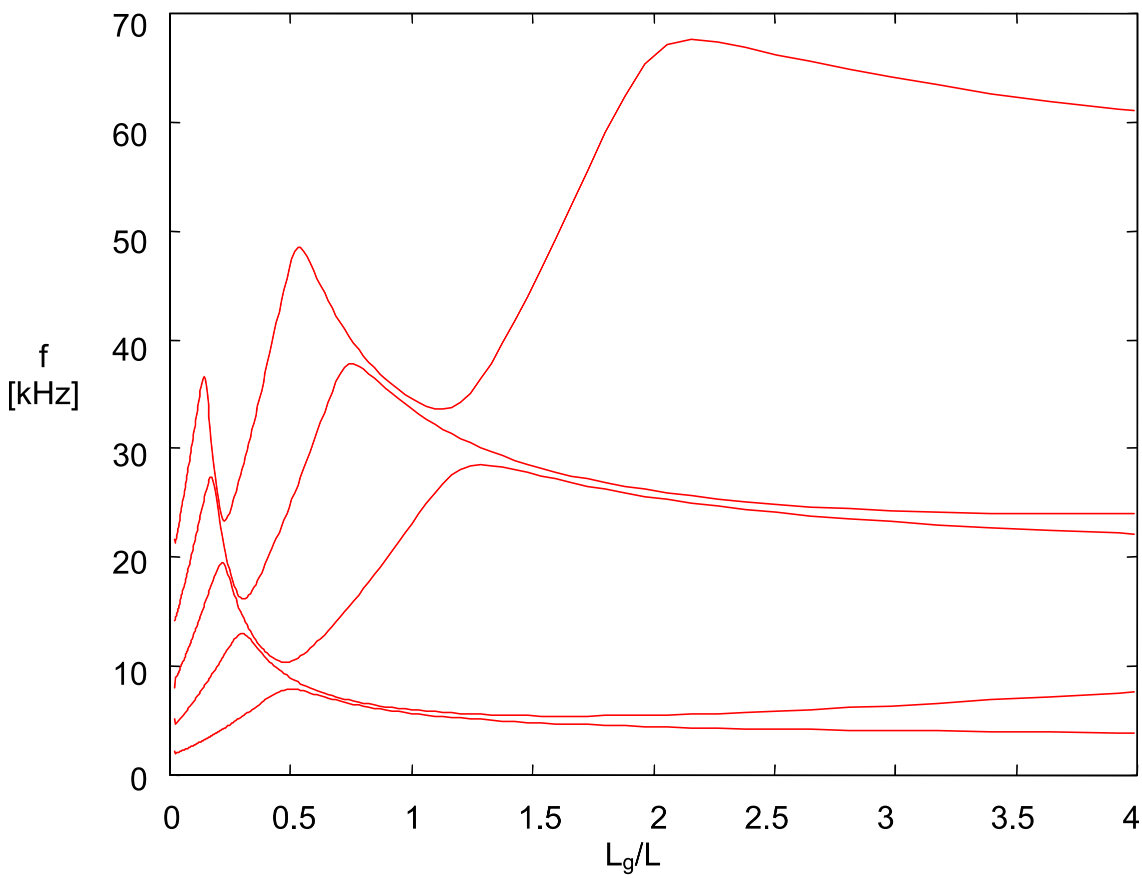

Figure 2.18. Frequency versus L_g/L plot for the same hot-wire shown in Figure 2.17 having d_g=35μm and total length, L_o=3.5mm. Plotted here using one colour for all the frequency lines.

line can represent the third negative gradient portion of the fifth natural frequency line.

More lines can be drawn, this time possibly of parabolic type, linking the ‘first positive gradient portion’ of the first natural frequency with the ‘second positive gradient’ of the third natural frequency and the ‘third positive gradient’ of the fifth natural frequency line. Similarly, the remaining positive gradient portions of each of the other frequency lines can also be linked with parabolic shaped patterns, such as the ‘first positive gradient’ of the second natural frequency with the ‘second positive gradient’ of the fourth natural frequency lines.

The hyperbolic and parabolic trends in Figure 2.17 can be mapped by using the solutions of ‘equivalent’ uniform beams. In order to follow this process, an analysis was conducted on each section of the stepped beam separately, rather than on the entire geometry as a whole. As shown in Figure 2.19, the stepped beam was divided into two uniform cantilevered beams, and one uniform fixed-fixed beam, each corresponding to the sections of the original stepped beam.

Figure 2.19. The hot-wire geometry separated into three uniform beam sections.

The natural frequencies of each of the individual sections, shown in Figure 2.19, were then calculated, from the closed form exact solutions [2], and plotted in Figure 2.20. Firstly, for the uniform cantilevered beam in Figure 2.20(a), a hyperbolic trend is observed. Moving from the left to the right on the horizontal axis, as L_g/L increases, the length of the uniform section increases such that the beam becomes more flexible, and hence, its natural frequency decreases. Conversely, in Figure 2.20(b) the plot for the uniform fixed-fixed beam exhibits parabolic frequency trends. Moving from the left to right on the graph corresponds to a decrease in the length of the section, so that it becomes more rigid, and its natural frequency increases.

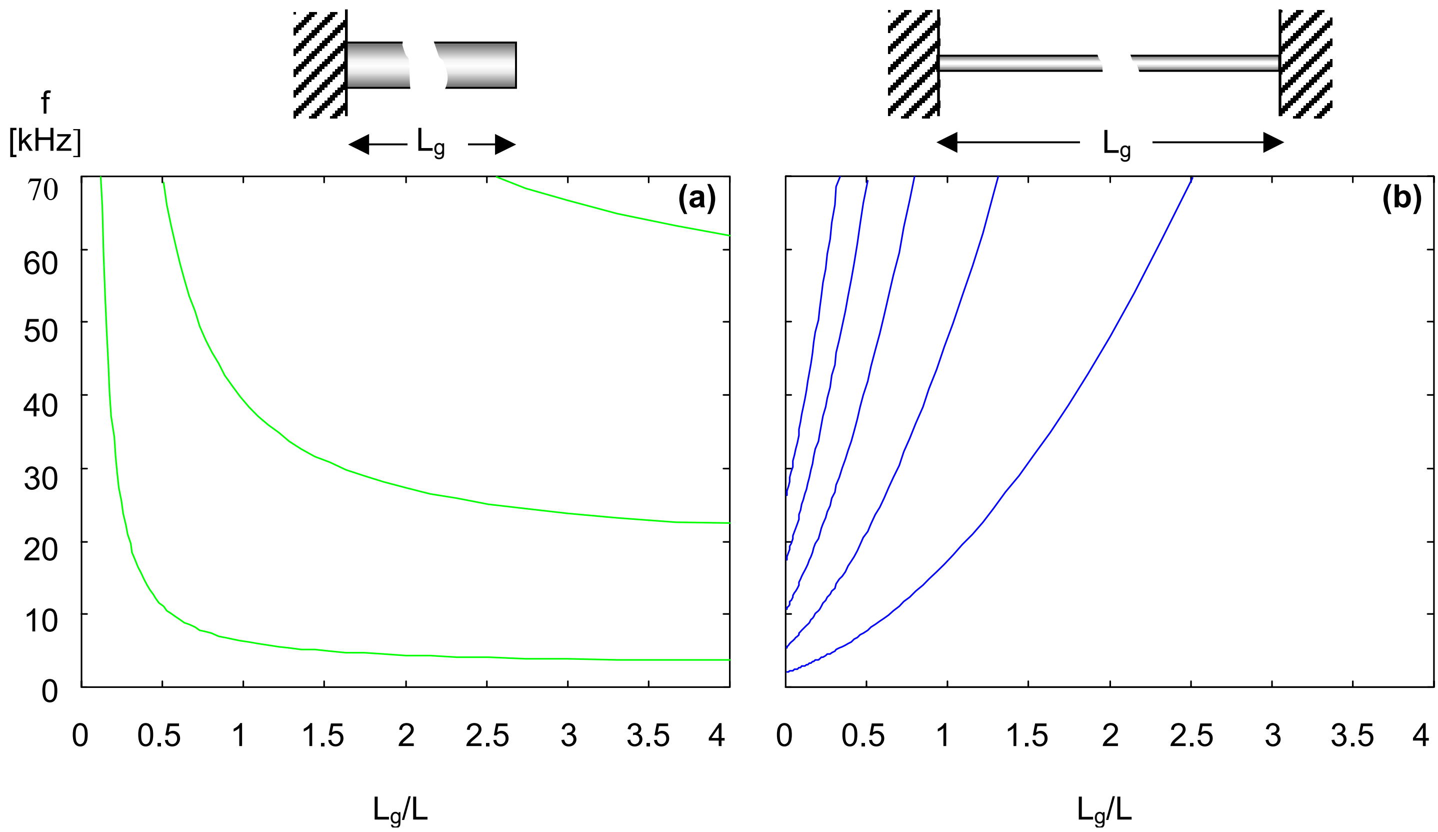

Figure 2.20. Frequency distribution plots for the individual uniform beam geometries shown, plotted on the same scale as in Figure 2.18.

Figure 2.21 shows the individual section frequencies plotted over the frequencies of the original stepped beam. The red line, corresponding to the natural frequencies of the stepped geometry, closely follows the blue and green lines of the middle and end sections, respectively. For example, the second mode (red) involves the 1st blue curve and the 1st green curve. The third mode (red) involves the 1st and 3rd blue curves and the 1st and 2nd green curves. Hence, the natural frequency plots for the stepped geometry can be mapped using two standard uniform beam equations, rather than having to go through the lengthy finite elements solutions.

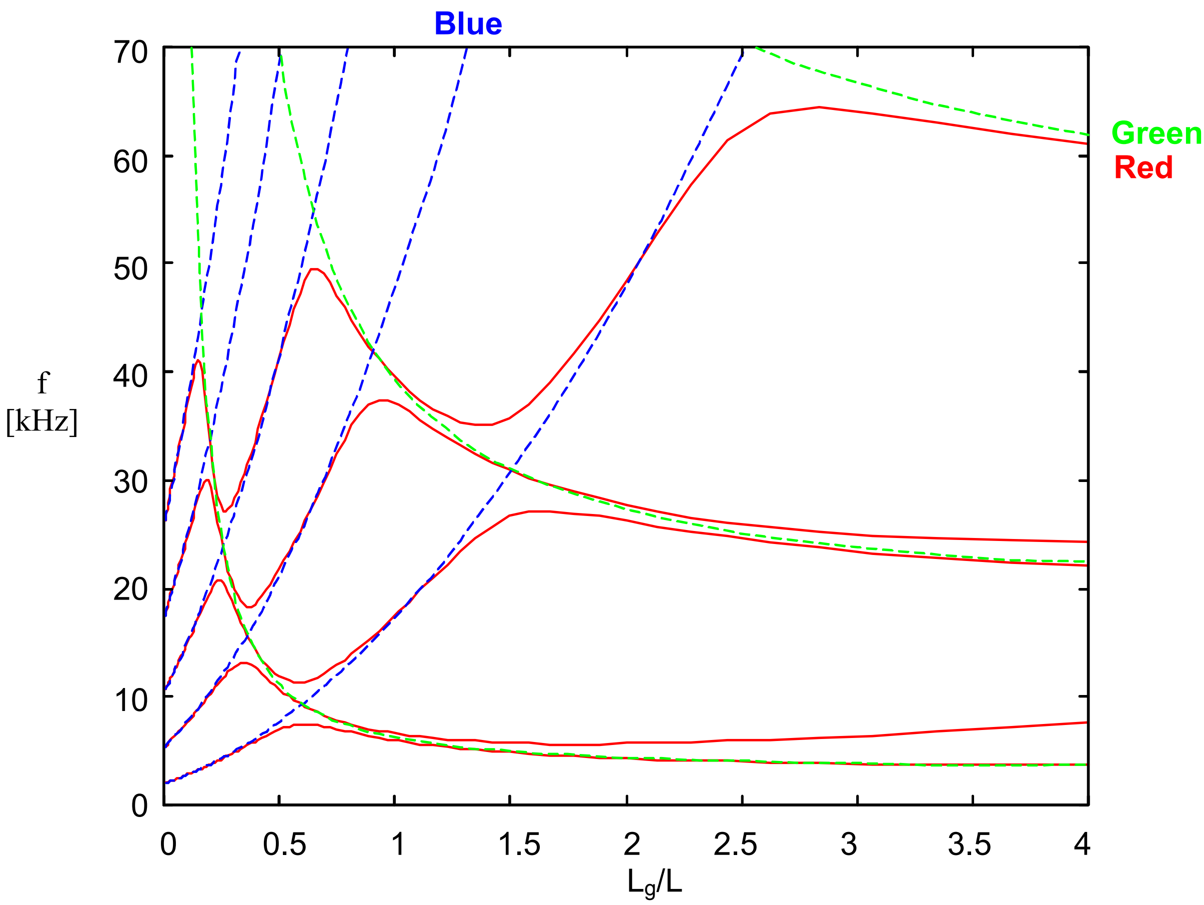

Figure 2.21. Frequency against L_g/L plot for the same hot-wire shown in Figure 2.19 shown in red. Also plotted are the blue and green lines from Figure 2.20 corresponding to the middle and end sections, respectively.

The correlation between the natural frequency separations of the stepped geometry and those of the individual sections is suspected to be only valid for significant step changes in section diameters, as seen previously in Figure 2.7. The middle section of the geometry needs to be able to vibrate largely on its own, as if it were mounted between two fixed ends.

There is a clear mismatch between the red lines and the interchange between the blue and green lines in Figure 2.21. The red line intersects with the blue line, and they have similar slopes, then it asymptotes towards the green line. The degree of mismatch is dependent on the magnitude of the step change between the thick and thin cross sections of the stepped beam. Investigations have shown that as the step change decreases, so does the correlation between the frequencies. As a guide, if the step change between the two sections is at least 5 times, then, a reasonable match is observed. If a larger step change is practicable, of around 10 times, then a closer match is expected.

The procedure outlined in this section can be used to eliminate the number of trial searches required. When a promising curve is found, the frequency distribution must be verified using a complete model.

2.4 Conclusions

In this chapter, a novel technique has been introduced for the control of transverse vibrations of slender beams. The technique relies on modifying the structure slightly to achieve close first and second natural frequencies. When the first and second natural frequencies are close, the beam attempts to have both mode shapes exist simultaneously. The resulting mode shape is a combination of the first and second mode shapes. This combined mode shape is ‘unbalanced’ as there are two mode shapes equally possible for the same frequency. This particular situation restricts the beam’s vibration from building to resonance in any one particular mode. A numerical procedure is outlined here for the general case of a fixed-fixed beam geometry. Scaling and trends of the numerical results are discussed. The next three chapters discuss application of this control technique to practical problems.

Chapter 3

SENSING WIRE VIBRATION OF HOT-WIRE PROBES

3.1 Introduction

Hot-wire anemometry is a powerful and practical technique for measuring mean and fluctuating fluid velocities and temperatures. It is relatively inexpensive and easy to use for research, teaching and industrial applications. The sensing component of a hot-wire probe is a thin wire, typically in the order of 2 to 6 micrometers in diameter and about 3 millimetres in length. In Figure 3.1 the sensing wire mounted between two prongs is shown.

For traditional isothermal applications, the sensing wire is kept at a constant temperature of about 300^{o} C during measurements, when used in the constant temperature anemometry (CTA) mode. The cooling effect of the oncoming fluid is interpreted as the velocity of the flow to be measured.

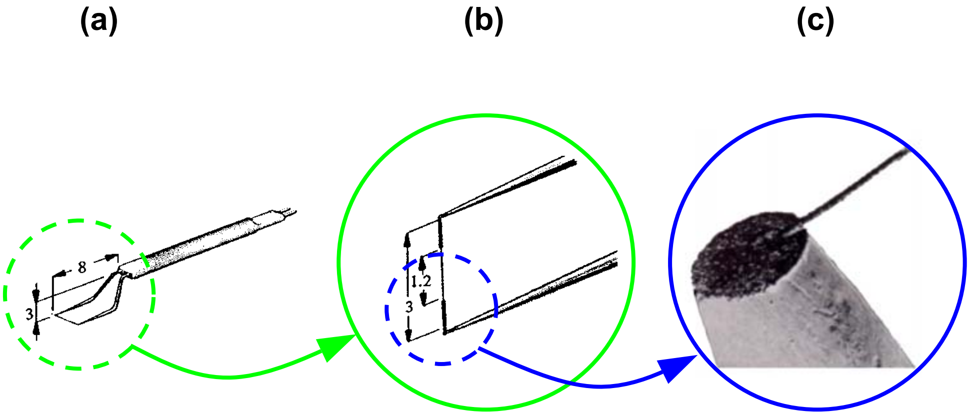

(Dimensions are shown in mm)

Figure 3.1. Showing **(a)** hot-wire probe in entirety, **(b)** hot wire alone [11] and **(c)** electron microscope photograph of wire and prong connection [12].

As shown in Figure 3.2, the hot wire probe forms one resistor in a Wheatstone bridge. Two fixed resistors (R1 and R2) and an adjustable resistor (R3) complete the Wheatstone bridge. Oncoming fluid velocity cools the sensor and causes bridge unbalance. A differential feedback amplifier senses the bridge unbalance and adds current to maintain the temperature of the sensor [13]. Since the feedback amplifier responds rapidly, the sensor temperature remains virtually constant as the velocity changes [14]. The voltage change required to maintain the constant sensor temperature is interpreted as the velocity of the oncoming fluid through a calibration procedure.

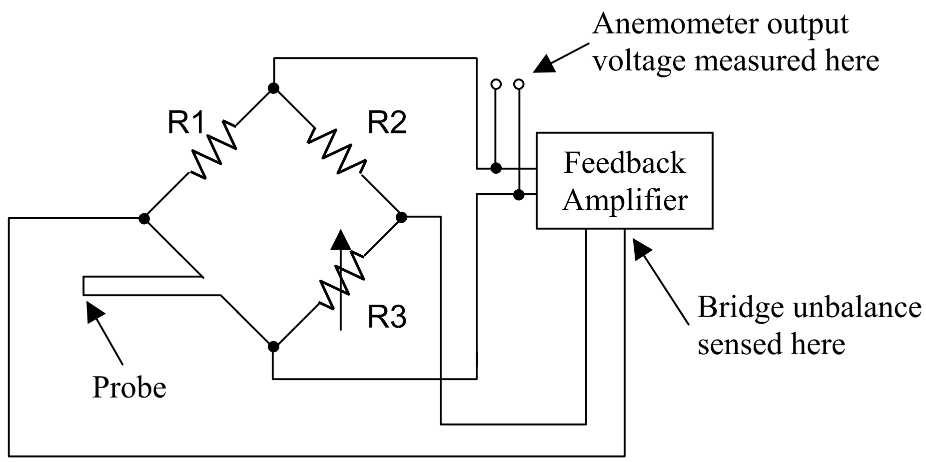

Figure 3.2. The block diagram of a constant temperature anemometer [13].

The underlying assumption of the interpretation discussed in the preceding paragraph is that the wire is stationary, and the velocity of the flow 'relative' to the wire can be assumed to be the 'absolute' velocity. However, due to its flexibility, the hot-wire probe is susceptible to large amplitude resonance vibrations. As a result of these vibrations, the relative velocity can no longer represent a close indication of the absolute flow velocity.

A turbulent flow approaching the wire has mean and fluctuating velocity components. The mean velocity can cause a deflection of the wire, which is best described as causing a constant sag or curve in the wire. Wires are manufactured with a pre-tension, which may compensate for this effect. This curve does not present a significant problem to the accuracy of the measurements, since it causes no fluctuations in the wire displacement. However, the fluctuating velocity component of the flow can cause the wire to resonate. Each velocity fluctuation in the flow has an associated fluctuating force that leads the wire displacement by a phase angle of 90 degrees at resonance [2]. On the other hand, the wire velocity always leads the displacement by 90 degrees. Hence, at resonance, the velocity of the wire is in phase with the excitation force fluctuations. Therefore, the velocity of the wire is in phase with the velocity fluctuations in the flow. This presents a significant problem, if the velocity fluctuations of the wire are comparable in magnitude to the velocity fluctuations in the flow. It is easy to see that if the wire has the same amplitude velocity fluctuations as those of the flow velocity, then there would be no relative velocity between the wire and the flow. Zero relative velocity is, of course, an unlikely condition. However, the relative velocity sensed by the probe wire can be somewhat smaller than the absolute velocity of the flow. In Figure 3.3 (a) a hot-wire probe is shown in the wake of a cylinder, where the flow is from top to bottom. A close up of the blurry envelope in Figure 3.3 (b) indicates the stream-wise vibrations possible in turbulent flow.

In this chapter, the limited works related to the vibration of a hot-wire probe are reviewed in the next section. In section 3.3, a numerical model is introduced. The numerical predictions are discussed in Section 3.4. The scaled-up experimental results and the actual size flow measurements are presented in Sections 3.5 and 3.6, respectively.

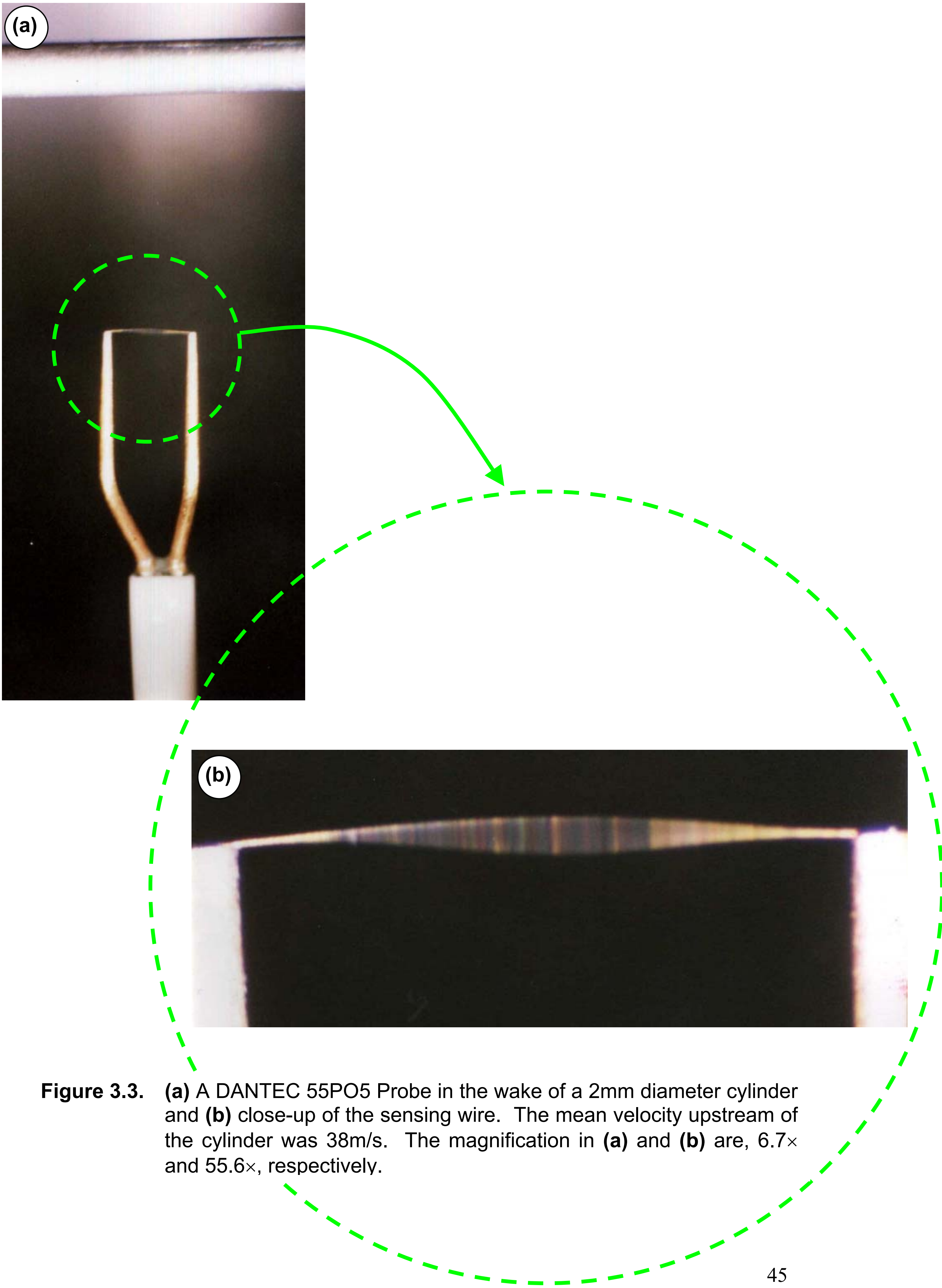

Figure 3.3. **(a)** A DANTEC 55PO5 Probe in the wake of a 2mm diameter cylinder and **(b)** close-up of the sensing wire. The mean velocity upstream of the cylinder was 38m/s. The magnification in **(a)** and **(b)** are, 6.7× and 55.6×, respectively.

3.2 Earlier Work

The problem of wire vibration was first observed by Perry et al. [15, 16]. This work investigated two types of wire vibration, namely, rotational vibration and skipping (or whirling) of the wire. However, the more predominant case of stream-wise transverse vibrations had not been investigated in detail before the work of [8].

This earlier study in reference 8 indicated measurement errors when large amplitude wire vibrations are expected. It suggested that the filament of a hot-wire probe can be excited at its first or higher resonance modes. If the probe wire is excited in the first mode, the resulting vibration velocity is in-phase with the velocity fluctuations in the flow along the entire wire length as mentioned earlier. Hence, these in-phase oscillations may reduce the relative velocity between the wire and the flow, leading to smaller readings than the true absolute velocity of the flow. Therefore, hot wire dimensions must be chosen such that the resulting first natural frequency of the wire is larger than the expected frequency content in the flow.

One way to achieve a high first natural frequency of the wire is to use a short wire. However, a short wire causes heat conduction loss to the prongs. Heat conduction creates a non-uniform temperature distribution along the wire, which reduces hot wire sensitivity. This prominent problem is discussed in [17] and [18]. Hence, this condition may not be practically achievable.

The earlier work in [8] investigated the differences in the experimental results obtained with different probes under the same flow conditions. It showed that large measurement errors were present for some probes, while others had more accurate results. For cases when the first natural frequency is within the frequency range of excitation, the most accurate measurements were observed when the first and second natural frequencies of the probe wire were close numerically. This earlier investigation pointed out a limited number of already existing favourable designs. However, no effort was made to look at new designs with improved dynamic characteristics. It is this determination, which forms the basis for this research thesis. The objective here has been to explore the possibilities of linking the first and second natural frequencies together to achieve favourable vibration characteristics.

3.3 Numerical Modelling

Application of the technique discussed in Chapter 2 to a hot-wire probe, was commenced by numerically modelling the particular slender beam of interest. The geometry of a hot-wire probe sensing wire can be modelled using beam type (a) from Figure 2.5, which is shown again here in Figure 3.4 for convenience. In this figure, the middle sensing wire has d and L for diameter and length, whereas d_g, L_g and L_o represent the diameter and the length of the thicker ends and the total length of the wire, respectively. Boundary conditions are taken to be built-in where the wire is welded to the prongs. The electron microscope photograph presented in Figure 3.1 (c), justifies this boundary condition by clearly showing the welded connections.

Hot-wire probes are manufactured with an intentional pre-tension at room temperature. The numerical model does not include this pre-tension. The presence of any wire pre-tension would simply increase all the natural frequencies by the same scale, rather than making any relative changes. In

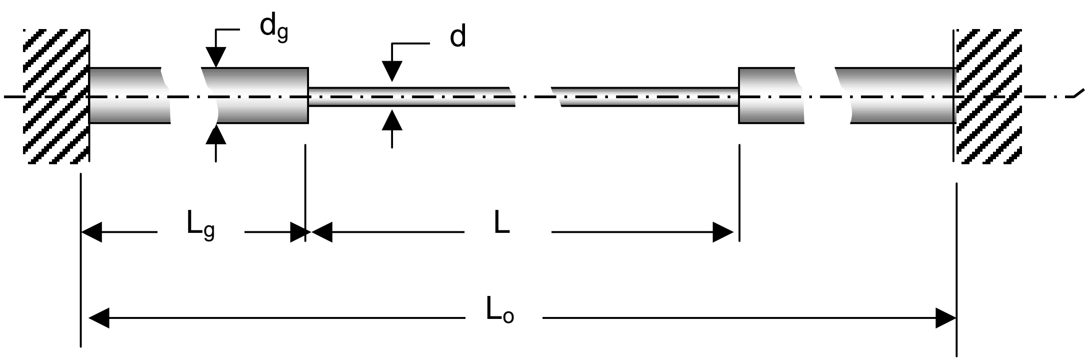

Figure 3.4. Schematic of the sensing wire numerical model.

addition, pre-tension may be lost when the wire is heated for flow measurements.

3.3.1 Numerical Model

Along the length of the wire, 30 standard finite beam elements [2] were used to approximate the dynamic properties of the model in Figure 3.4. The three sections of the beam had ten elements each, a sufficient number to give an accurate representation of the first five mode shapes. The minimum number required was found to be 6 elements, so 30 is ample. Solution of the resulting eigenvalue problem in Matlab® [10] provided the first 58 natural frequencies for the wire, of which the first five were of interest, since the higher modes are well outside the frequency range of flow excitation.

Dynamic response of the wire to a broadband, random white noise excitation force was obtained by numerically integrating the system differential equations of motion using the Newmark-β technique [2]. The white noise was generated in Matlab® [10] using the built in random number generator, then scaling the output to the desired frequency by altering the time step. The frequency content of the excitation force (zero to 50 kHz) was sufficient to excite up to the fifth mode of the wire. Broadband excitation may be assumed to be indicative of the forces that a wire experiences when placed in a turbulent flow. This external force was applied at one node to the right of the mid-point so as to be able to excite the even numbered modes, which have nodes at the mid-point. A single node input was chosen rather than a uniformly distributed load for closer similarity with the experimental set up discussed later. Structural damping of 1% was used in the model. 50,000 steps of integrations were performed with a time step of 10 μs to allow the root mean square (rms) of the displacement to settle to within 1% of its steady state value.

One of the existing hot-wire probe geometries, Probe 3 in [8], is investigated here as the starting geometry. This probe has a total length of 3 mm, a sensitive length and diameter of 1.18 mm and 5.75 μm, respectively, resulting in a sensitive length to diameter ratio, L/d, of 205. It has a thick end diameter of 30 μm. The probe wire has a platinum core plated with tungsten, and its thicker ends are plated with gold. Previous research showed that Probe 3 was the least susceptible to large amplitude vibrations, and one of the most accurate for measurements in turbulent flow [19]. The objective here has been to possibly improve it further.

3.3.2 Numerical Predictions

The effect of varying the ratio of the length of the end sections to the sensitive length, L_g/L, is shown in Figure 3.5. From left to right along the horizontal axis, the ratio of the end length to the sensitive length, L_g/L, increases. This increase results in a smaller L and larger L_g for a constant L_o of 3 mm. The ratio of the end length to the total length, $L_g/L_{o,}$ is also shown as a second horizontal axis for reference. The vertical axis represents the five resonance frequencies of the wire corresponding to the five curves given in ascending order. Figures 3.5(a), 3.5(b) and 3.5(c) correspond to end diameters, d_g, of 15μm, 30μm and 45μm, respectively.

The starting geometry of Probe 3 is marked with a vertical dashed line at L_g/L of 0.77 in Figure 3.5(b). As L_g/L increases from the starting value of 0.77 in this figure, the first (f_{n1}) and second (f_{n2}) resonance frequencies move closer, while the third resonance frequency is pushed away. Furthermore, the third and fourth resonance frequencies also approach one another as L_g/L increases. As the thick ends increase in length, they become more flexible and participate more actively in vibrations. It appears that thick ends can participate a lot more readily in the first two modes as compared to the higher ones. As a result, increasing L_g/L generally gives smaller f_{n1} and f_{n2}; while higher modes can exhibit initial rapid increases before levelling off and then decreasing gradually. This trend is most clearly observed in Figure 3.5(c), where d_g is 45 μm, whereas Figure 3.5(a) shows only slight changes in the relative positioning of natural frequencies.

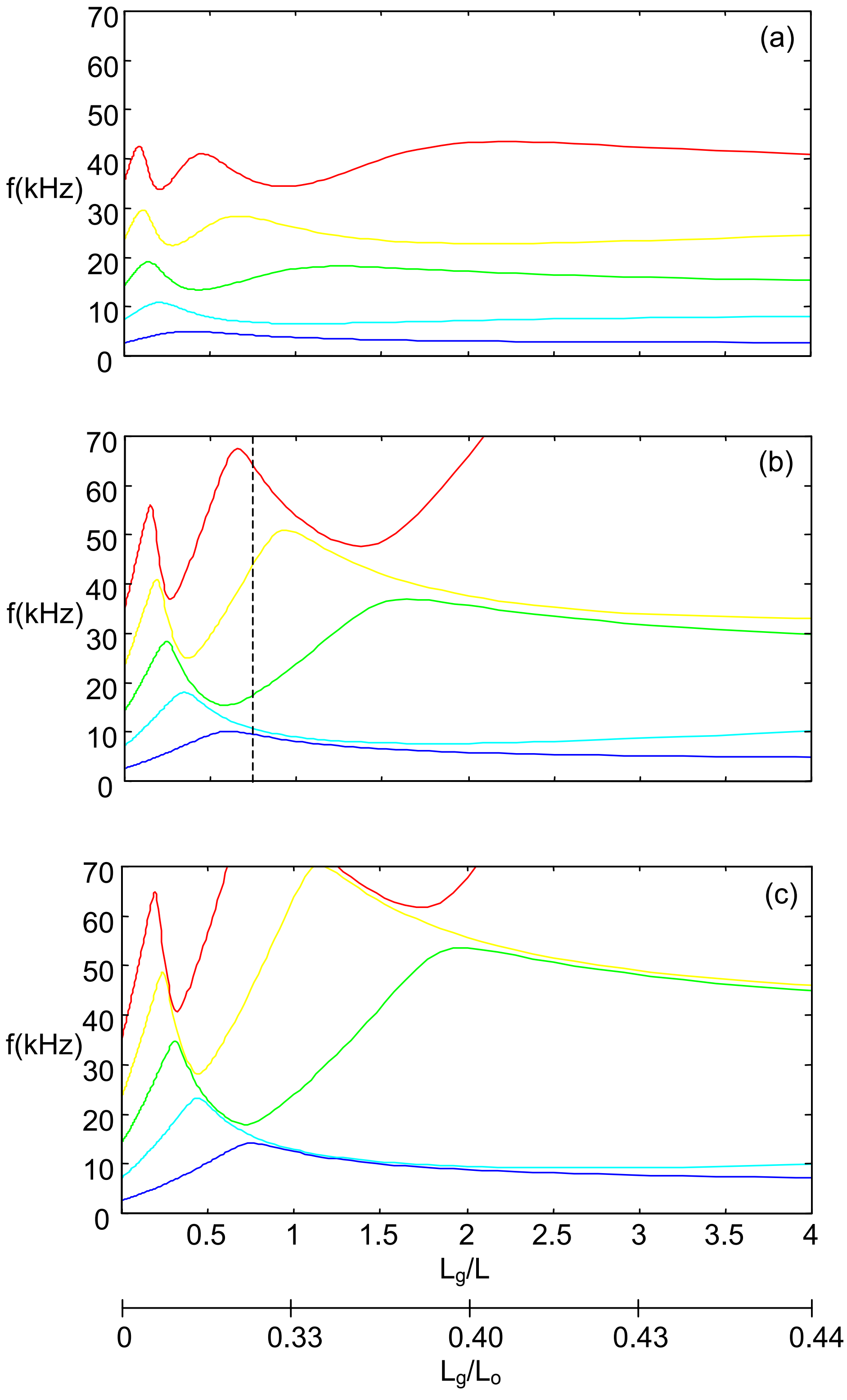

Figure 3.5. Variation of the first five natural frequencies with L_g/L for d_g of **(a)** 15 μm, **(b)** 30 μm and **(c)** 45 μm. L_g/L_o scale also shown.

The effect of L_g/L decreasing from the starting value of 0.77 in Figure 3.5 (b), is the relative separation of the resonance frequencies. For L_g/L of approximately 0.2, all five resonance frequencies become almost equally spaced. The reason for this trend originates from the effective stiffening of the ends as they become shorter. Short ends contribute less to the dynamic response. The response of the sensing wire overwhelms that of the thick ends, eventually approaching the case of a uniform beam consisting of the sensing section alone with well-separated natural frequencies.

Eight representative end length to sensitive length ratios (of 0.5, 0.77, 1, 1.13, 1.5, 2, 2.5 and 3) were chosen from Figure 3.5, and the resulting probe wire models were subjected numerically to a broad band excitation to obtain their dynamic responses for comparison. The results of this excitation are shown in Figure 3.6. In Figure 3.6, a value of zero on the horizontal axis represents the middle of the wire. The vertical axis is the normalised rms of the displacement amplitude. The vertical axis is normalised by dividing the rms response of each case by a scaler parameter, which is the rms response of Probe 3 in the mid span. Probe 3 from reference [8] was previously shown to be the best existing design. Probe 3 is marked with (o) in Figure 3.6 (b), having L_g/L of 0.77, with a total length of 3 mm and an end diameter, d_g of 30 μm. Hence, any new probe with a normalised rms response smaller than unity represents a desirable structural improvement. Any normalised response larger than unity, however, indicates a detrimental effect due to geometric changes. Clearly, reduction in the end diameter to 15 μm, has a detrimental effect as shown by the increased rms amplitudes in Figure 3.6(a).

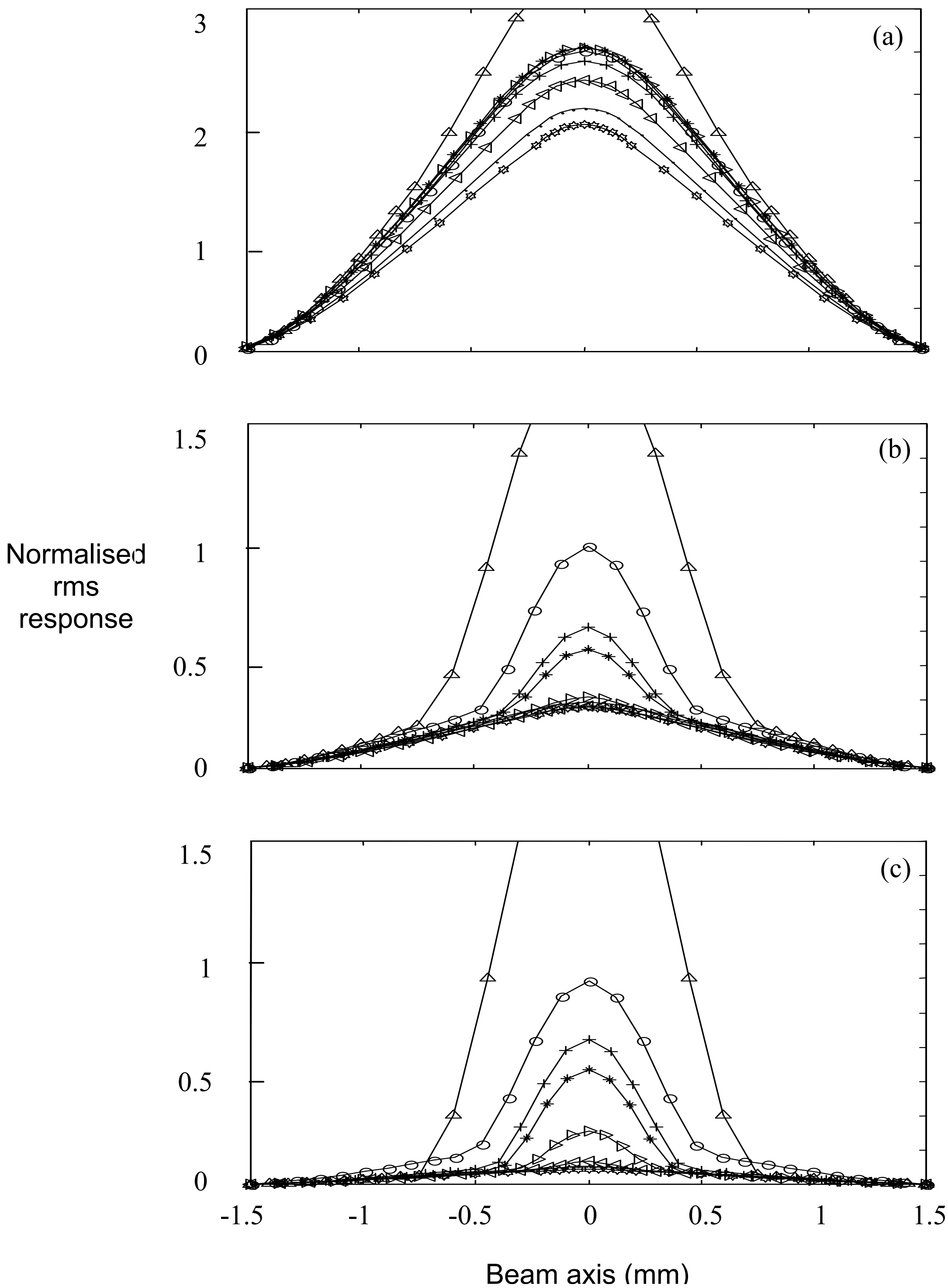

Figure 3.6. Variation of the normalised rms displacement response for random white noise excitation and for d_g of (a) 15 μm, (b) 30 μm and (c) 45 μm. L_g/L: 0.5(△); 0.77(o); 1(+); 1.13(*); 1.5(▷); 2(◁); 2.5(•); 3(✡).

Figure 3.6(b) shows the reduction in amplitude achievable by altering L_g/L. The best, lowest amplitude, case is for L_g/L of 3 (✡). It is notable, however, that there is little difference in amplitude between geometries having L_g/L of between 1.5 (▷) and 3 (✡). Figure 3.6(c) shows the rms amplitudes for probes with an increased end diameter d_g of 45 μm. Here, a probe with L_g/L of 1.5 (▷) has comparable amplitude to that having L_g/L of 1.5 (▷) with d_g of 30 μm. However, unlike the case for 30 μm, increasing L_g/L to 3 (✡), reduces the RMS amplitude significantly for 45 μm.

A more concise presentation of this data may be achieved by plotting only the mid-span rms amplitude for each geometry, as shown in Figure 3.7. Similar

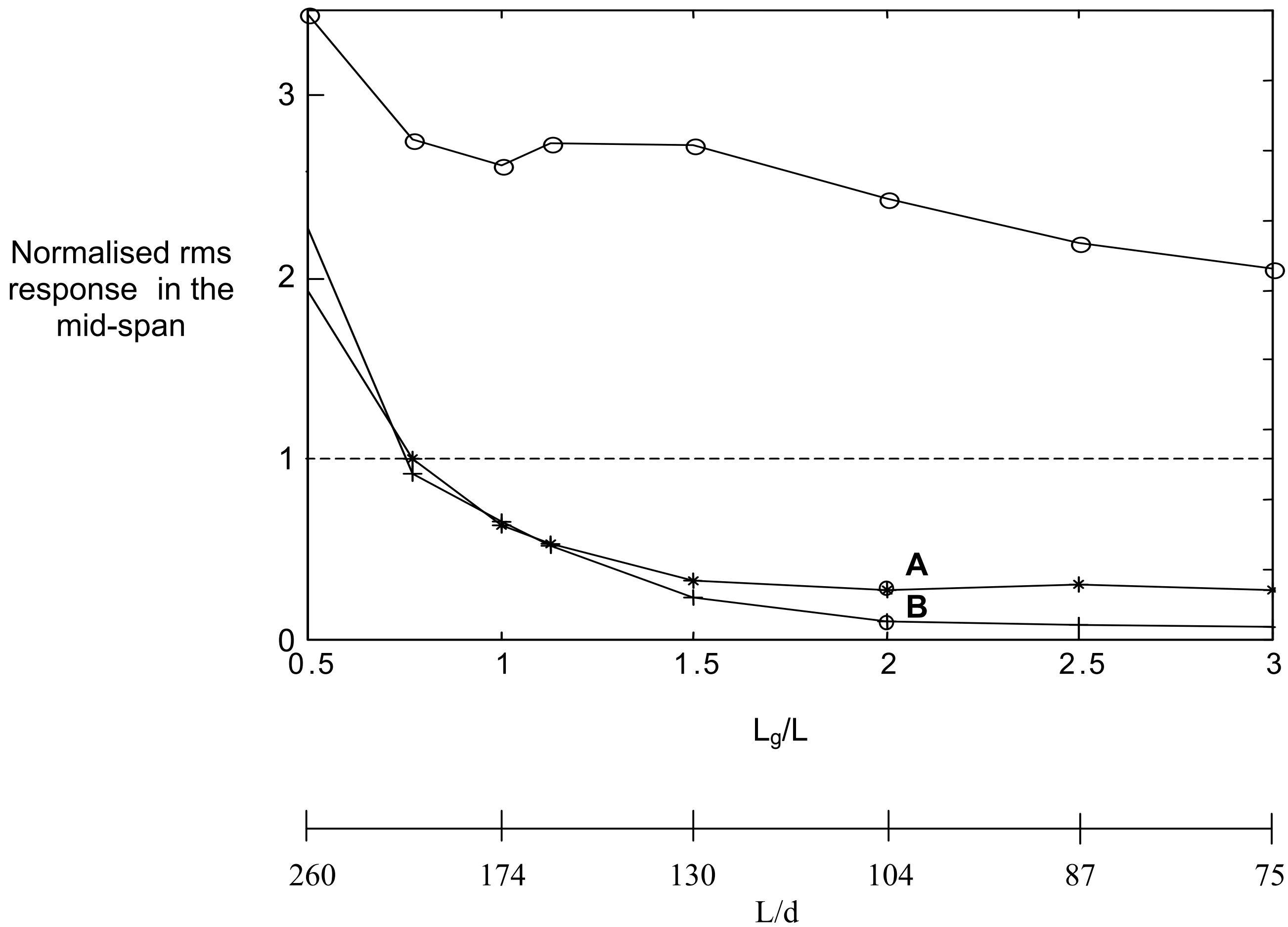

Figure 3.7. Variation of the peak rms displacement at the mid-span with L_g/L (or L/d) for d_g of 15μm (o), 30μm (*) and 45μm (+). A and B correspond to the probes examined further.

to Figure 3.6, the rms responses are normalised by dividing them by the response of the starting geometry. The horizontal dotted line represents the rms response of Probe 3, which intersects the 30 μm line at L_g/L of 0.77. Figure 3.7 shows a clear reduction of the rms amplitude as L_g/L increases. Of particular interest is the plateau seen in the curves corresponding to end diameters, d_g, of 30 μm and 45 μm. In this figure, a second horizontal axis is also shown in terms of the sensing length to diameter ratio, L/d. The effect of L/d in the selection of probe geometries is discussed in the next section, Section 3.3.3. Here, the argument is limited to determining the probe geometry, which is the least prone to transverse oscillations.

The displacement history of Probe 3 is shown in Figure 3.8, along with those of two better cases having L_g/L of 2, and d_g of 30 μm (Probe A) and 45 μm (Probe B) chosen from Figure 3.7. The mid-span rms displacement of these two probes are marked in Figure 3.7. Here, the vertical axes are normalised by scaling the peak response of Probe 3 in Figure 3.8 (a) as unity. The displacement histories show the reduction in response for the suggested geometric changes. The smallest rms amplitude, approximately 0.1 in Figure 3.7, is achieved using a total length of 3 mm, L_g/L of 2 and end diameter, d_g of 45μm, referred to as Probe B above. This combination represents a 90% reduction when compared to the original rms amplitude.

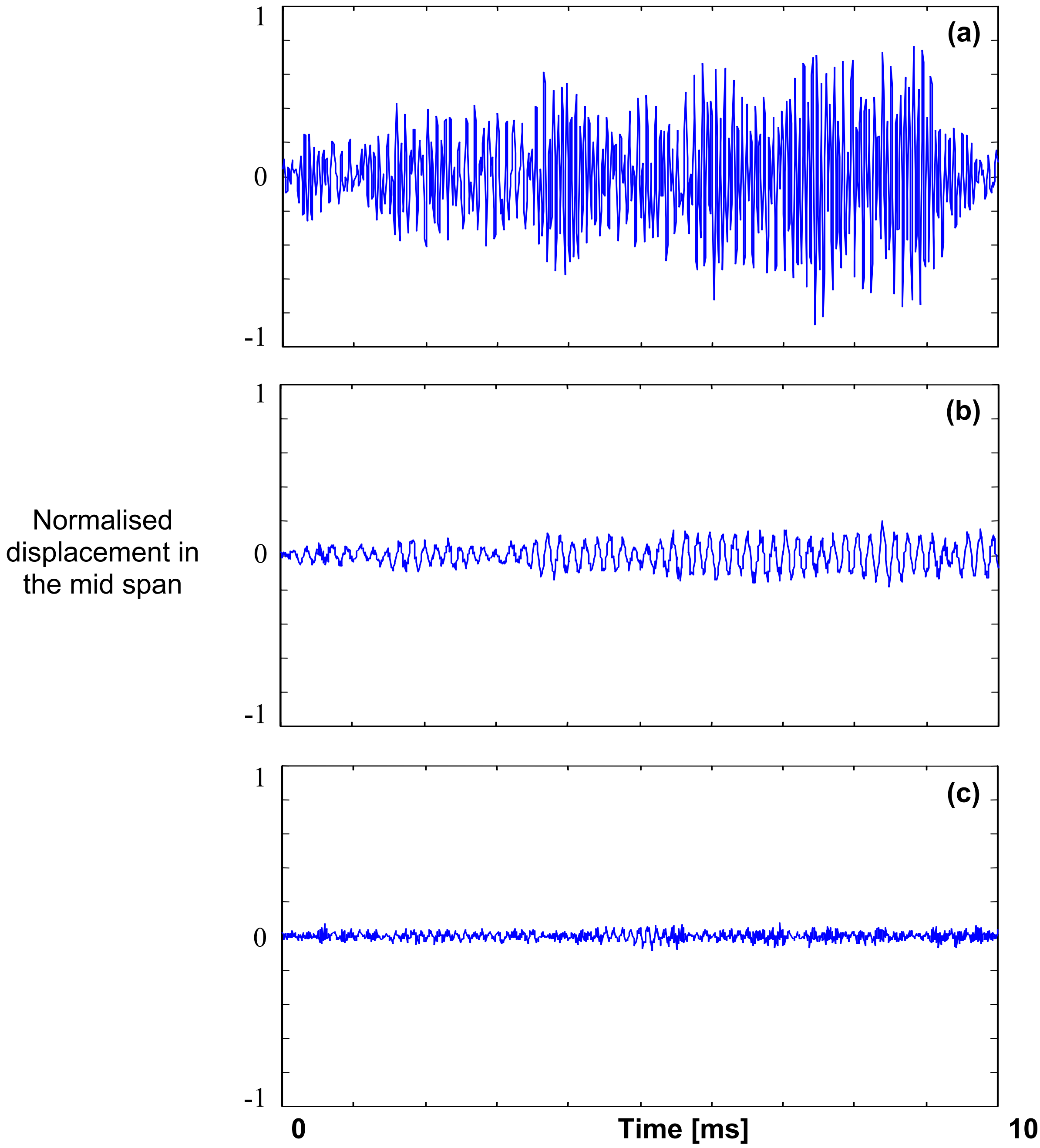

Figure 3.8. Displacement histories for **(a)** Probe 3, **(b)** Probe A having $L_g/L=2$ and $d_g=30\mu m$, and **(c)** Probe B having $L_g/L=2$ and $d_g=45\mu m$. The sensitive length to diameter ratios for **(a)**, **(b)** and **(c)** are 205, 104 and 104 respectively.

3.3.3 Effect of L/d

The suggested geometric changes are shown graphically for clarity in Figure 3.9, providing a visual comparison amongst Probes 3, A and B.

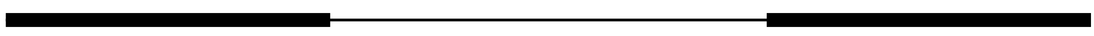

(a) Probe 3 with a total length of 3 mm and a sensitive length of 1.2 mm, giving L_g/L of 0.77. The wire has an end diameter of 30 μm, and a sensitive length to diameter ratio, L/d, of 205.

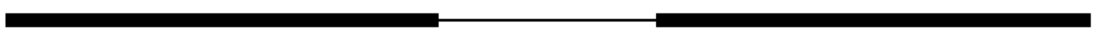

(b) Probe A, with a decreased sensitive length of 0.6 mm, giving L_g/L of 2 and L/d of 104.

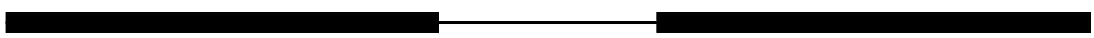

(c) Probe B, with a decreased sensitive length of 0.6 mm, once again giving L_g/L of 2, and L/d of 104. This wire has an increased end diameter of 45 μm.

Figure 3.9. Wire geometries for **(a)** the original probe, **(b)** for Probe A, and **(c)** for Probe B.

The previous work [19] had shown that a range of sensitive length to diameter ratios between 310 and 160 was acceptable. The favourable cases discussed in relation to Figures 3.8 and 3.9 have their L/d to be 104, clearly smaller than the recommended minimum value. If a minimum L/d of 160 is to be kept, then a sacrifice from the predicted reductions may be necessary.

The length to diameter ratio may be increased by decreasing the sensitive diameter, d. Such a modification leads to a more flexible sensitive section, which vibrates with larger amplitude. Compensation for this detrimental effect can be achieved by moving to L_g/L larger than 2. An example is considered here with L_g/L of 3, a total length, L_o, of 3 mm, and end diameter, d_g, of 45 μm (Probe C). Here, the sensitive diameter has been decreased to 3.75 μm, from the original value of 5.75 μm resulting in a L/d of 160. The normalised displacement history for this probe is given in Figure 3.10 in the same format as in Figure 3.8. The reduction in rms amplitude from the Probe 3 amplitude is 85%. Compared to the 90% reduction achieved by ignoring the L/d limit with Probe B, this geometry maintains much of the suggested benefits.

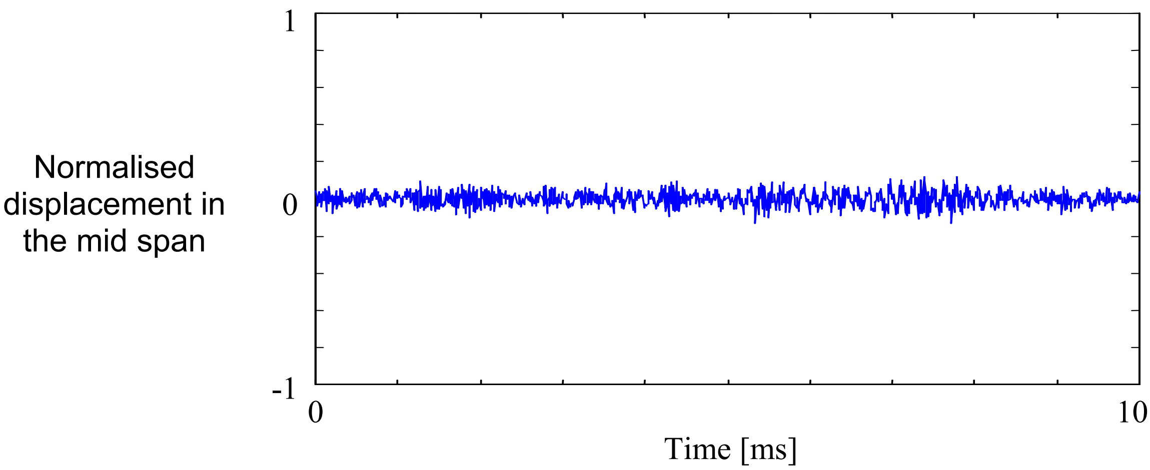

Figure 3.10. Displacement history for Probe C with d =3.75 μm such that L/d=160, plotted on the same axes as Figure 3.9.

The first three natural frequencies for the wire geometries discussed above are shown in Table 3.1. Probe 3 has a separation of 1060 Hz between its first and second natural frequencies, and 7520 Hz between its second and third natural frequencies, relative differences of 10% and 40%, respectively. The last probe geometry given in the table, Probe C with L/d of 160, has a first and second natural frequency separation of only 302 Hz, which is a relative difference of just under 4%. It is important to stress that these results are numerical predictions. The next section presents experimental observations in an attempt to verify these predictions.

Table 3.1 First three natural frequencies of Probe 3 and the new geometries.

	Natural frequencies [Hz]		
	1	2	3
Probe 3 L_g/L=0.77 d_g=30μm d=5.75μm L/d=205	9380	10440	17960
Probe A L_g/L=2 d_g=30μm d=5.75μm L/d=104	5850	7692	35633
Probe B L_g/L=2 d_g =45μm d=5.75μm L/d=104	8825	9500	53600
Probe C L_g/L=3 d_g =45μm d=3.75μm L/d=160	7736	8038	48349

3.4 Scaled-up Experimental Verification

The geometry of a hot-wire probe is not a standard one to enable comparisons with published results. Hence, verification of the numerical predictions must be done experimentally. It was decided that a scaled-up experimental model should form a preliminary verification base, before attempting actual size probe manufacturing and testing. Hence, the numerical model discussed in Section 3.3, was scaled up by 1000 times, making it 3 m long instead of 3 mm. Furthermore, steel and aluminium replaced tungsten and gold to lower the cost. Therefore, the experimental model was not an exact replica but a close representation of the earlier numerical one. This fact necessitated new numerical predictions with revised material properties and geometry for comparison with experimental observations.

3.4.1 Experimental Setup

Four beam geometries were chosen here. Beam 3 is the starting beam geometry, constructed with aluminium ends of 30 mm diameter, with a steel sensitive diameter of 6 mm. It has a total length L_o, of 3 m, and a sensitive length L, of 1.18 m giving it an L_g/L of 0.77. It is a 1000 times scaled up version of Probe 3. The beam is mounted between two workbench vices bolted into a reinforced concrete floor. These rigid end supports provide a reasonable simulation of the built-in boundary condition. The next beam geometry analysed, Beam A, has an end diameter, d_g, of 30 mm, and an L_g/L of 2. The other two beam geometries, Beam B and Beam C, have end diameters of 45 mm with L_g/L of 0.77 and 2, respectively.

The experimental set-up is shown schematically in Figure 3.11. The signal generator, item 1, produces a broadband, random signal with a frequency range of up to 50 Hz, sufficient to excite the first three natural frequencies of the beam. This type of excitation is similar to that used in the simulations. The signal is then amplified in item 2, and sent to the shaker, item 3.

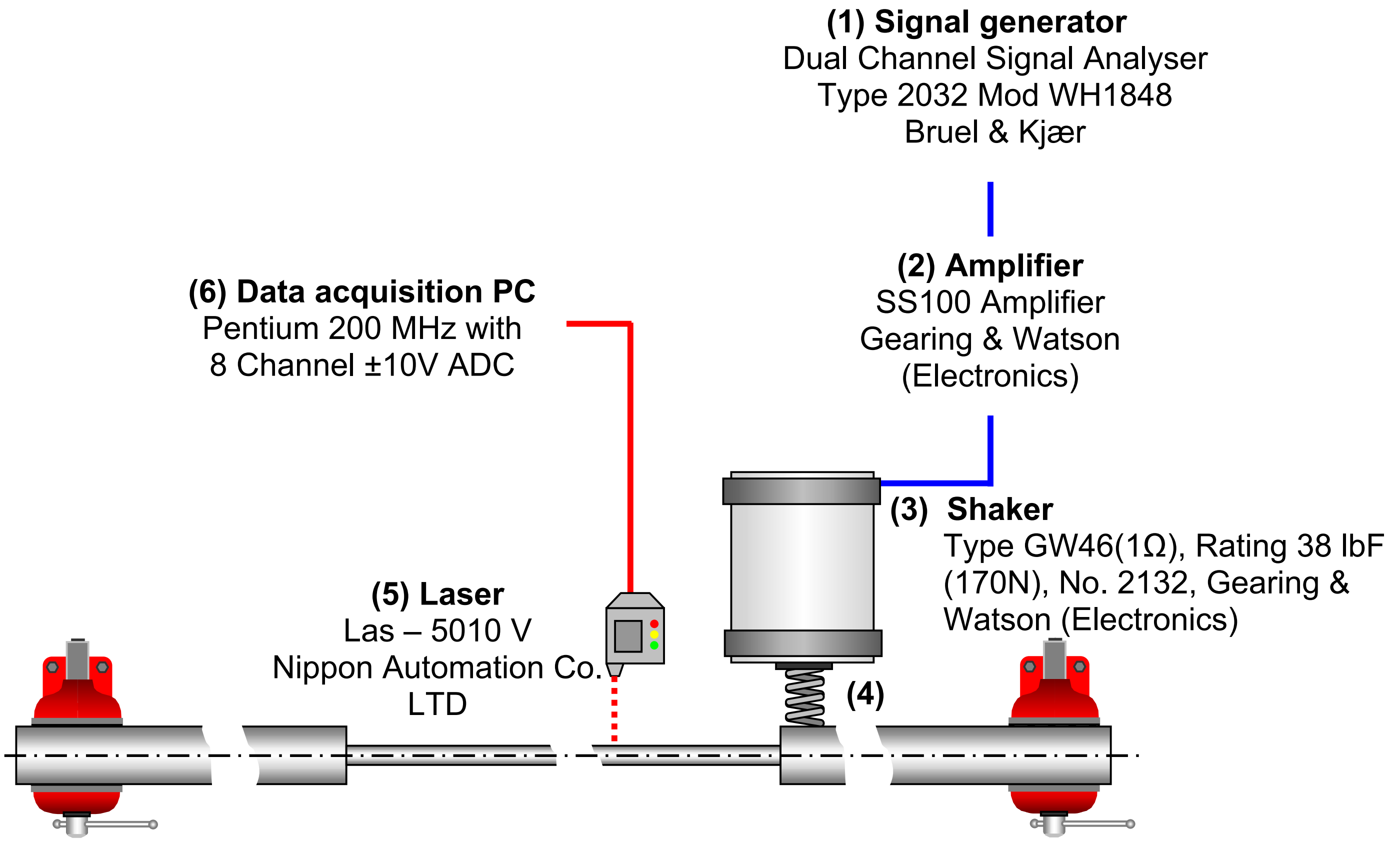

Figure 3.11. Schematic representation of the experimental rig showing
(1) the signal generator,
(2) the signal amplifier,
(3) the shaker,
(4) soft spring,
(5) the laser displacement transducer and
(6) the data acquisition PC.

The shaker was consistently mounted 800 mm from the right hand side rigid end support, so that it was well away from any nodal positions for the mode shapes under consideration. A soft spring, item 4, was used to transfer the force from the shaker to the beam. The response of the beam was measured using a laser displacement transducer, item 5. The measurement point was 1350 mm from the right hand side rigid end support. As previously mentioned, the midpoint of the beam was not chosen to avoid the node at the centre point for even modes of vibration.

The displacement data was recorded on a personal computer, item 6, with an analogue to digital converter (ATD) using HP VEE [20] data acquisition software. The data was sampled at a frequency of 1,000 Hz for just over 32 seconds. The maximum frequency of interest was observed to be around 50 Hz, as summarized in Table 3.2. 100 Hz cut-off frequency was also tested, with no change in the observed response. The data records were analysed using Matlab® [10].

Table 3.2 Experimentally and numerically determined natural frequencies of the experimental beams. f_i refers to the i^{th} natural frequency in Hz.

	f_1	f_2/f_1	f_2	f_3/f_2	f_3	Normalised rms displacement
Beam 3						
Experimental	13.5±0.5	1.44	19.5±0.5	1.13	22±1	1.0
(Numerical)	(16.5)	(1.45)	(24)	(1.2)	(29)	(1)
Beam A						
Experimental	12.5±0.5	1.36	17.0±0.5	3.12	53±2	0.63
(Numerical)	(13.5)	(1.30)	(17.5)	(3.97)	(69.5)	(0.25)
Beam B						
Experimental	16.0±0.5	1.50	24.0±1	1.25	30±1	0.58
(Numerical)	(19)	(1.92)	(36.5)	(1.05)	(38.5)	(0.85)
Beam C						
Experimental	21±1	1.08	22.0±1	2.14	47±2	0.27
(Numerical)	(21.5)	(1.05)	(23)	(3.34)	(76.8)	(0.18)

3.4.2 Scaled-Up Experimental Results

The predicted and measured natural frequencies of the four beams are shown in Table 3.2. The odd numbered columns show the natural frequencies, while the even numbered columns, with the exception of the very last column, show the ratio, $f_{(i+1)} / f_i$ where i is the mode number. Each row has the experimental results and experimental uncertainty based on 3 repetitions for different beam geometries, followed by the numerically predicted results in parentheses. Some reduction in the magnitude of the natural frequencies is observed experimentally, as compared to those predicted numerically, for all beam geometries analysed. The reason for this apparent reduction in the overall stiffness may be due to not having perfectly rigid end supports experimentally, as is the case numerically.

According to the numerical results, Beams 3 and B are expected to have relatively well separated first and second natural frequencies, f_2/f_1 of 1.45 and 1.92, respectively, making them susceptible to large amplitude vibrations. The experimentally measured separation between the natural frequencies for Beam 3, f_2/f_1 of 1.44, matches the prediction closely. For Beam B, a separation of 1.50 is observed experimentally, not in agreement with the numerically predicted value of 1.92. On the other hand, numerical predictions suggest that Beams A and C have close first and second natural frequencies, f_2/f_1 of 1.30 and 1.04, respectively, making them less susceptible than Beams 3 and B. Experimental observations verify these predictions closely, and Beams A and C have f_2/f_1 of 1.36 and 1.08, respectively.

The Fast Fourier Transform (FFT) of the displacement histories of the forced vibration responses of Beams 3, A, B and C are presented in Figures 3.12, 3.13, 3.14 and 3.15, respectively. In frame (a) of each figure, the natural frequencies corresponding to the normal modes are labelled, along with the observed skipping modes. Skipping modes were observed to exist in three dimensions, in a circular orbit around the beam's neutral axis. They were first noticed after obtaining a large number of spectral peaks in the response of the beams under random excitation. When tested under sinusoidal excitation, true normal modes were identified with their characteristic shape. The remainder of the spectral peaks gave the fundamental mode existing simultaneously in both the horizontal and vertical planes (skipping modes). Although the skipping modes appeared at several distinct frequencies, they retained the shape of the in-phase fundamental mode without any nodes.

These three dimensional skipping modes were thought to exist due to asymmetric boundary conditions where the vertical plane is slightly less rigid than the horizontal one. As a result, any misalignment of the forcing from the horizontal plane was able to excite skipping modes. Skipping modes cannot exist numerically. The difference in the numerically and experimentally observed displacement response is, therefore, attributed largely to the presence of the skipping modes in the experiments.

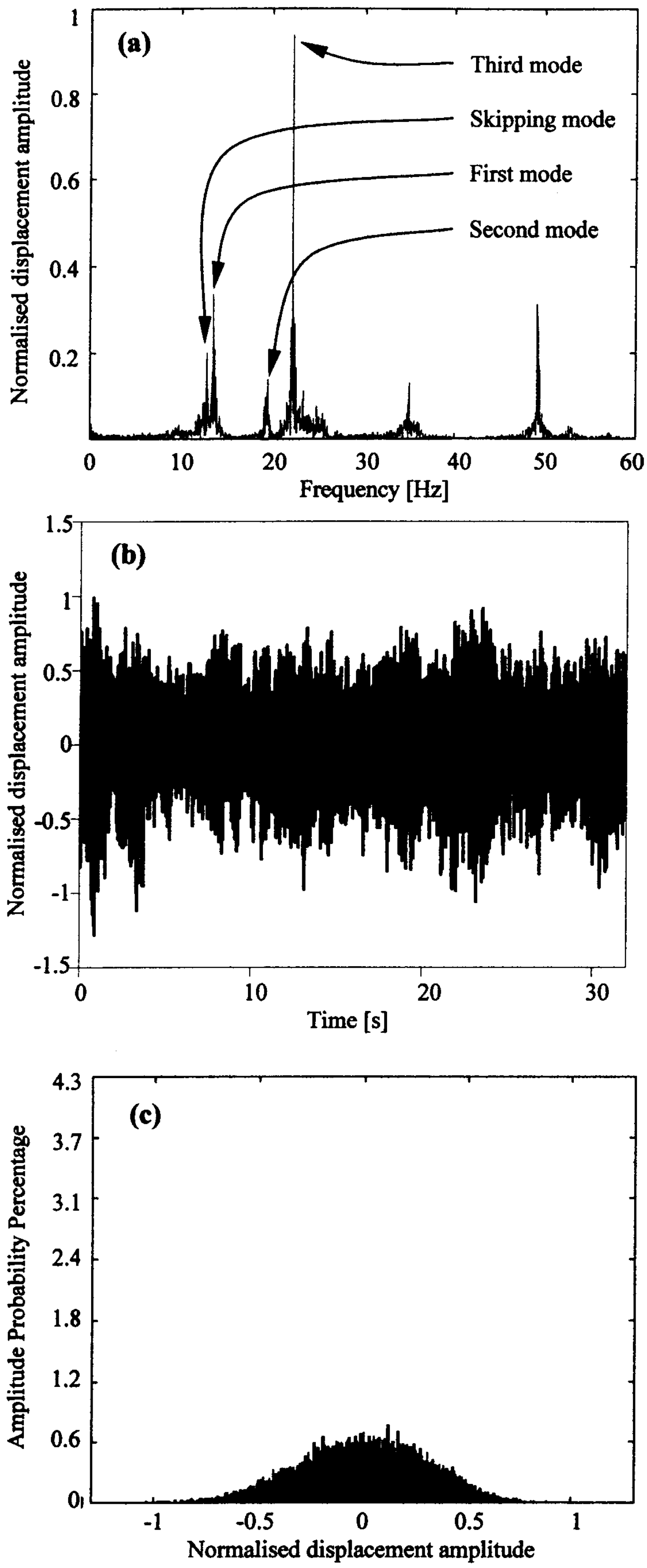

Figure 3.12. **(a)** FFT, **(b)** displacement history and **(c)** amplitude probability distribution for the starting geometry, Beam 3, of L_g/L = 0.77 and end diameter, d_g = 30mm

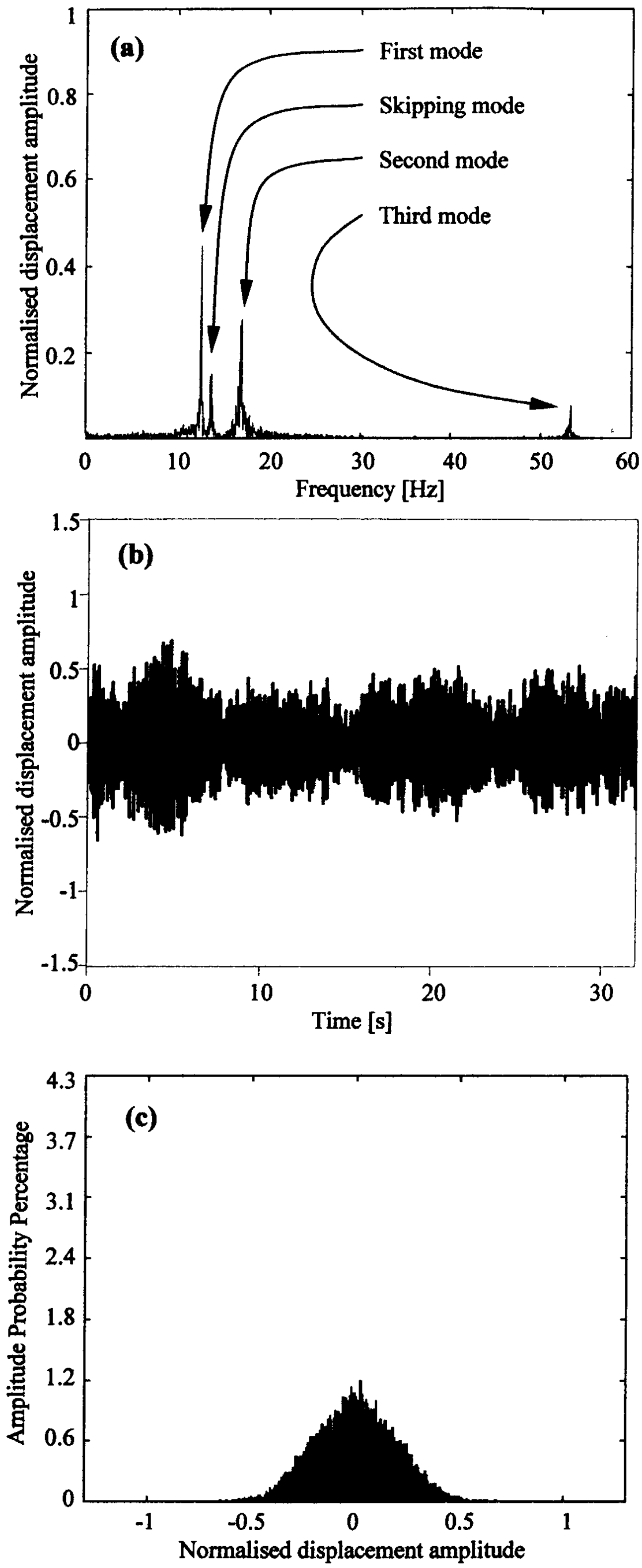

Figure 3.13. Same as Figure 3.12, but for Beam A, of L_g/L = 2 and end diameter, d_g = 30mm

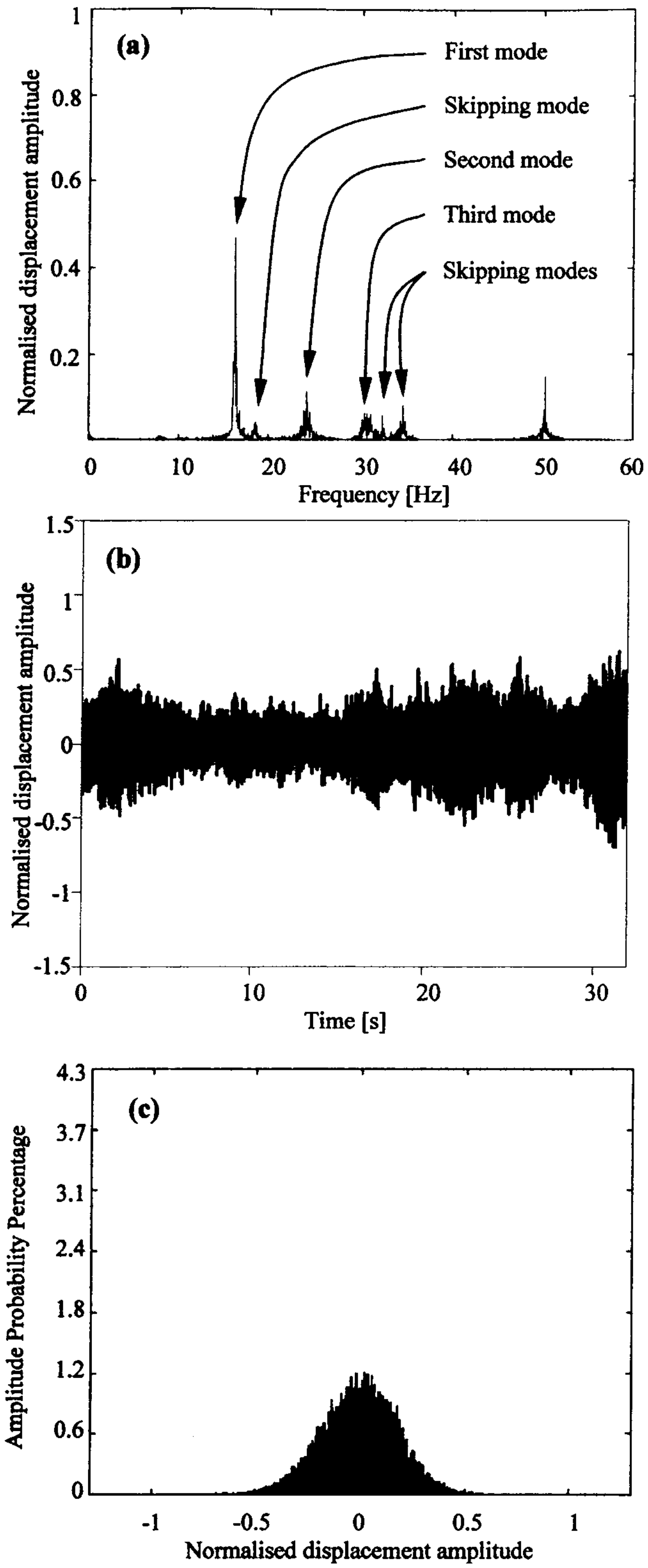

Figure 3.14. Same as Figure 3.12, but for Beam B, of $L_g/L = 0.77$ and end diameter, $d_g = 45$mm

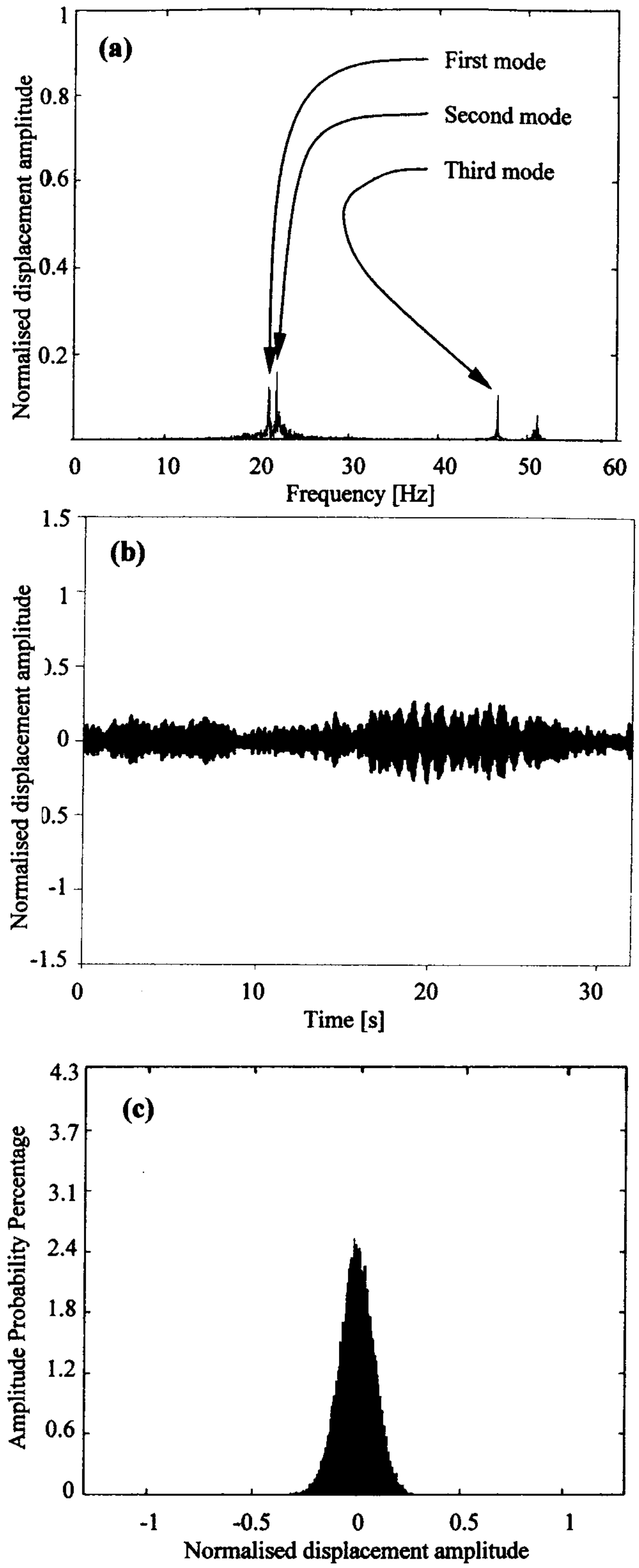

Figure 3.15. Same as Figure 3.12, but for Beam C, of $L_g/L = 2$ and end diameter, $d_g = 45$mm

In Table 3.2, the last column shows the experimental and numerical normalised rms displacement amplitudes at the mid-span. The experimental excitation point was different to the numerical one due to space considerations. However, the measurement point was similar for both the numerical and experimental observations. Numerically, Beam A, due to its close first and second natural frequencies, is expected to have a vibration amplitude reduced by 75% in comparison with that of Beam 3. While the experimental results verify this prediction qualitatively, the reduction in the rms amplitude of Beam A, in comparison with that of Beam 3, is only about 40%. Further differences are seen for Beam B, where a reduction of just over 40% in rms was measured, whereas 15% less rms displacement than that of Beam 3 was predicted numerically. Beam C is the only geometry for which the measured and predicted results agree, and about 73% and 82% reduction, respectively, in the rms displacement, is achieved.

The only beam not to exhibit any skipping modes was Beam C, possibly due to its first and second plane modes being almost coincident. This observed result is in agreement with the numerical prediction, since this geometry was predicted to be the least susceptible to large amplitude vibrations. In the experiments, when allowed to vibrate freely in response to a transient input, a node clearly travelled up and down the sensitive length of this beam. It attempts to have both mode shapes exist simultaneously. Since the second natural frequency is slightly larger that the first, a travelling node is formed. This travelling node prohibits the natural vibration modes from building to resonance.

Figures 3.12(b), 3.13(b), 3.14(b) and 3.15(b) show the normalised displacement histories of the experimentally measured data for each beam. The axes for all four plots are the same so that comparisons may be made easily. Another form of comparison among the four geometries' displacement history is shown with the percentage probability distributions in Figures 3.12(c), 3.13(c), 3.14(c) and 3.15(c). The horizontal axis here is the same as the vertical normalised displacement amplitude axis of Figures 3.12(b), 3.13(b), 3.14(b) and 3.15(b); while the vertical axis is the percentage probability. If the vibration amplitude were always close to zero, the histograms would be tall and narrow. For a beam that is susceptible to large amplitude vibrations, the percentage probability would have a shallow and wide distribution. The taller and narrower probability distribution of Beam C in Figure 3.15(c) than that of Beam 3 in Figure 3.12(c) indicates a significant improvement over Beam 3. Beams A and B, however, show smaller improvements over Beam 3.

As indicated earlier, the presence of skipping modes must be the cause of the difference between the experimental and numerical results. While the skipping modes are difficult to avoid experimentally, they are completely removed by choosing the geometry of Beam C, which has been shown to be more stable than Beam 3 with less than 30% of the rms amplitude.

These experimental observations were considered to be promising. The next stage in the experimental verification was the actual size probe manufacture to conduct flow measurements. In the next section, the details of these measurements and experimental results are presented.

3.5 Actual Size Experimental Verification and Flow Measurements

3.5.1 Probe Manufacture

Facilities are available within Victoria University to repair broken hot-wire probes. Hence, actual size probe manufacture was done by the candidate. The prongs were made from size 10 stainless steel sewing needles, which have a diameter of 0.5mm, and they were held together using 5-minute Araldite Epoxy Resin. Wollaston wire was soldered onto the prongs using a standard electric soldering iron. Wollaston wire diameters of d=2.5μm with d_g=71μm, and d=5μm with d_g=82μm were used.

Figure 3.16 shows a photograph of the probe manufacture workstation. The Zeiss microscope, item 1, provides a clear view of the wire and prongs, with the help of the light source, item 2. The prongs and Wollaston wire are held in the micromanipulator, item 3. Item 4 in this figure is the welding station.

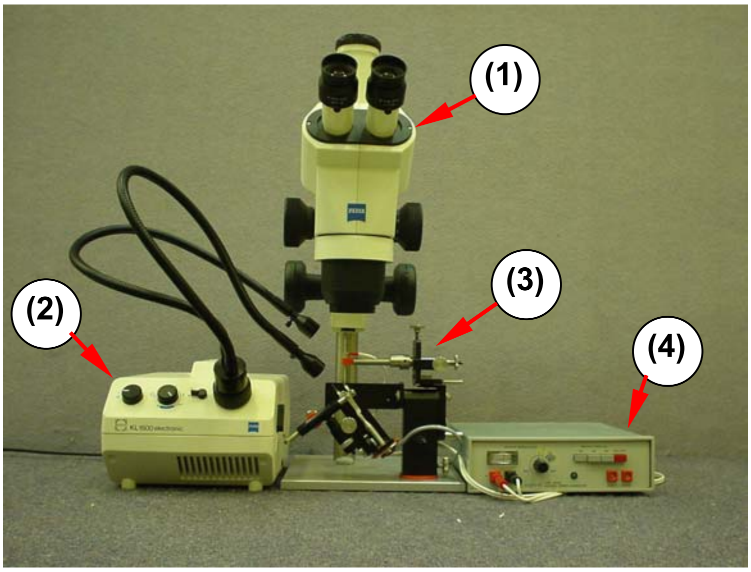

Figure 3.16. Photograph of the probe manufacture workstation showing

(5) Zeiss Stereo microscope, Stemi 2000-C 0.65-5.0.
(6) Light source, Schott KL1500 Electronic 15V 150W Halogen Lamp.
(7) DANTEC Micromanipulator, Type 55A13.
(8) Weld station, Type 55A12 Power Generator.

To make each probe, the prongs were cleaned first using a fine, 1000 grade, sandpaper. Next, a small amount of solder was plated onto the end of each prong to form a small droplet. Non-corrosive paste flux was used to hold the wire onto the prongs. The soldering iron was then gently touched onto the side of the prong to melt the already positioned solder. Thus, the Wollaston wire sank into the molten solder, securely fastening it to the prong. Once the wire had sunk into the molten solder the soldering iron could be removed, then the process was repeated for the other prong. After the wire was securely fastened to both prongs, the excess wire was removed by repeated bending until the fatigue limit was reached and failure occurred. Fortunately, this only took two or three cycles. Soldering the wire was the preferred method of attachment rather than welding, which took much longer with less reliable results.

The Wollaston wire was then etched using concentrated nitric acid. Rather than a pipet arrangement, a meniscus was used to direct the acid. A 1mm-diameter silicone tube was dipped into nitric acid, and a small amount of it was drawn into the tube using a syringe. The tube was then positioned next to the wire to be etched using the DANTEC micromanipulator, item 3 in Figure 3.16. The other end of the tube was then gently pinched to cause the acid in the tube to be forced out slightly. Care was taken to form a meniscus without letting the acid drip away. This meniscus was then moved into contact with the wire to begin the etching process as shown in Figure 3.17. The length of wire to be etched could be adjusted by moving the meniscus closer to or further away from the wire. Achieving the desired sensing length, L, under the microscope, required a trial and error procedure. The etching process took between 15 and 45 minutes depending on which diameter of Wollaston wire was used. After etching, a spray of water from a syringe diluted any traces of nitric acid remaining on the wire. The wire and prongs were then cleaned using acetone.

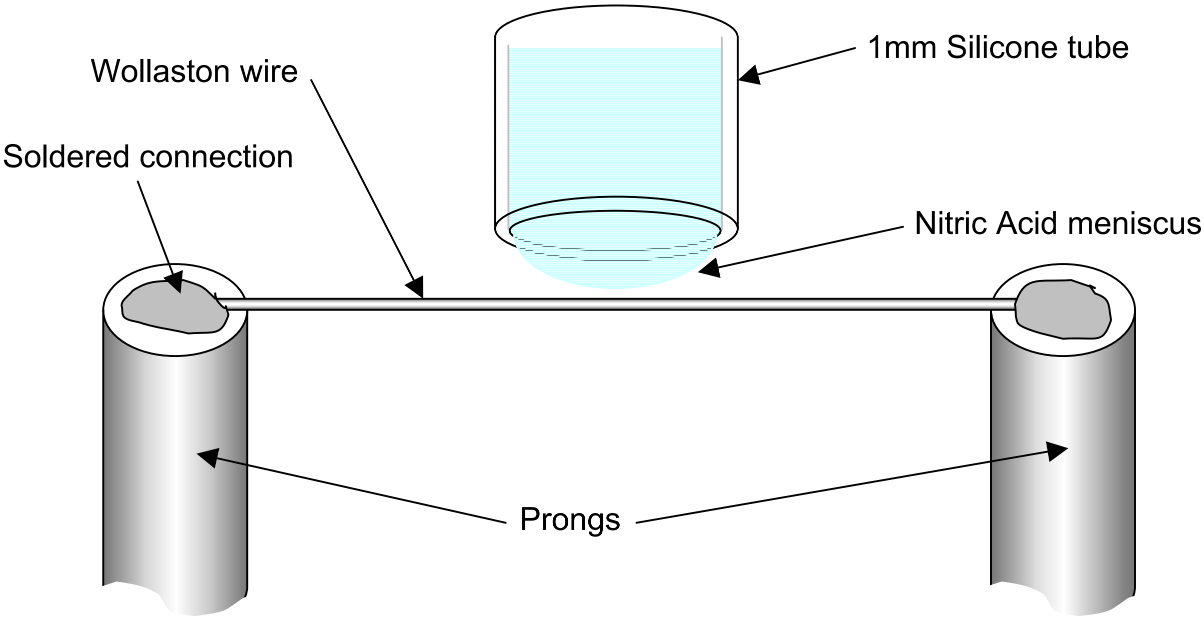

Figure 3.17. Schematic representation of the etching process using an acid meniscus.

3.5.2 Experimental Setup and Wire Parameters

Once the selected probes were manufactured, measurements were conducted just outside a fully developed turbulent pipe flow. The experimental setup used for this purpose is illustrated in Figure 3.18. The throttled fan is capable of generating mean centreline wind speeds of up to 38m/s. At the highest speed, the Reynolds number, Re, at the pipe exit is 230000, based on the mean centreline velocity. The pipe is 18m long, and it is made from drawn mild steel with an internal diameter of 108mm and has a smooth interior surface. It has sufficient length to ensure fully developed turbulent pipe flow conditions at the exit [21].

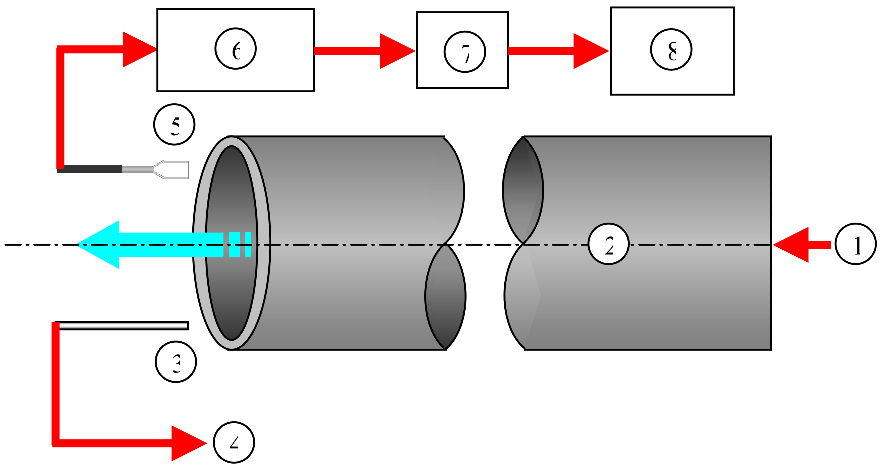

Figure 3.18. Schematic diagram of the experimental set-up.

(1) Fan
(2) Steel Pipe: L = 18m, I.D. = 108mm
(3) Pitot tube: I.D. = 1mm
(4) Micromanometer: Furness Controls Limited FC012
(5) Hot-wire Probe with 90 degree probe support and 4m cable
(6) Dantec Streamline 90N10 Frame CTA Module 90C10
(7) Keithley Metrabyte STA-U DAS58 Universal Screw Terminal Accessory Board
(8) Pentium 166MHz Personal Computer with 64MB RAM

The hot-wire probes were positioned 13.2mm from the pipe wall, and 2mm downstream of the pipe exit to enable wire observation during measurements. For this purpose, the Zeiss microscope, item 1 in Figure 3.16, was mounted above the probe wire at the pipe exit. A 1mm-inner-diameter Pitot tube was mounted in the mirror image position at the bottom wall of the pipe to monitor mean velocity calibration. Measurements were taken using a DANTEC Constant Temperature Anemometer (CTA), Streamline. For calibration and data acquisition, the accompanying software, Streamware, was used. Each wire was calibrated using at least 20 measurement points of known velocities. A power law line of best fit was then calculated through the 20 points. The calibrated data was then recorded on a desktop computer via the Metrabyte data acquisition board using a sampling frequency of 100kHz, for just over 5 seconds, giving a total of 524288 points. Higher sampling frequencies were tested, but there were clearly no spectral components present above 50kHz, so 100kHz was deemed to be sufficient. Post processing was done using Matlab® [10].

Separate measurements were taken using seven different probe geometries at the same position in the flow. The first probe used was a DANTEC 55P05, which has the dimensions shown in Table 3.3. The other six geometries shown in Table 3.3 were made in the laboratory. Probes 2 and 3 (not listed in Table 3.3) were manufactured but met with unfortunate accidents before measurements were completed, such as the one shown in Figure 3.19.

Table 3.3. Geometric and measurement data for the seven probes under analysis.

PROBE	DANTEC	1	4	5	6	7	8
L_g [mm]	0.95 ±0.01	0.92 ±0.01	1.14 ±0.04	1.21 ±0.01	0.73 ±0.03	1.11 ±0.02	1.11 ±0.01
L [mm]	1.10	1.23	0.77	0.57	1.37	0.91	0.56
L_o [mm]	3.00	3.07	3.05	3.00	2.82	3.12	2.78
L_g/L	0.87 ±0.01	0.75 ±0.01	1.48 ±0.05	2.13 ±0.01	0.53 ±0.02	1.22 ±0.02	1.98 ±0.02
d_g [μm]	40	71	71	71	82	82	82
d [μm]	5.75	2.5	2.5	2.5	5	5	5
L/d	191.3	492	308	228	274	182	112
$\bar{U}$ [m/s]	32.2	31.55	30.93	31.92	31.43	33.22	32.35
ε [m^2/s^3]	232	267	414	426	229	222	294
$\sqrt{\overline{u'^2}}$	5.92	6.30	6.01	7.67	6.19	6.46	6.32
f_{n1} [kHz]	12200	4000	11000	17500	5600	16600	20600
f_{n2} [kHz]	12800	11800	20900	17600	15600	26200	20700
f_{n3} [kHz]	20000	23100	21000	20000	30900	26300	35000
Normalised static deflection	1	90	20	8	6.5	2	0.5

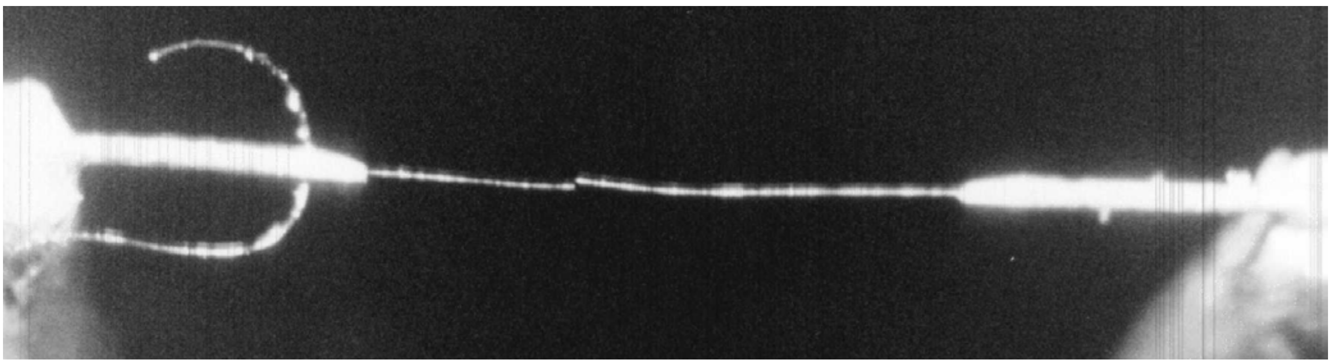

Figure 3.19. Photograph of probe 2 after a piece of fluff (shown on left hand side) hit the wire during measurements and broke the sensitive length. Magnification is 52 times.

In table 3.3, the first group of parameters represent the geometric features of the 8 probes. These were measured with the microscope. Out of these, the very last row indicating L/d is of significant importance. As discussed earlier, a range between 160 and 310 was reported in the literature as being necessary for accurate measurements. The low end of the range leads to insensitivities due to conduction loses to the prongs. The high end leads to insensitivities due to spatially averaging the small scales in the flow. Spatial averaging, of course, takes place for any finite length where the ideal condition is a sensing wire of 'zero length' to enable accurate sensing of all scales in the flow.

The second group in Table 3.3, represent the mean flow velocity, Ū, rate of dissipation and the rms of the fluctuating velocity component in the flow, $\sqrt{\overline{\mathbf{u}'^2}}$. The next three rows indicate the numerically predicted structural resonance frequencies. Finite element modelling and the measured geometric and material properties were used to obtain these predictions.

The very last row in this table indicates the equivalent stiffness of the probe wires. These numbers were obtained after numerically integrating their finite element approximation to obtain the history of the displacement in the mid-span. After Fourier transforming these displacement histories, the spectral components corresponding to the zero frequency (static deflection) are reported here. A small value of static deflection indicates a 'stiff' structure, whereas a large value corresponds to a more flexible one since all wires were excited by the same forcing function.

3.5.3 Measurements

From the velocity trace of each probe, the mean value was removed, and a fast Fourier transform (fft) was performed on the fluctuating component. Each data record was split into 52 equally sized intervals so that an averaged fft or auto spectrum could be obtained. Each interval had 10000 points to give a frequency resolution of 10Hz. Although higher frequency resolutions, such as 2Hz, were tried, no additional information was gained. The auto spectra were scaled so that the area under the graph equalled the mean square of the velocity fluctuations.

The frequency axis of the auto spectrum was converted into the one-dimensional longitudinal wave number, k_1, scale using the following:

$$k_1 = \frac{2\pi f}{U}$$

where f is the frequency of velocity fluctuations in Hz, and

$\bar{U}$ is the longitudinal mean velocity in m/s.

The rate of dissipation is calculated by:

$$\varepsilon = 15\nu \int_0^\infty k_1^2 E_1(k_1) dk_1$$

where ν is the kinematic viscosity, and

$E_1(k_1)$ is the one-dimensional energy spectrum of the longitudinal velocity fluctuations, u, given as follows:

$\overline{u^2} = \int_0^\infty E_1(k_1) dk_1$ representing the mean square average of the velocity fluctuations.

3.5.4 Experimental Results

The auto spectra, or energy spectra, for each wire geometry given in Table 3.3, is plotted in Figure 3.20 in the same order of presentation as in Table 3.3. It is notable that all seven wires show comparable energy spectra for small k_1 values. This is an expected result since previously reported experimental findings showed that the sensitivity of a hot-wire probe to large-scale fluctuations was independent of the wire dimensions [8]. Therefore, energy spectra do not provide clear indications of high frequency response to small-scale fluctuations. The energy spectra are presented here only for completeness. It may be worth mentioning that the spectral spacing is quite wide here (as a result of the 10 Hz frequency spacing) to represent the large scales in the flow properly. However, this rather rough representation is not considered to be detrimental. It is the high frequency, small-scale, fluctuations that are of interest since the hot-wire response to small-scale fluctuations is highly influenced by wire geometry. Dissipation spectra are used for this purpose.

High frequency, small-scale behaviour can be seen clearly in a plot of dissipation spectra. The dissipation spectrum $k_1^2 E_1(k_1)$ obtained with each probe is plotted against one-dimensional longitudinal wave number, k_1 in Figure 3.21, again in the same order as in Table 3.3. Before the distribution of dissipation spectra is discussed, it may be worthwhile to briefly present the resultant rate of dissipation obtained with different wires. Rate of dissipation here represents the total area under the $k_1^2 E_1(k_1)$ versus k_1 plots.

The dissipation rate values for the seven probes are plotted in Figure 3.22 against sensitive wire length. The rate of dissipation plotted against wire length, as in Figure 3.22, is expected to give a straight line, which intersects the vertical axis at the zero wire length (ZWL) dissipation value. This technique is based on linearly extrapolating the dissipation rate measured with hot-wire probes of different sensitive lengths to zero wire length [12]. The ZWL dissipation rate was shown to be a good estimation of the 'true' rate of dissipation in fully developed turbulent pipe flow. The 'true' rate of dissipation is taken to be the value obtained from turbulence kinetic energy balance. This technique is applied here as a guide, only, since the present measurements were taken outside the pipe, and no other turbulence measurements exist for the same location to compare these results with.

As discussed in the previous paragraphs, some scatter exists in the results. However, a straight line of best fit can be drawn through points 1,4,5,6 and D. It appears that Probes 7 and 8, which have a small L/d combined with thick wire diameters, correspond to low values of the rate of dissipation compared to the line fit.

Now, going back to spectral distributions, in Figure 3.21(a), the dissipation spectrum obtained with a standard DANTEC 55PO5 boundary layer probe is presented. This probe has a sensitive length of L=1.10mm, d=5.75μm and d_g=40μm. It is used here as the datum, since it is currently one of the most widely accepted probes for general use [8]. This plot represents a typical dissipation spectrum with the exception of four small isolated spectral peaks which occur for k_1 values of 3.7×10^3, 4.1×10^3, 5×10^3 and 8×10^3. Judging by the sharpness of these peaks, they are speculated to be associated with electronic circuitry. They occur roughly at the same frequencies in Figures 3.21(a)-(g). The rate of dissipation for this probe is 232 m^2/s^3.

The dissipation spectrum of Probe 1 is shown in Figure 3.21(b). As shown in Table 3.3, this probe has well-separated natural frequencies. It has a large L/d of 492, corresponding to a sensitive length of 1.23mm, making it susceptible to spatial averaging effects [19]. In addition, it is 90 times more flexible than the Dantec probe as indicated in the last row of Table 3.3. The spectrum of this probe is included here only as an example of how such a wire geometry can gibe a distorted spectrum. The rate of dissipation for Probe 1 is 267m^2/s^3.

Based on the earlier L/d arguments alone, Probe 4 would have been deemed acceptable with its L/d of 308, and a sensitive length of 0.77mm. However, as indicated in Table 3.3, it has its first natural frequency (11kHz) well separated from the second (20.9kHz) and third (21kHz) natural frequencies. The dissipation spectrum in Figure 3.21(c) shows a significant dip, believed to be due to wire resonance. This dip, however, occurs in the vicinity of $k_1=3.5\times10^3 m^{-1}$ corresponding to approximately 17kHz. The rate of dissipation for Probe 4 is $414 m^2/s^3$, with its shorter sensitive length than that of the Dantec wire, this value is as expected. The flexibility of Probe 4, 20 times higher than Dantec's, seems also to contribute to a distorted spectral distribution similar to that in Figure 3.21(b).

The dissipation spectrum of probe 5 also exhibits a significant dip as shown in Figure 3.21(d). This dip corresponds to a k_1 of 1.2×10^3 m^{-1}, or approximately 6kHz. In Table 3.3, the first natural frequency of Probe 5 is shown to be 17.5kHz. Although the first and second frequencies are close, this probe has the third frequency in close proximity. Previous work showed this scenario to be detrimental to reduce the suppression effect of the second mode on the first mode [22, 23]. Probe 5 has a dissipation rate of 426 m^2/s^3 and a somewhat distorted spectral distribution similar to those in Figures 3.21(b) and 3.21(c).

Probe 6 also has an acceptable L/d of 274 with a sensitive length of 1.37mm. Such a large sensitive length can lead to spatial averaging along the wire as mentioned earlier for Probe 1. This geometry is also predicted to be susceptible to wire resonance. Analysis of Figure 3.21(e), the dissipation spectrum for this probe, reveals a small dip at k_1=1.7$\times$10^3 m^{-1} corresponding to a frequency of around 8 kHz. At around 6 kHz, this geometry's first natural frequency was predicted to be well separated from the second and third. It is thought that the dip would have been much larger if the spatial averaging effect was not present, since spatial averaging seems to have a smoothing effect on the data. This wire has a sensitive length slightly longer than that of the DANTEC wire. A comparable rate of dissipation of 229 m^2/s^3 to that of the DANTEC probe, was measured with Probe 6.

The dissipation spectrum obtained with Probe 7 is shown in Figure 3.21(f). Probe 7 has an acceptable L/d of 182 and a sensitive length, L, of 0.91 mm. The predicted first natural frequency of this geometry was around 17 kHz, and its second and third natural frequencies were predicted to be both close to 26 kHz. Since the first natural frequency is well separated from its neighbours, a dip in the dissipation spectrum would be expected. The dissipation spectrum however, does not exhibit any dip. The first three natural frequencies for this geometry are within the excitable range, which includes frequencies up to 25 kHz (corresponding to k_1=5$\times$10^3 m^{-1}). This wire has a slightly shorter sensitive length than the DANTEC wire. A slightly smaller dissipation rate, 222 m^2/s^3, was obtained with it than that measured with the DANTEC probe.

The final probe geometry for discussion here is Probe 8, which has an unacceptable L/d of 112 and sensitive length of L=0.56 mm. The natural frequencies of Probe 8 are distributed very favourably. It has an equivalent structural stiffness twice as much as that of the reference DANTEC probe. As expected, the dissipation spectrum of Probe 8 in Figure 3.21(g) demonstrates a smooth curve with no indication of dips. This wire has a dissipation rate of 294 m^2/s^3, higher than that of DANTEC's with its shorter sensitive length.

In summary, dissipation spectra of various probes in Figure 3.21 demonstrate that not only the well recognised L/d but also the structural parameters may have an important role in the accuracy of small scale measurements. Probes of low structural stiffness (Probes 1, 4, 5) may significantly distort the spectra towards small scales. Probes with well separated first natural frequencies within the range of flow excitation (Probes 1,4 and 6) or with close first, second and third natural frequencies (Probe 5) may show an unexpected dip in their spectral distribution corresponding to loss of sensitivity due to structural resonance as discussed earlier in Section 3.1. It is also apparent from the clear mismatch between the predicted structural frequencies in Table 3.3 and the spectral displacement in Figure 3.21 that accurate prediction of the structural natural frequencies is quite difficult.

This lack of accuracy may be attributed to geometric imperfections and possible presence of axial tension or sag during measurements. Home-made probes have geometric imperfections such as those of boundaries, and conical transitions between the etched and un-etched sections of the Wollaston wire. These transitions are clear step changes in the numerical model. In addition, ideal boundary conditions are imposed numerically opposed to less than perfect connections possible in the real wires.

Although it is almost impossible to accurately account for the presence of an axial force on a probe wire during measurements, these axial forces do not change the relative proximity of the natural frequencies. An axial tension increases whereas sag, as a result of axial compression, reduces the numerical values. However, any probe wire with well-separated frequencies is expected to retain its character even though the values of these frequencies may be displaced. Therefore, resonance dips in the dissipation spectra at a frequency different than that of the numerical predictions may not be too surprising considering the possible differences between real probe operating conditions and the corresponding ideal numerical model. What is pleasing, however, is that despite the differences, it is still possible to predict the presence and absence of resonance effects to a great extent.

3.6 Conclusions

In this chapter, a general approach has been developed for vibration control with coincident first and second natural frequencies. This control of structural response is demonstrated both numerically and experimentally with a scaled-up hot-wire model. In addition, a procedure to manufacture hot-wire probes has been developed in order to apply the control principles to flow measurements.

Flow measurements showed that structural resonances did not have a significant enough effect on the total rate of dissipation. However, anomalies related to spectral dips due to structural resonances can now be explained with the material presented here.

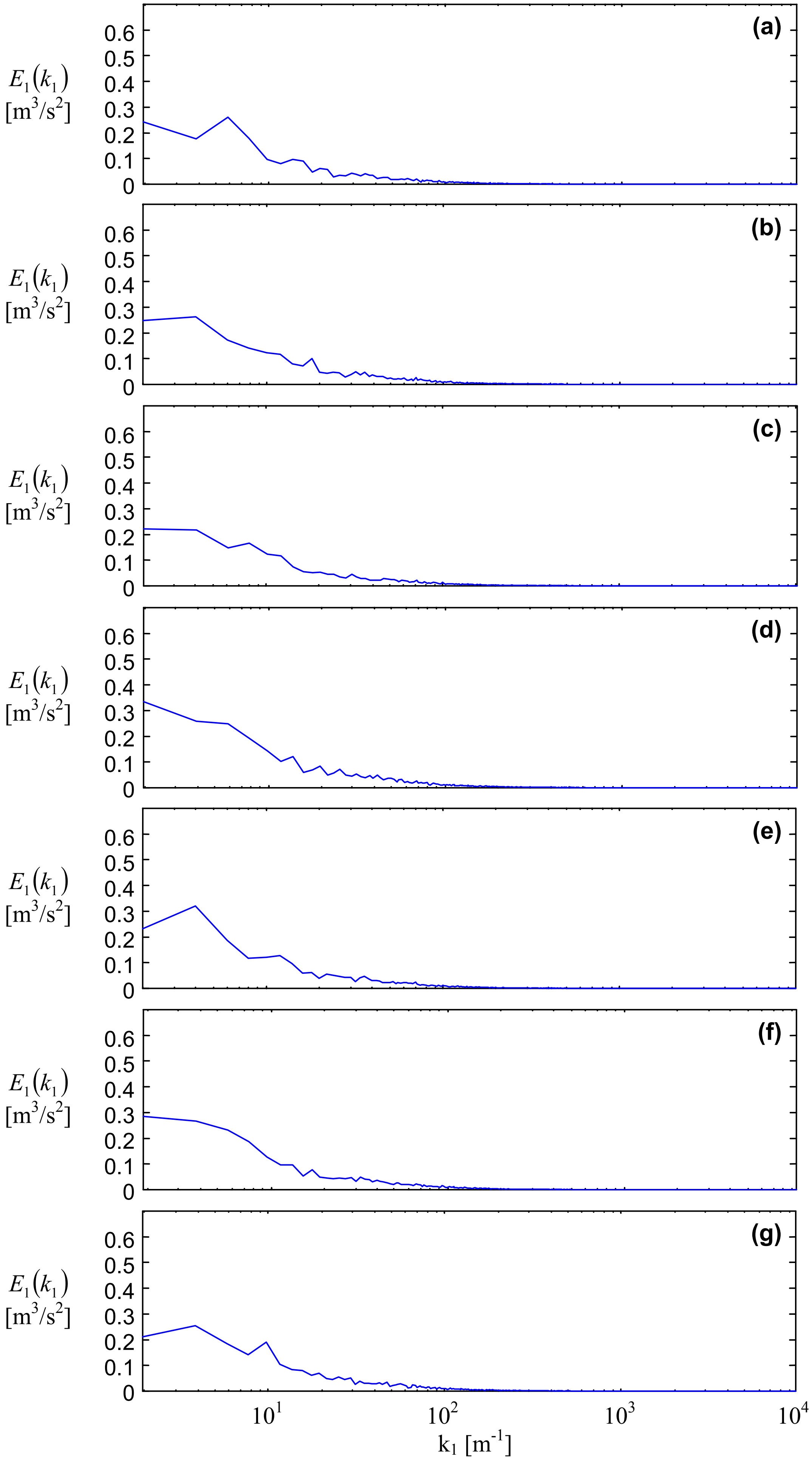

Figure 3.20. Energy spectra for the seven probe geometries listed in Table 3.3: **(a)** DANTEC, **(b)** Probe 1, **(c)** Probe 4, **(d)** Probe 5, **(e)** Probe 6, **(f)** Probe 7 and **(g)** Probe 8.

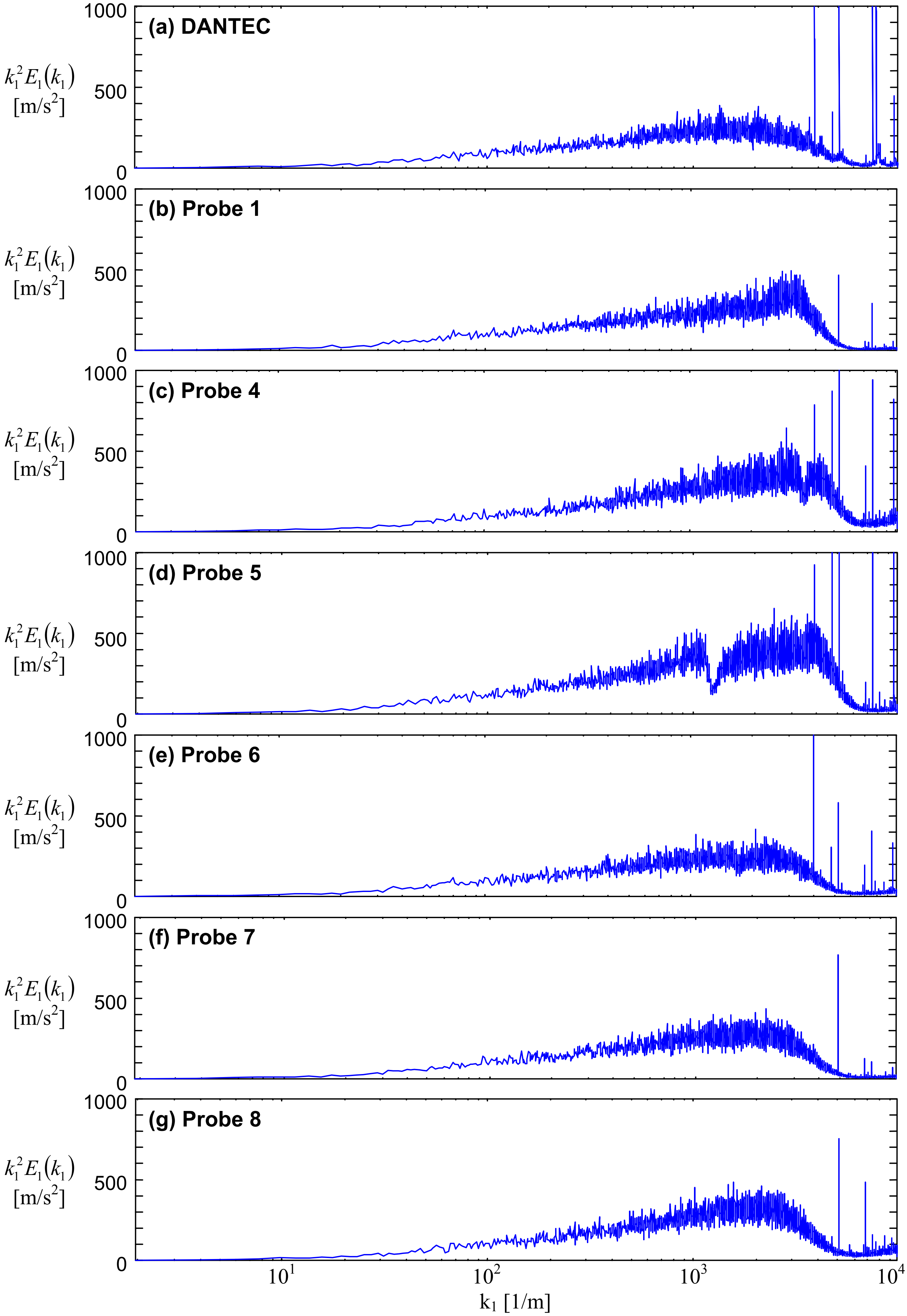

Figure 3.21. Dissipation spectra for seven probe geometries listed in Table 3.3: **(a)** DANTEC, **(b)** Probe 1, **(c)** Probe 4, **(d)** Probe 5, **(e)** Probe 6, **(f)** Probe 7 and **(g)** Probe 8.

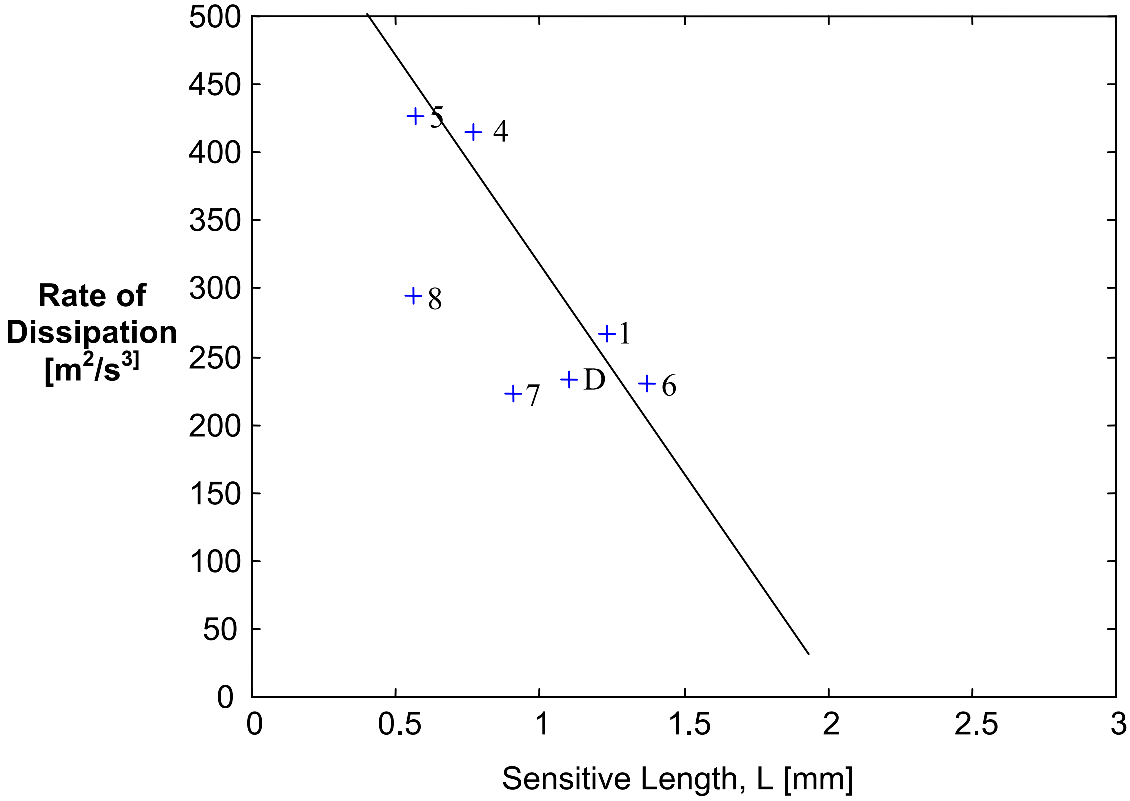

Figure 3.22. Rate of dissipation of turbulence kinetic energy as measured by the seven different hot-wire probes under analysis in the fully developed pipe flow.

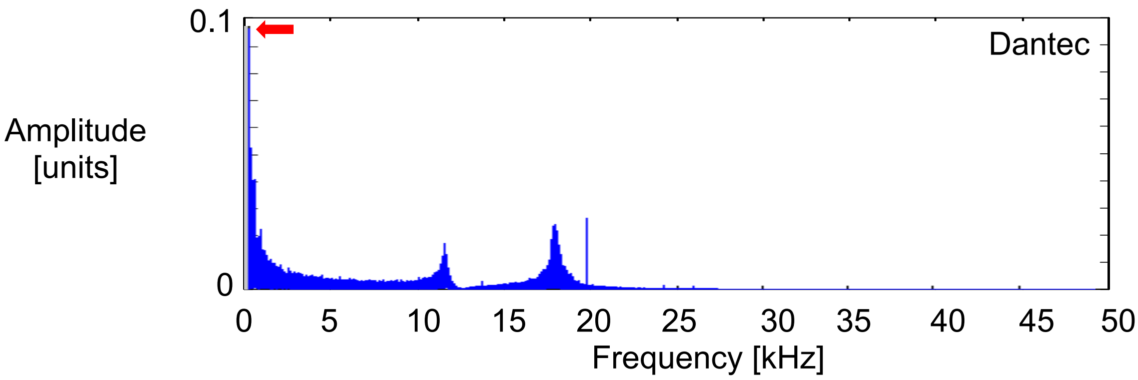

Figure 3.23. Displacement amplitude spectrum of the DANTEC probe using the measured velocity data as the excitation input.

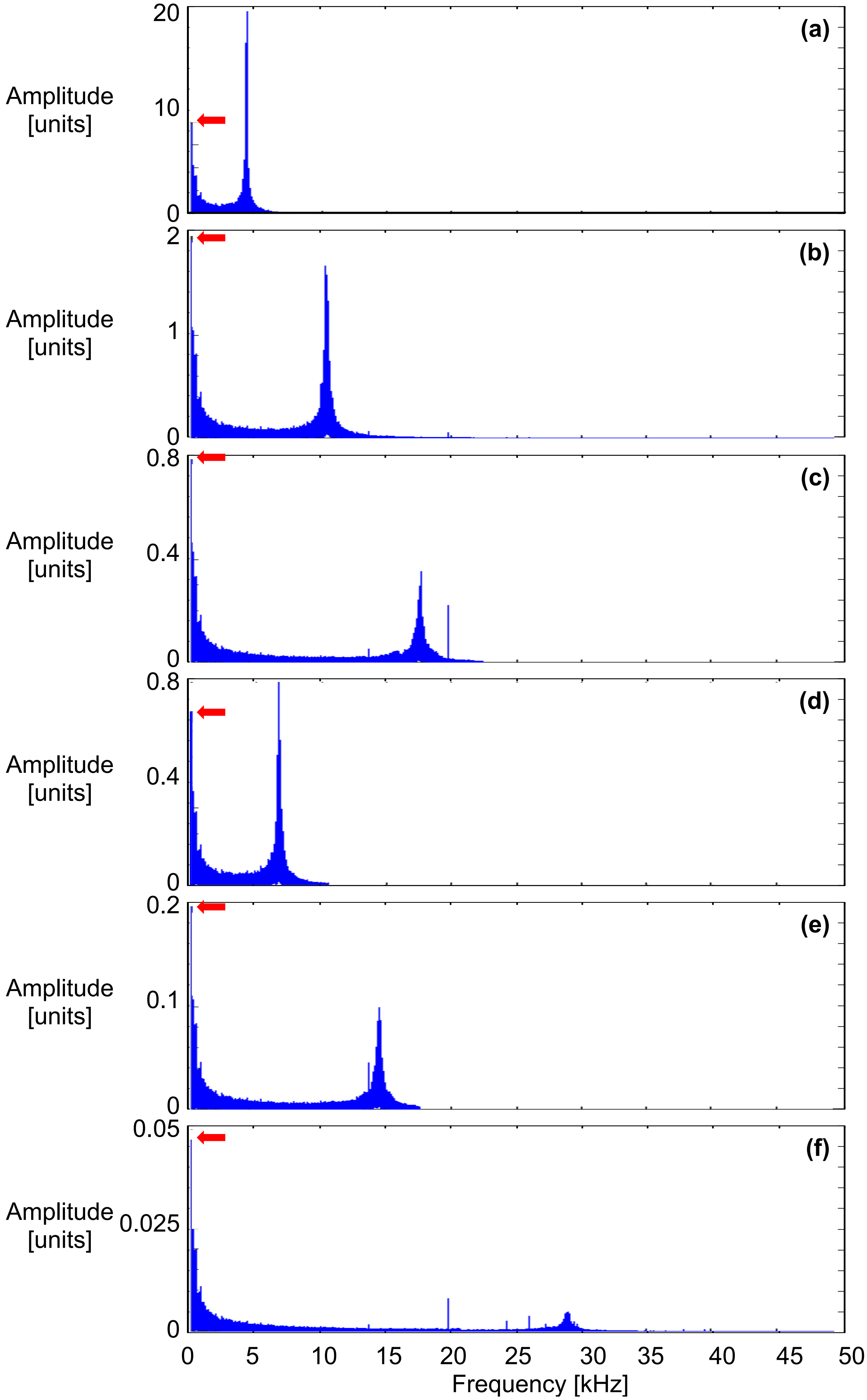

Figure 3.24. Displacement amplitude spectra for **(a)** Probe 1, **(b)** Probe 4, **(c)** Probe 5, **(d)** Probe 6, **(e)** Probe 7 and **(f)** Probe 8. The red arrows point towards the zero frequency static deflection.

Chapter 4

MILLING TOOL CHATTER

4.1 Introduction

The control procedure suggested in the preceding chapters of this thesis is applied next to an excessive vibration problem in a manufacturing procedure. The nominated problem is the chatter instability in end milling.

Chatter is a self-excited vibration problem, resulting from the unavoidable structural flexibility at the point of cut where the cutting tool and work piece interact. It occurs at large rates of material removal when the removal rate exceeds critical stability limits. When uncontrolled, chatter causes a rough surface finish, dimensional inaccuracy of the work piece, unacceptably loud noise levels and accelerated tool wear. In general, chatter is one of the most critical limiting factors to be considered when designing a manufacturing process.

Studies of chatter date back over half a century such as those by Arnold [24] and Merchant [25]. Basic understanding of the problem, including the mechanism of surface regeneration, mode coupling and association with structural dynamics, were postulated more recently by Tobias [26] and Tlusty [27, 28]. Their continued works with collaborators have provided the frame of current chatter research.

The cutting force can be assumed to be proportional to the thickness of the chip to be removed from the work piece. The dynamic response of the structure causes the instantaneous chip thickness to vary in time. Hence, the cutting force, which is the reason for vibrations, feeds on the structural dynamics. This process is generally termed as 'primary feedback'. A fluctuating chip thickness leaves behind undulations on the cut surface of the work piece. These undulations are "read" by the following passes of the tool resulting in an additional contribution to the dynamic fluctuations. This additional effect is termed as 'surface regeneration' or 'secondary feedback'.

While the fundamental understanding has been well established, numerous practical issues to effectively control chatter still remain to be resolved as an active field of research. Chatter suppression techniques range from monitoring/prediction procedures to remedial control strategies. The objective of monitoring procedures is to slow the waste removal rate to suppress chatter, once the occurrence of chatter is determined [29, 30]. Remedial techniques, on the other hand, are more proactive as they attempt to suppress the dynamic response of the structure while a high rate of waste removal is maintained. These include sensing the structural response and imposing a corrective effort to negate it [31, 32], actively interfering with the cutting parameters to avoid the feedback [33, 34], and using auxiliary devices to suppress excessive oscillations [35, 36]. The list of referred publications given here is by no means exhaustive, only representative.

The approach taken here is to accept the presence of the feedback processes rather than attempting to interfere with them. Then the problem of control becomes one of developing a procedure to suppress the dynamic response of the structure to delay the occurrence of chatter.

The process is focussed on designing a cutter for an end mill, which is much less prone to excessive oscillations than its conventional counterpart. Hence, the approach is not much different than that in [37] and [38] where critical components of the machine structure were redesigned to enhance the chatter stability. The advantage of what is suggested here, however, is not to require any changes in the machine, but only to include an adaptor for a conventional cutter. It is, therefore, an add-on solution to existing configurations.

The rationale for the design procedure is briefly discussed in the next section. Then the numerical model and numerical predictions are given. A laboratory model of the suggested design and experimental observations are then presented with preliminary conclusions.

4.2 Suggested Control Technique

A helical end mill cutter is shown in Figure 4.1(a) where the spindle attachment is assumed to be relatively rigid compared to the structural flexibility of the cutter. Cutting takes place at the free end where the excitation to the cantilevered cutter is provided in the form of a fluctuating resistance (cutting force) of the work piece. Realistic representation of shaped cutting edges is important to obtain the feedback cutting force, which depends upon the contact geometry between the cutter and the work piece. The force feedback has been decided not to be of concern for the preliminary study presented here. Hence, it is quite justified to model the cutter as a uniform cantilever beam as shown in Figure 4.1(b) where d and L correspond to the diameter and the free overhang from the spindle.

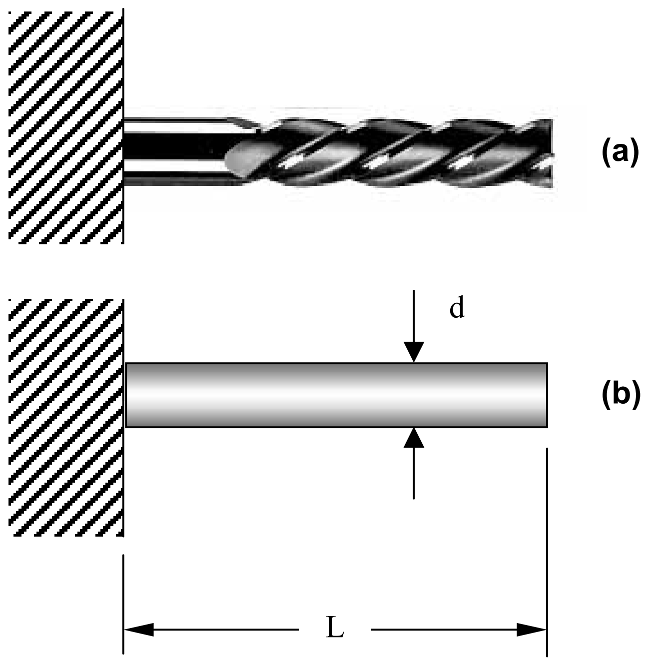

Figure 4.1. **(a)** A typical helical end mill cutter and **(b)** its simplified model cantilevered from a rigid spindle.

A uniform-sectioned cantilevered beam has its fundamental natural frequency well separated from those of the higher modes. The second and third frequencies are approximately 6 and 17 times larger than the fundamental frequency, making the structure quite vulnerable to resonance at the fundamental mode. This fact has been clearly, and repeatedly, indicated in the literature whenever the frequency content of chatter instability is reported in all the references sited earlier.

The first two mode shapes of a cantilevered beam from Chapter 2, are repeated in Figures 4.2(a) and 4.2(b). As in any structure, the fundamental mode is the most flexible one, due to its in-phase nature along the entire length. Higher modes become increasingly less flexible as they must accommodate phase changes and nodes.

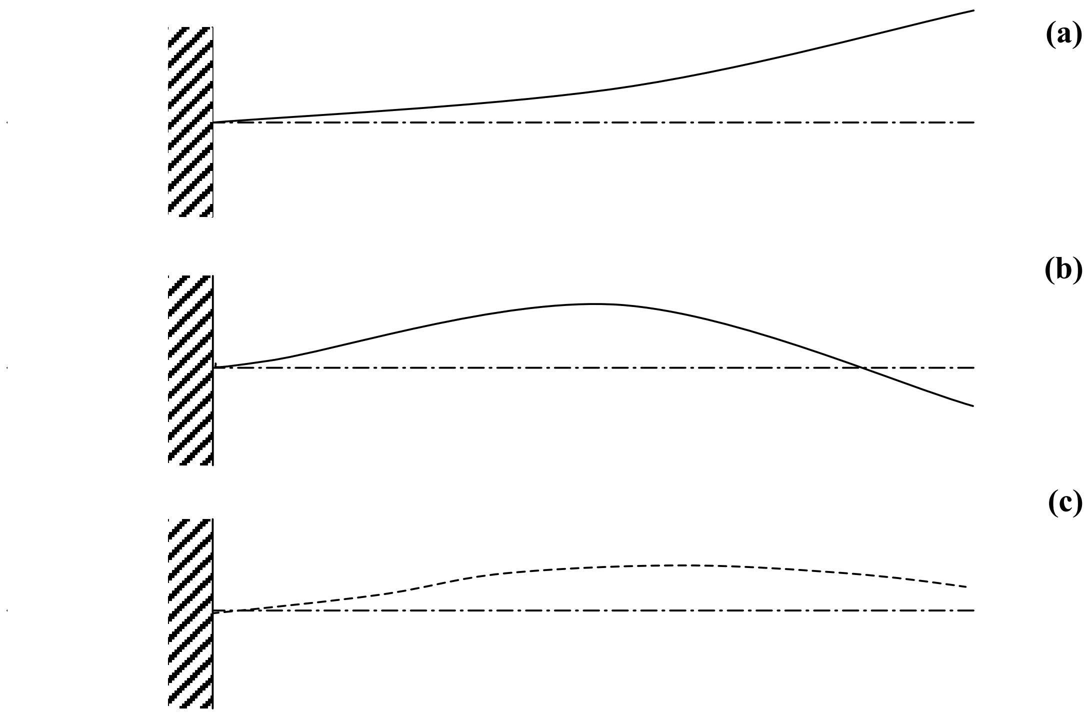

Figure 4.2. Showing **(a)** the first, and **(b)** the second mode shapes, and **(c)** their spatial average (assuming comparable peak displacements).

It is of particular interest in Figure 4.2(b) to note the location of the node of the second mode. If it were possible to force the co-existence of the first and second modes, the node of the second mode could have a restraining effect on the tip oscillations of the first mode. Such a co-existence is possible when the first and second natural frequencies of the beam are close numerically.

In Figure 4.2(c), a fictitious mode shape is suggested in which the modal displacements in Figures 4.2(a) and 4.2(b) are averaged. The two assumptions behind such an average are coincident first two modes, and comparable peak response in each mode. In practice, however, it may not be possible to have this coincidence of frequencies, and the second natural frequency is always somewhat higher in frequency than the first one. In earlier experiments [39], this difference in frequencies was observed to cause a travelling node along the beam. The first two modes took turns to exist, resulting in neither having the opportunity to establish a steady natural resonance. Attenuations were obtained as a result.

Earlier work on hot-wire design has indicated the possibility of manipulating the distribution of the natural frequencies of a beam with a stepped geometry. Design parameters in such a study would be those affecting the stepped change to identify geometries with close first two natural frequencies. The objective here, therefore, is to accommodate stepped beam geometries similar to that shown in Figure 4.3(a) for end milling. In this illustration, d and L represent the diameter and length of the cutter, whereas d_g and L_g are the relevant parameters of an adaptor to make a stepped geometry practically possible.

With the suggested design, the adaptor is attached to the spindle on one end. On the other end, the cutter is attached to the adaptor. Any improvement with the stepped geometry in Figure 4.3(a), can only be based on a performance comparison relative to the geometry shown in Figure 4.3(b) where the cutter is attached directly to the spindle of the milling machine. Inclusion of the adaptor is only sensible for geometries where the stepped beam has a smaller dynamic response than that of the cutter alone.

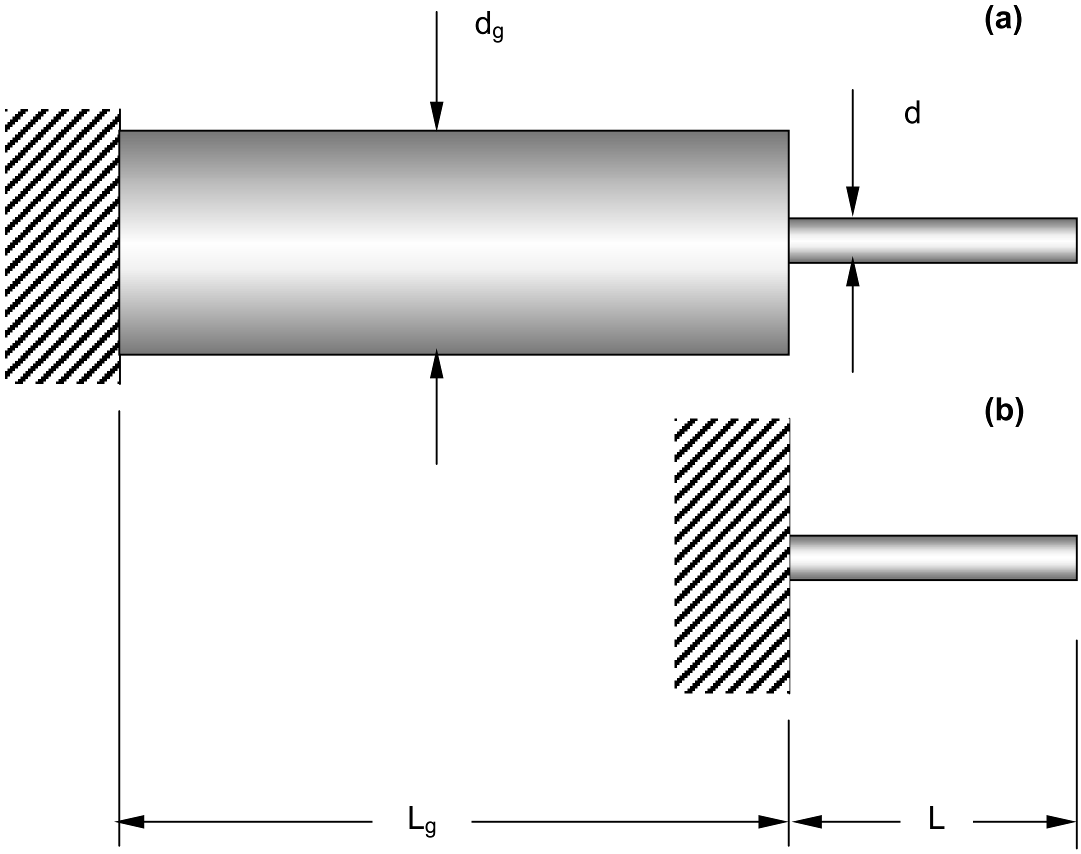

Figure 4.3. Schematic representation of the comparison between **(a)** the combined adaptor-cutter system (for $L_g/L=2.25$) and **(b)** the cutter alone.

4.3 Numerical Procedure

The numerical procedure is virtually identical to that described earlier for the hot-wire application. A brief discussion is included here to maintain the completeness of information within this chapter.

The structure in Figure 4.3(a) is modelled with standard Euler-Bernoulli beam elements [2]. A total of 20 elements, 10 for each stepped section, have been determined to be accurate enough to approximate the structural dynamics in the first five modes. The larger adaptor section was assumed to be of aluminium, whereas steel was used for the tip cutter section. This assumption was based on the availability of suitable materials for the experimental verification discussed later.

Identifying promising geometries first required determining the natural frequencies. The eigenvalue problem was solved using Matlab, once the global mass and stiffness matrices were assembled. A proportional equivalent viscous damping matrix was then assembled to give 1% critical damping in the fundamental mode.

Promising geometries were tested by exposing them to a random white noise excitation at their free end [39]. History and spectral distribution of the excitation force are shown in Figures 4.4(a) and 4.4(b). A small response to such an excitation indicates less proneness to chatter instability.

Random excitation may be considered to represent the cutting force without feedback. Once the stability is lost, feedback takes over resulting an excitation containing a narrow band of frequencies around the fundamental frequency of the structure. Hence, a second excitation of sine-swept frequencies of up to 10 kHz, was also used in an attempt to observe the response to a narrow-band excitation.

The dynamic history response was calculated by integrating the system differential equations. Newmark-β method, constant average acceleration, was used to approximate the integration of equations. The root-mean-square (rms) tip displacement was computed for both the combined adaptor-cutter system and the corresponding cutter alone.

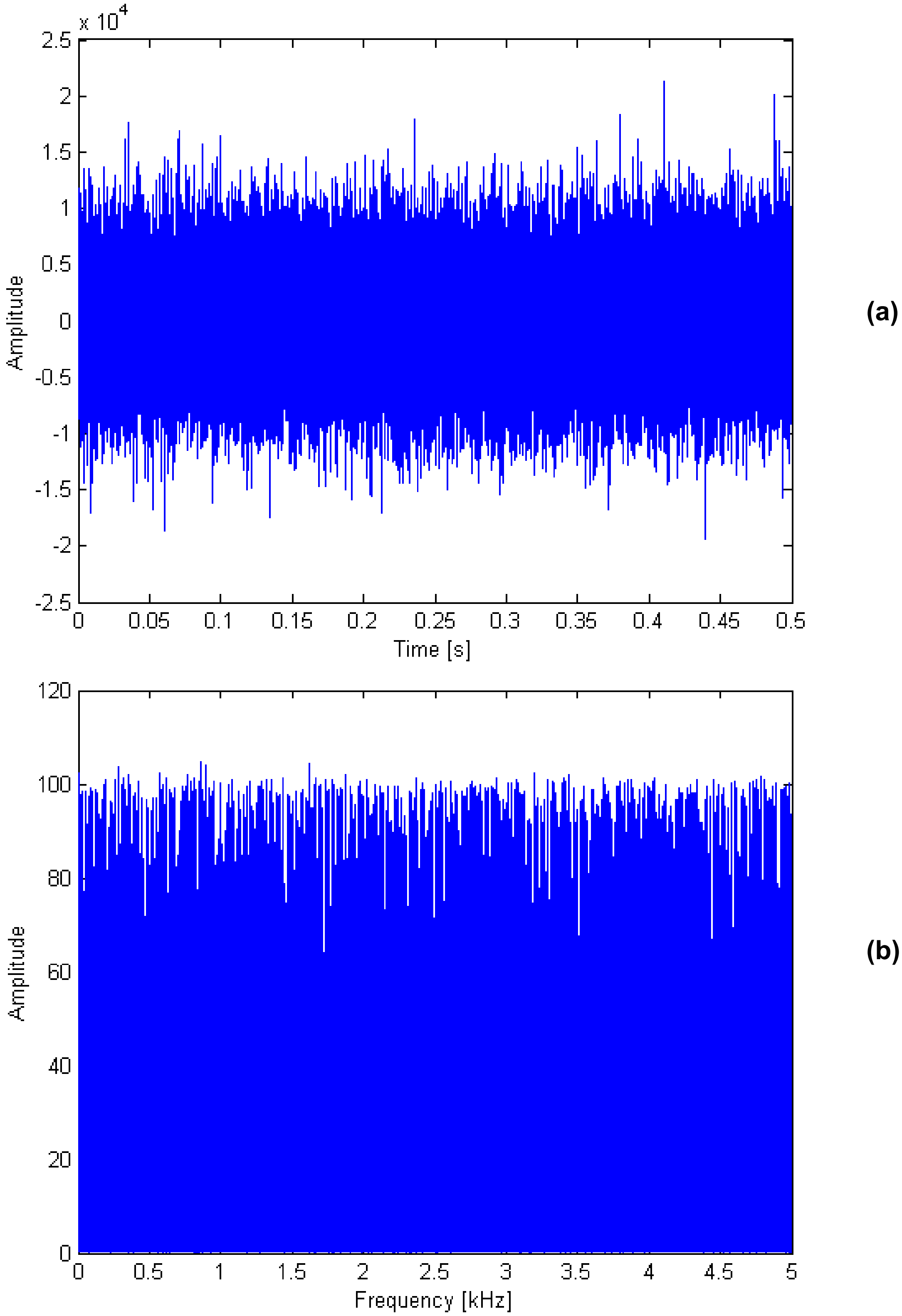

Figure 4.4. **(a)** History of the random force and **(b)** its FFT.

4.4 Numerical predictions

As mentioned earlier in Section 4.2, the method of control of excessive vibrations in the fundamental mode (by ensuring that the second mode is close to the fundamental mode) is possible if a step change in the cross section is introduced [39]. Hence, the parameters of critical importance to be determined are those relevant to a stepped change. A decision was made to simplify the resulting stepped geometry, by allowing only one step, starting from a large cross section at the fixed end to a smaller cross section at the free end, as shown in Figure 4.3(a).

Collective results of the initial numerical search for the most effective geometry are presented in Figure 4.5. In this figure, columns indicate, from left to right, increasing the total length (L_g+L) from 100 mm to 250 mm. Each of the four rows has a different diameter of the fixed end, d_g, ranging from 30mm to 15 mm, in descending order. For all frames, the diameter of the free end is maintained at 6mm. Hence, the top row represents a step diameter change, d_g/d, of 5. This change becomes less severe for each row, finally becoming 2.5 at the bottom row.

For each frame in Figure 4.5, the horizontal axis indicates the length ratio, L_g/L, between the larger fixed-end to smaller free-end. L_g/L varies from zero to four. Zero L_g/L corresponds to the full length consisting of the smaller free end, whereas a ratio of four corresponds to $4/5^{th}$ of the length corresponding to the larger fixed end. A schematic representation is presented in Figure 4.6, for selective L_g/L, and for $d_g/d=5$. There are five curves in each frame, indicating the variation of the first five natural frequencies with L_g/L. The vertical axis is cut at 70 kHz, which is significantly larger than any frequency of interest.

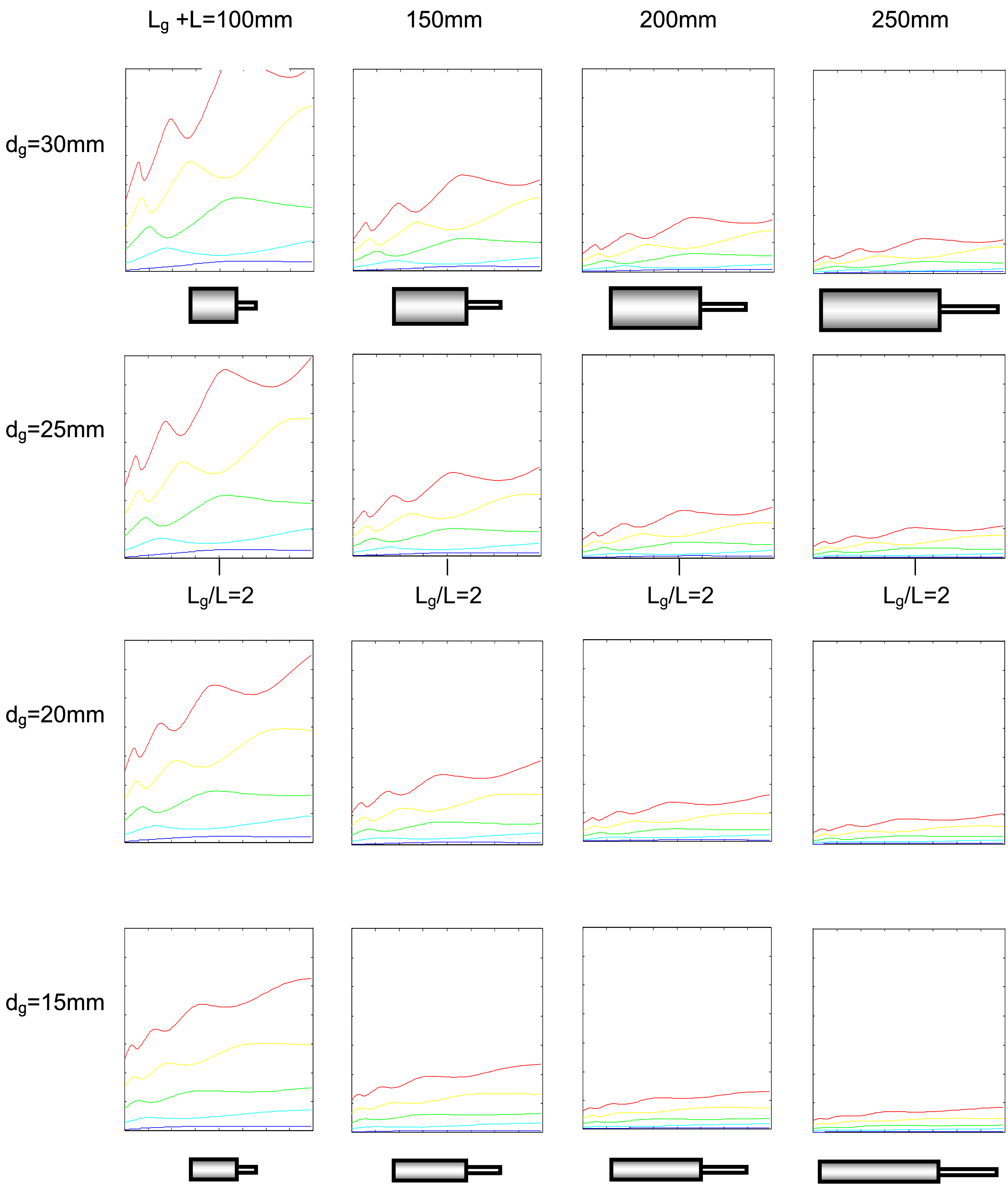

Figure 4.5. Frequency plots for fixed-free beam type 'j' with beam dimensions as shown. As in Figure 2.7, the horizontal axis is L_g/L between 0 and 4. The vertical axis is f_{n1} to f_{n5} between 0 and 70 kHz. The adaptor is aluminium, and the cutter is steel. Also shown are schematic representations of the beam geometry with $L_g/L=2$ for the first and last rows.

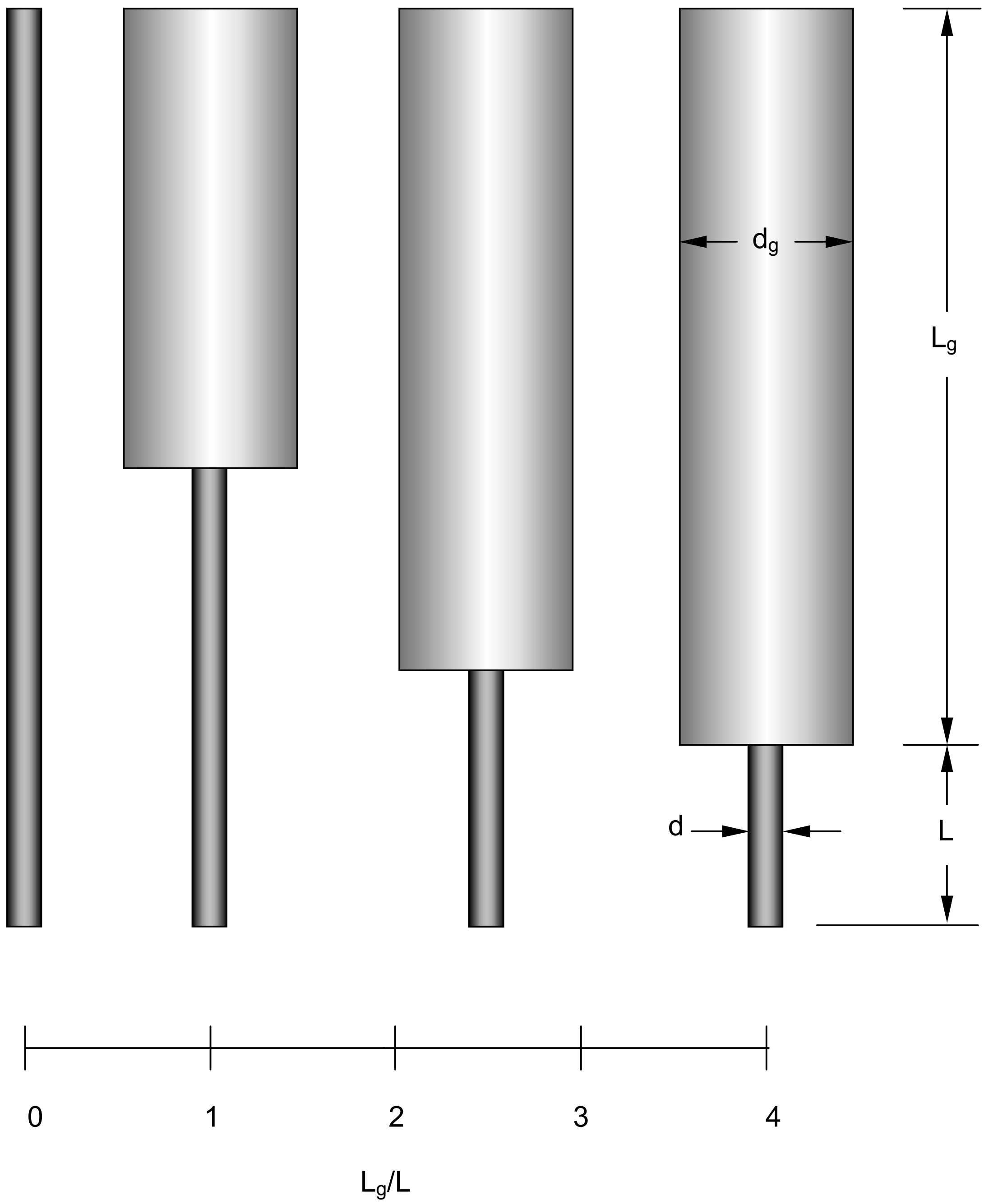

Figure 4.6. Schematic representation of four selective L_g/L geometries for d_g/d of 5.

For each row in Figure 4.5, the natural frequencies decrease from left to right, as the total length increases. For each column, natural frequencies decrease generally as the diameter of the larger fixed end, d_g, decreases from top to bottom. No particular L_g/L can be identified in the last two rows, for d_g/d of 3.33 and 2.5, where the lowest two curves are close indicating a promising geometry as discussed earlier. However, in the top two rows, for d_g/d of 5 and 4.17, of the second and third columns (total lengths of 150 mm and 200 mm), promising geometries may be identified. Among these geometries, the case corresponding to the total length of 150 mm and d_g/d of 5 is chosen for further analysis, due to having higher natural frequencies than those of the other promising cases. This case (row 1, column 2 in Figure 4.5) is repeated in Figure 4.7(a).

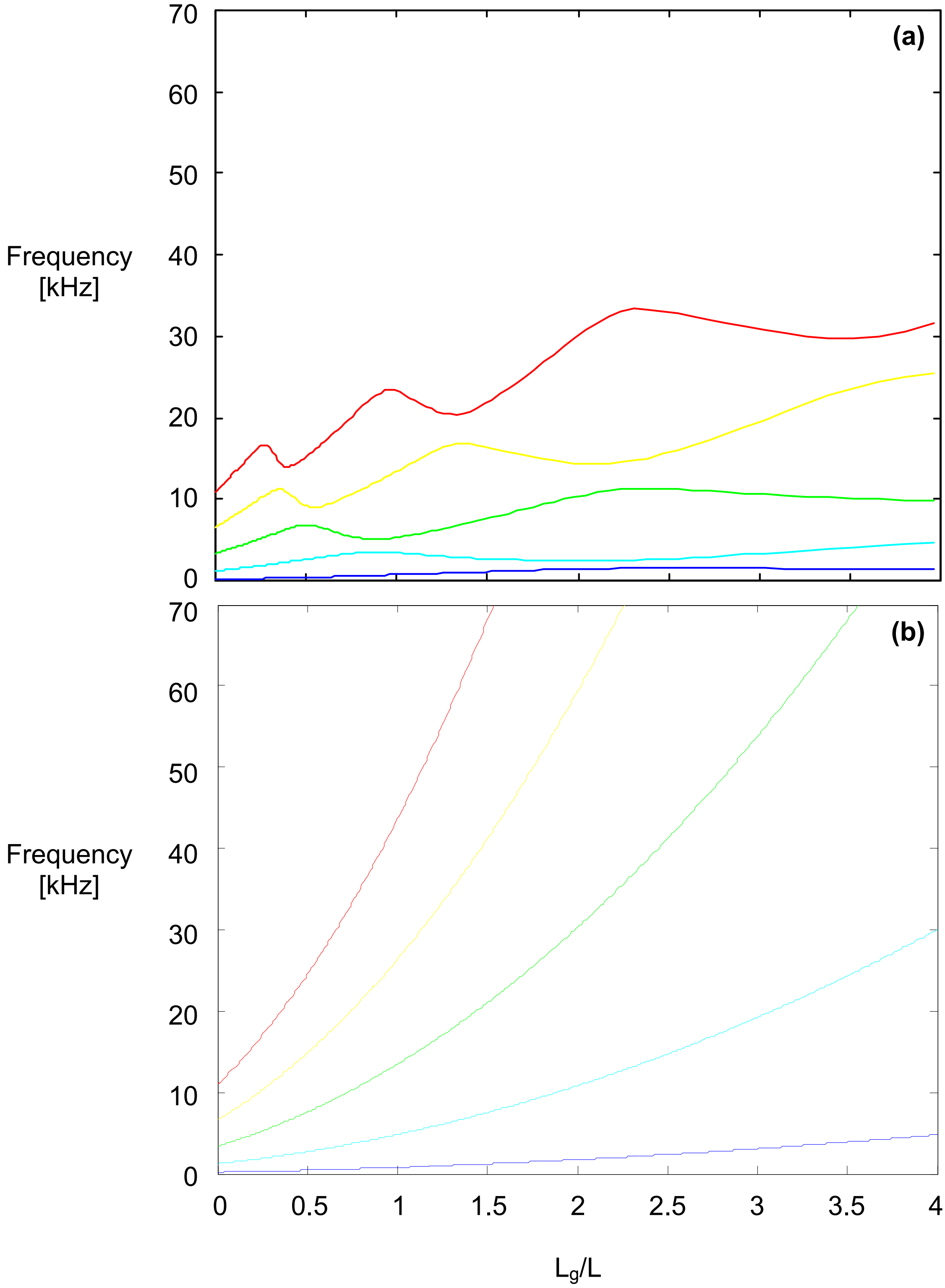

Figure 4.7. Variation of first five natural frequencies with L_g/L for **(a)** the 6 mm diameter steel milling tool with a 30 mm diameter aluminium adaptor, and for **(b)** the milling tool alone for $L_g+L=150$ mm.

An inspection of the trends of the natural frequencies in Figure 4.7(a), indicates that L_g/L values of approximately 1.8 to 3 produce the first two natural frequencies relatively close together, and the third one pushed far away from the second one. The first condition is necessary, to obtain a restraining effect from the second mode on the first mode. The second condition is desirable, to avoid the third mode keeping the second mode from its restraining effect (due to the anti-node of the third mode, corresponding to the node of the second mode).

The first five natural frequencies of the cutter alone are shown in Figure 4.7(b) for comparison with those in Figure 4.7(a). The natural frequencies in Figure 4.7(b) correspond to the fixed-free geometry of length L, and diameter d. As expected, the natural frequencies increase for increasing L_g/L, as the cutter length L becomes shorter. All the natural frequencies, and most importantly the fundamental frequency, are very well separated from each other.

The first two mode shapes corresponding to L_g/L of 2.25 and d_g/d of 5, are given in Figures 4.8(a) and 4.8(b), of the cutter alone, and in 4.8(c) and 4.8(d), of the stepped geometry. The first two frames correspond to the standard cases of a uniform sectioned beam, whereas the last two frames are those of the stepped geometry, showing the contribution of the long larger diameter adaptor. Of interest here, is that the tip displacement of the combined system appears to be greater, for both modes, than the cutter alone. It must be stressed that the amplitudes of each mode are somewhat arbitrary, since the eigenvectors are not uniformly scaled. This result may suggest that adding the adaptor would be detrimental. However, when the combined system mode shapes are forced to coexist, a retardation effect is obtained, and the tip displacement is reduced. This effect is demonstrated numerically and experimentally in the next two sections.

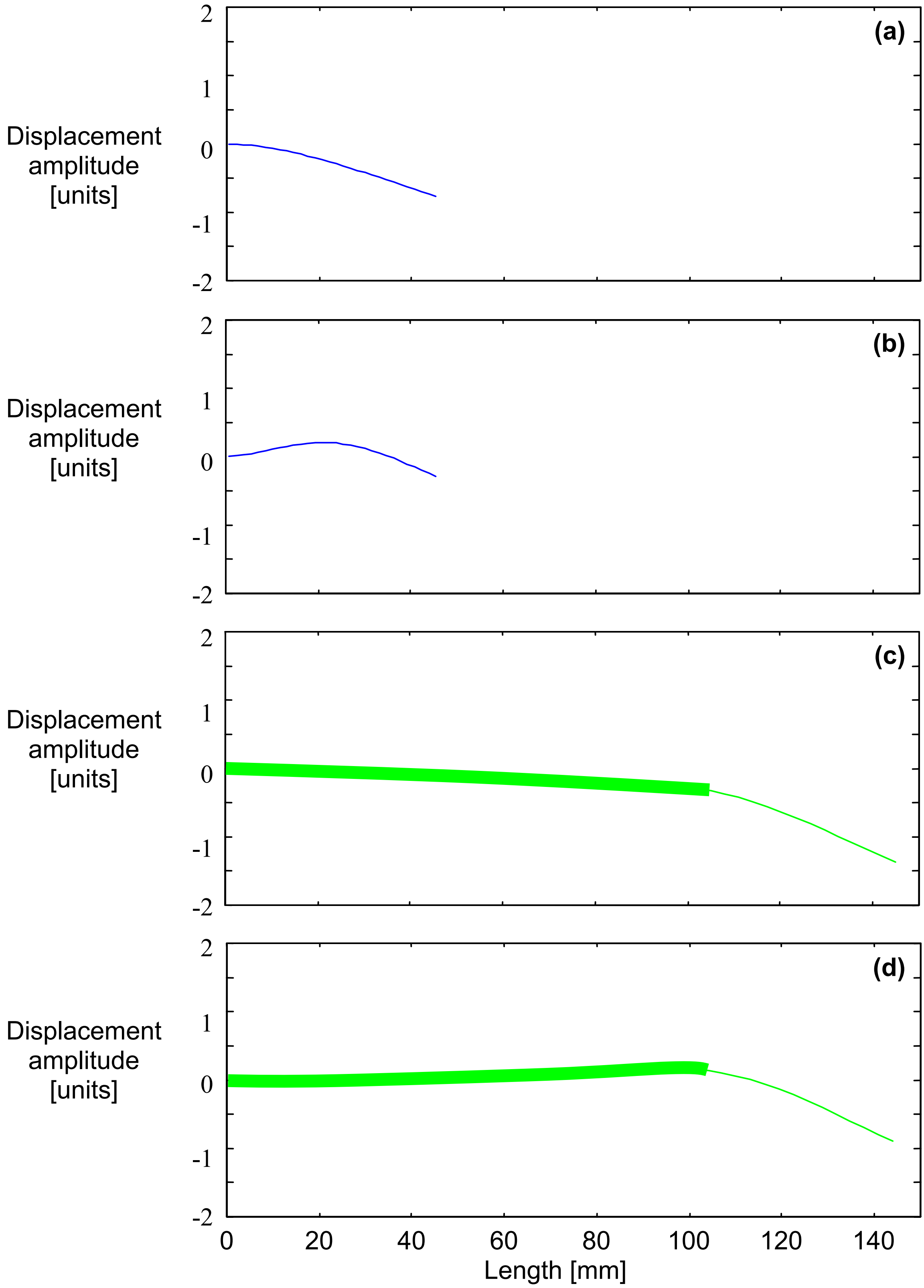

Figure 4.8. **(a)** and **(b)** first and second mode shapes of the cutter alone, respectively. **(c)** and **(d)** first and second mode shapes of the combined system of the adaptor and cutter, as indicated.

The next step involves the numerical prediction of the effectiveness of the suggested adaptor, for the particular geometries chosen from Figure 4.7(a), as compared to the case of the cutter alone. The results shown in Figure 4.9 correspond to a random white noise tip excitation to induce a dynamic response. It should be emphasized that this excitation is only indicative of cutting forces. No feedback is implemented at this stage, since the objective is to establish the control effect of the suggested geometry.

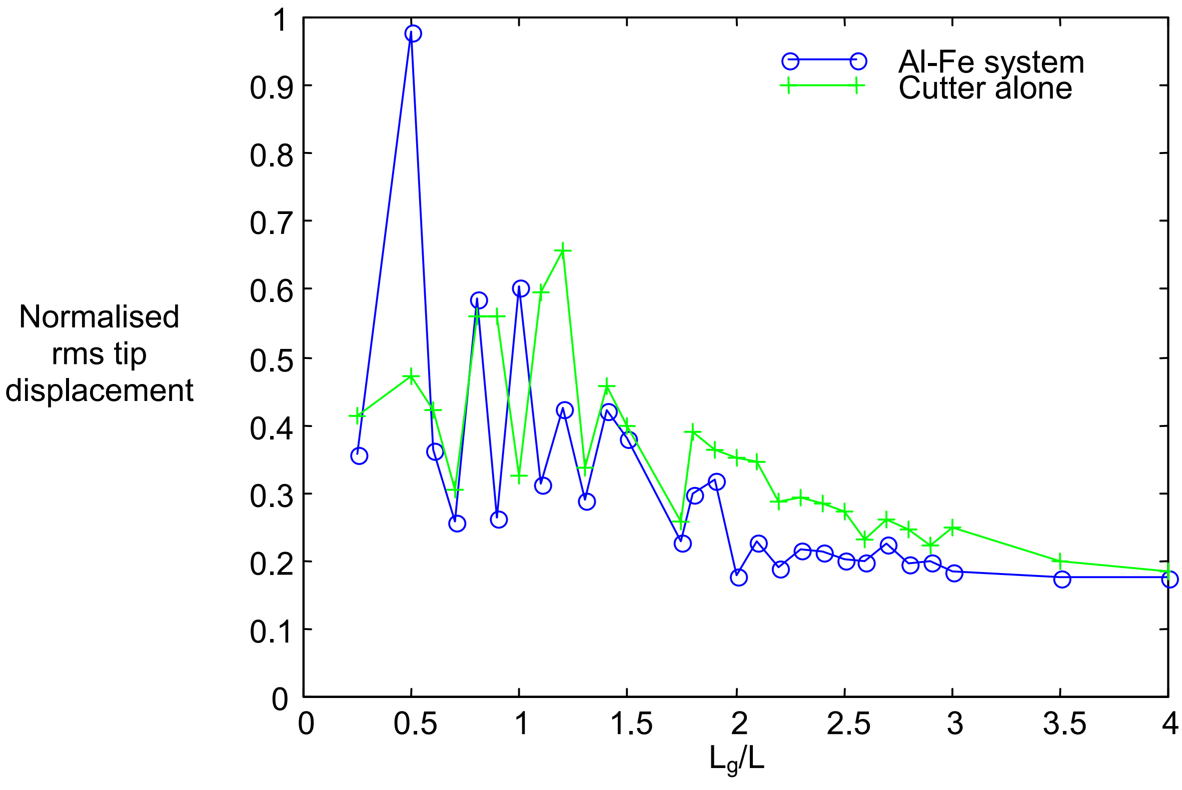

Figure 4.9. The rms tip displacement of the combined adaptor-cutter system (blue 'o') and the cutter alone (green '+').

The rms tip displacement of the cutter alone (green '+') and the cutter attached to the adaptor ('blue 'o') are shown in Figure 4.9, for varying L_g/L. The vertical axis is normalized to indicate the largest rms displacement to be unity. For L_g/L less than 2, no clear distinction is present between the response of the cutter alone and that of the adaptor-cutter system. In addition, both responses display severe fluctuations. As the structural dynamics become more favourable, for larger L_g/L, the fluctuations become smaller for both geometries. For L_g/L of about 2, the cutter with adaptor has 40% to 50% smaller response as compared to the case of cutter alone. This difference diminishes for larger L_g/L, as expected, since a short cutter also produces a small dynamic response.

Tip displacement histories are given in Figures 4.10 and 4.11 for selective L_g/L in response to the random tip excitation for the cutter alone and for the stepped geometry, respectively. As suggested from the rms plots earlier, the stepped geometries around L_g/L of 2.25 produce the most effective suppression over the case where the cutter alone is excited.

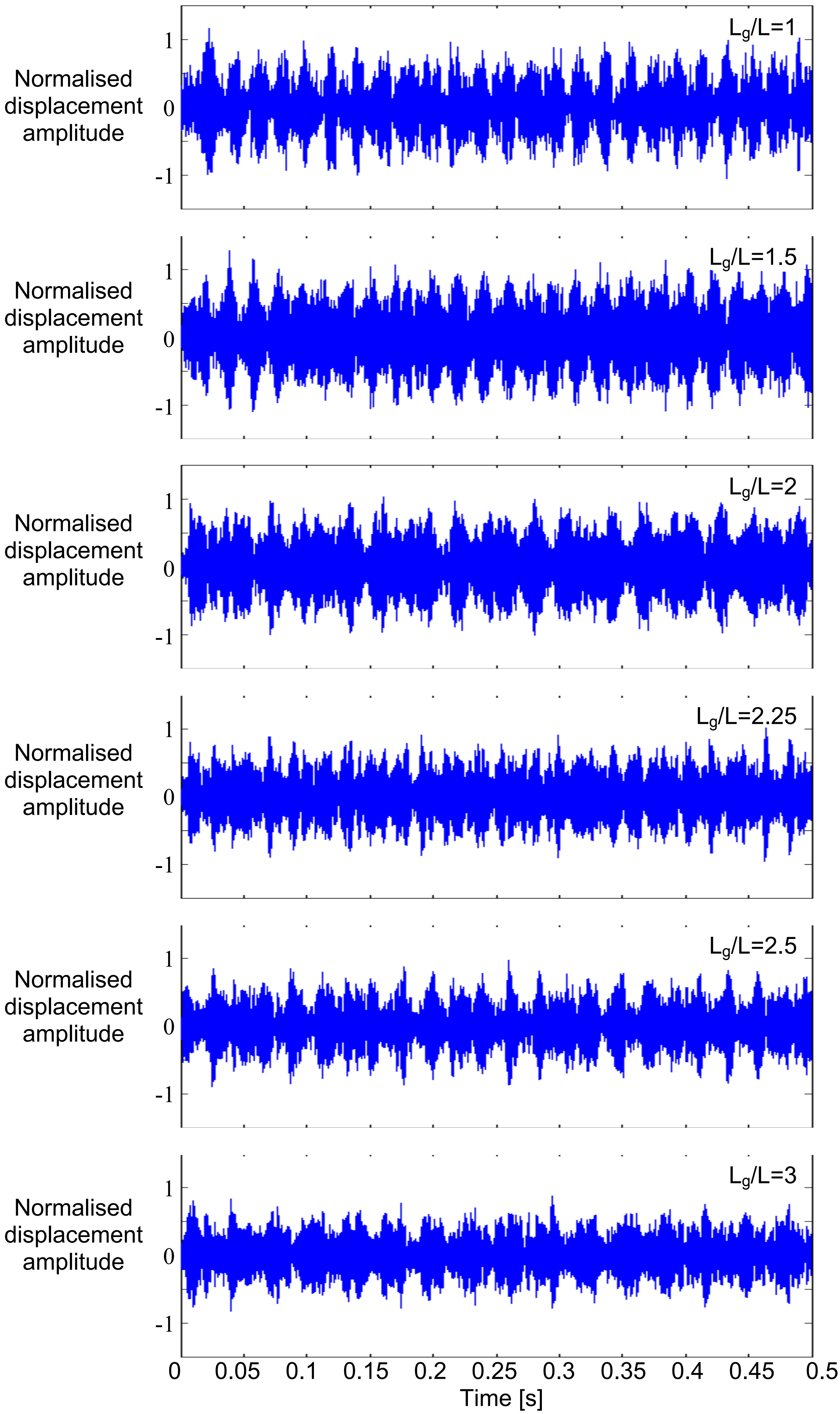

Figure 4.10. Tip displacement histories for the cutter alone corresponding to L_g/L values as indicated.

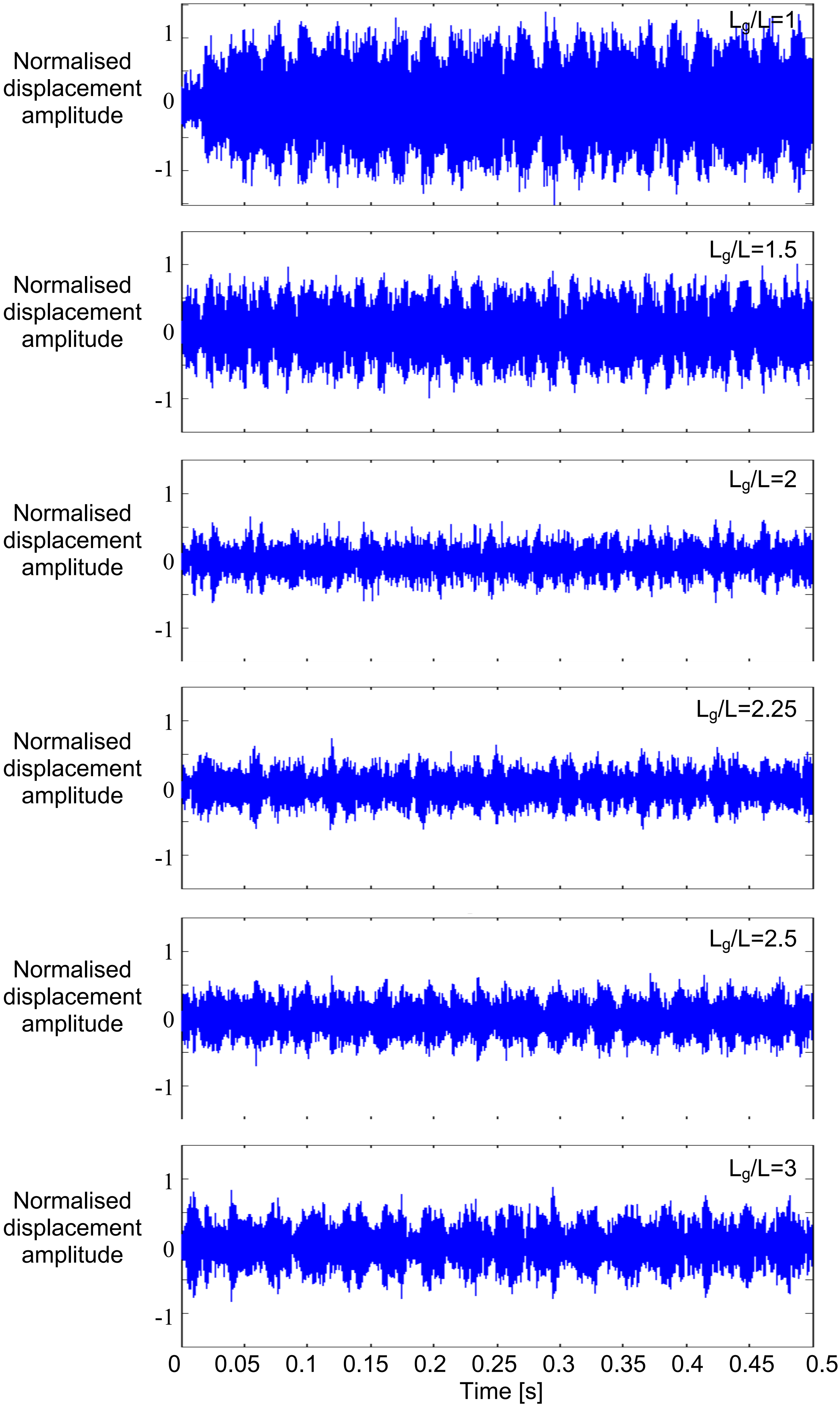

Figure 4.11. Same as in Figure 4.10 but for the adaptor-cutter system.

The suggested control is further examined next with a sinusoidal excitation, which swept frequencies from 0 to 10 kHz in 0.5s. The upper limit of the frequency is assigned rather arbitrarily, as a value large enough to cover the frequencies of interest. Displacement histories of the tip are given for selective L_g/L in Figures 4.12 and 4.13, for the cutter alone and the adaptor-cutter system, respectively.

In Figures 4.12(a) and 4.13(a), the case for L_g/L of 1 is given where both geometries result in a comparable peak displacement for the fundamental resonance. 10kHz covers only the first two natural frequencies for the cutter, whereas three resonances are encountered for the case with the adaptor, as indicated earlier in Figures 4.7(a) and 4.7(b). The same comments are true in Figures 4.12(b) and 4.13(b) with the stepped geometry showing a marginal attenuation. For L_g/L of 2 in Figures 4.12(c) and 4.13(c), the stepped geometry responds with an approximately 30% smaller peak amplitude than the cutter alone. For L_g/L of 2.25 in Figures 4.12(d) and 4.13(d), the difference becomes 45%. For L_g/L of 2.5 and 3, the difference is 30% and 15%, respectively, in Figures 4.12 and 4.13 (e) to (f). Hence, length ratios around 2.25 are now established to be promising to provide peak displacement attenuations.

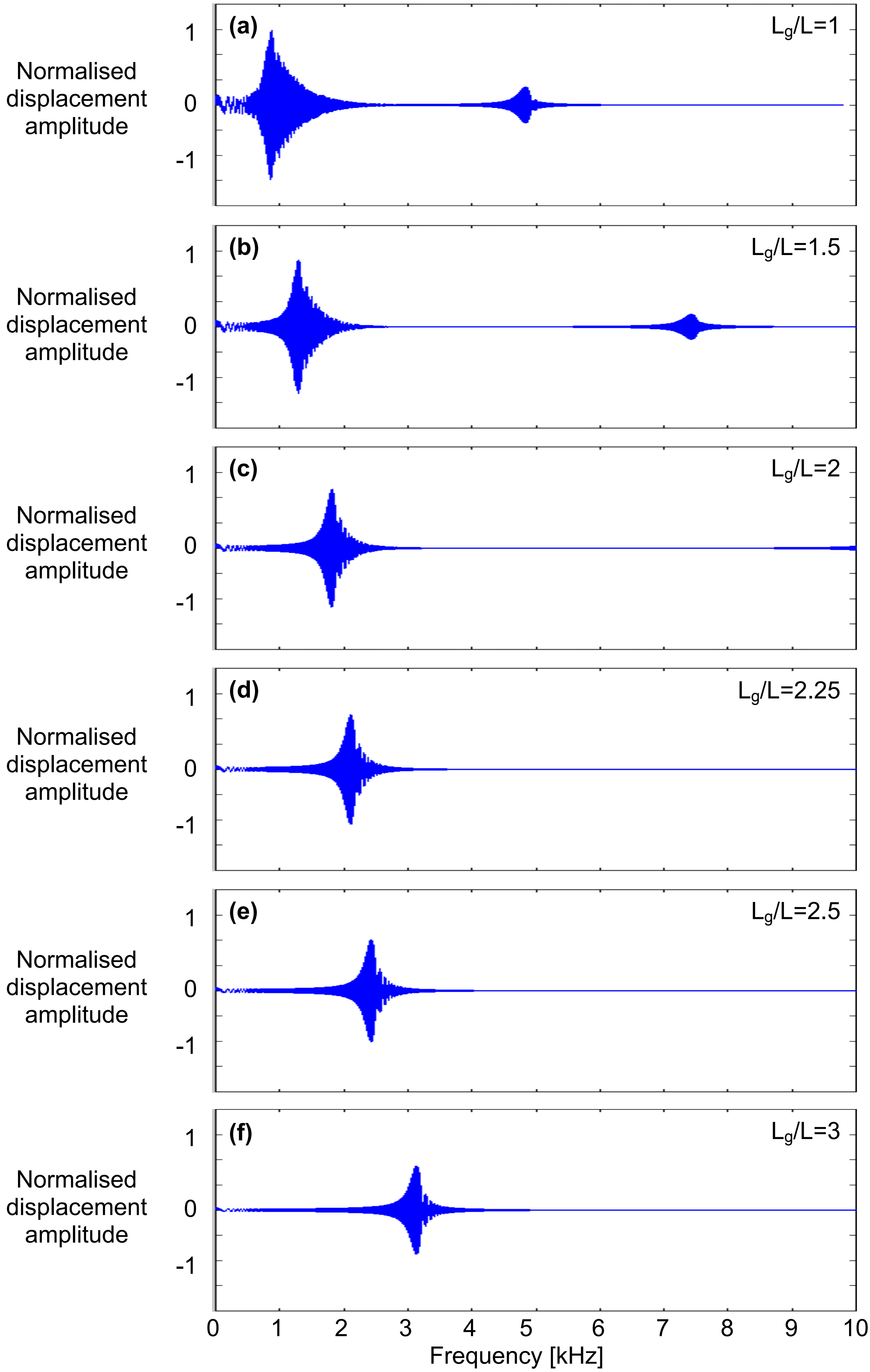

Figure 4.12. Frequency response to a ramped sinusoidal excitation for the cutter alone corresponding to L_g/L values as shown.

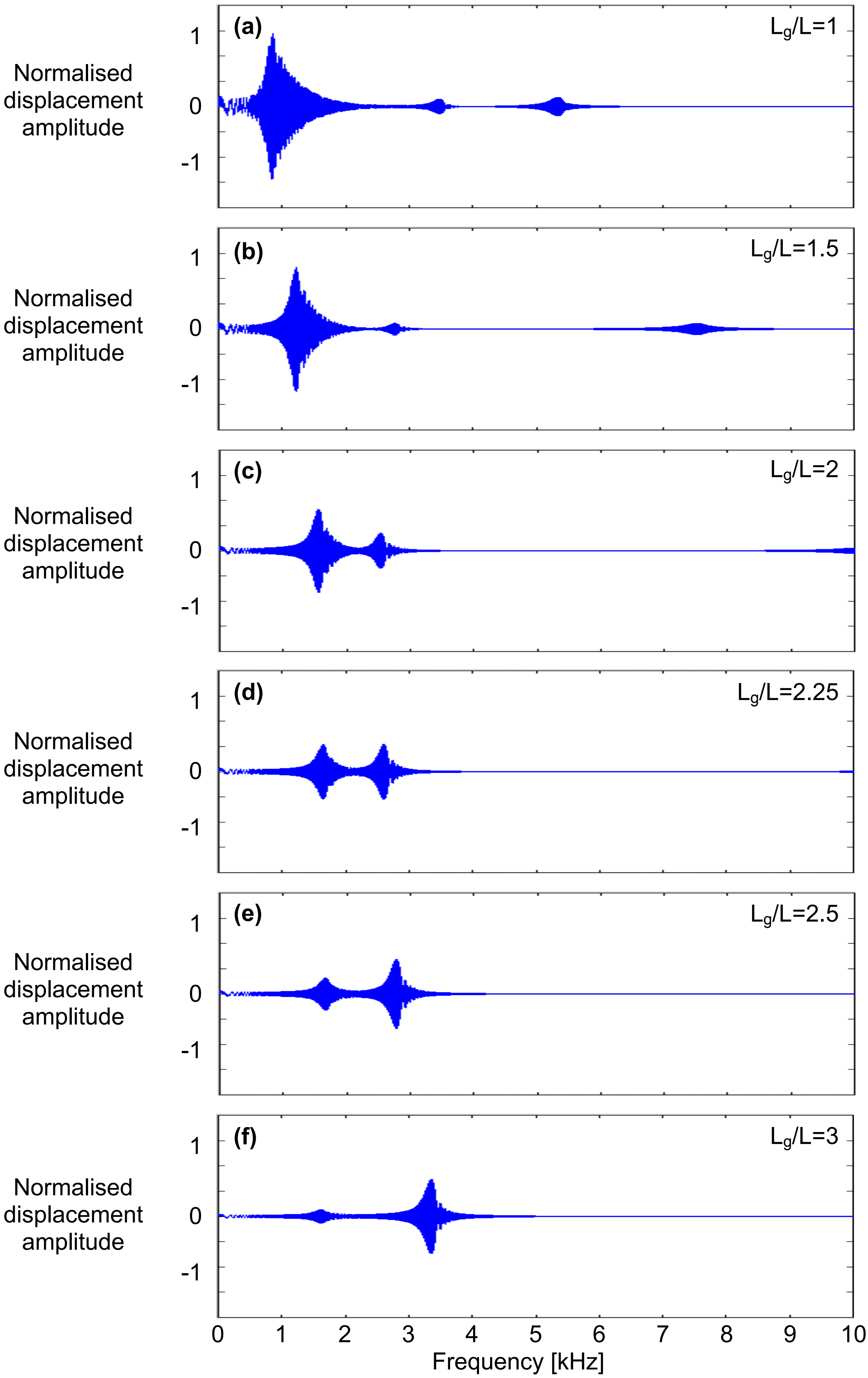

Figure 4.13. Same as in Figure 4.12 but for the adaptor-cutter system.

4. 5 Experimental Results

A simple experimental model has been prepared as a replica of the numerical model discussed in the preceding sections. A photograph of the experimental model is shown in Figure 4.14. Random excitation was provided by a generator (item 1), amplified (item 2) and fed to the electromagnetic shaker (3). Displacement output of the shaker was converted to a random force by including a soft spring (4) between the shaker and the structure. The tip response of the structure was sensed with an accelerometer (5), amplified (6) and stored digitally for further processing (7).

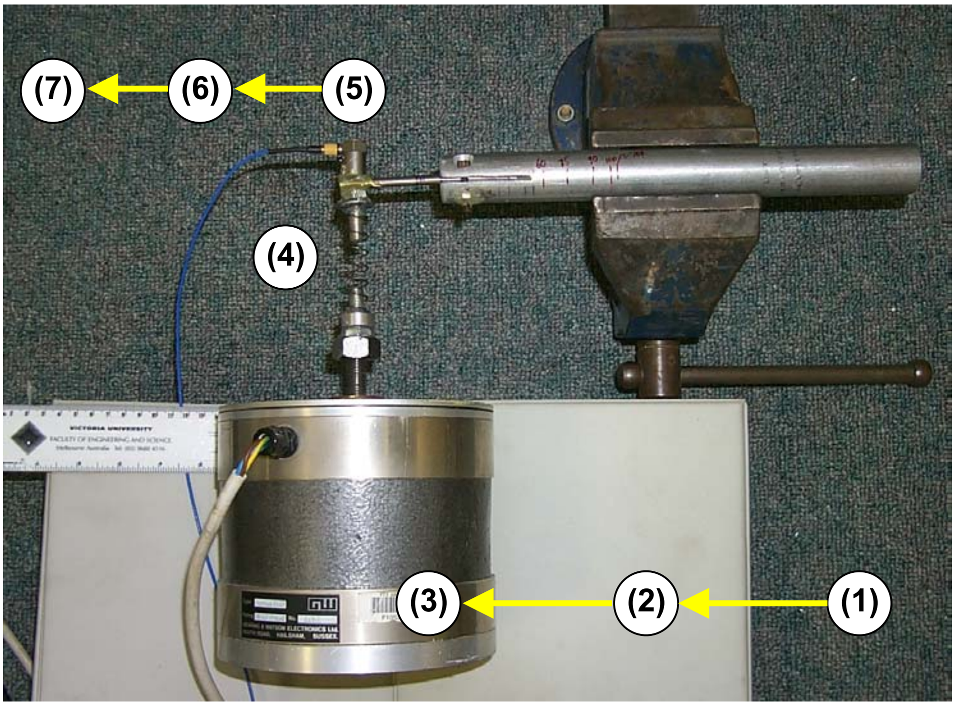

Figure 4.14. Top view of the experimental equipment itemised as follows:

1 Brüel & Kjær Dual Channel Signal Analyser Type 2032 (not shown)
2 Gearing & Watson Electronics Ltd SS100 Amplifier (not shown)
3 Gearing & Watson Electronics Ltd Shaker
Type GWV46(1Ω), Rating 38lbf (170N) No. 2132
4 Soft Spring
5 Brüel & Kjær Type 4383V Accelerometer with Noise & Vibration Measurement Systems CA11 Charge Amplifier
6 DT31 EZDATA Panel ATD board. (not shown)
Sampling Frequency 16384 Hz, 81920 Points, for 5 seconds.
7 PC using HP Vee version 4.01(not shown)

In Figure 4.14, the cutter is shown as mounted in its adaptor and the adaptor clamped on a machine vice. Length ratio L_g/L, for the 150 mm total length, was adjusted by mounting the cutter at different overhang lengths and by adjusting the clamped length of the adaptor in the vice. Although numerical predictions were all based on the displacement of the cutter tip, measuring acceleration was found be more practical due to the relatively high frequencies involved.

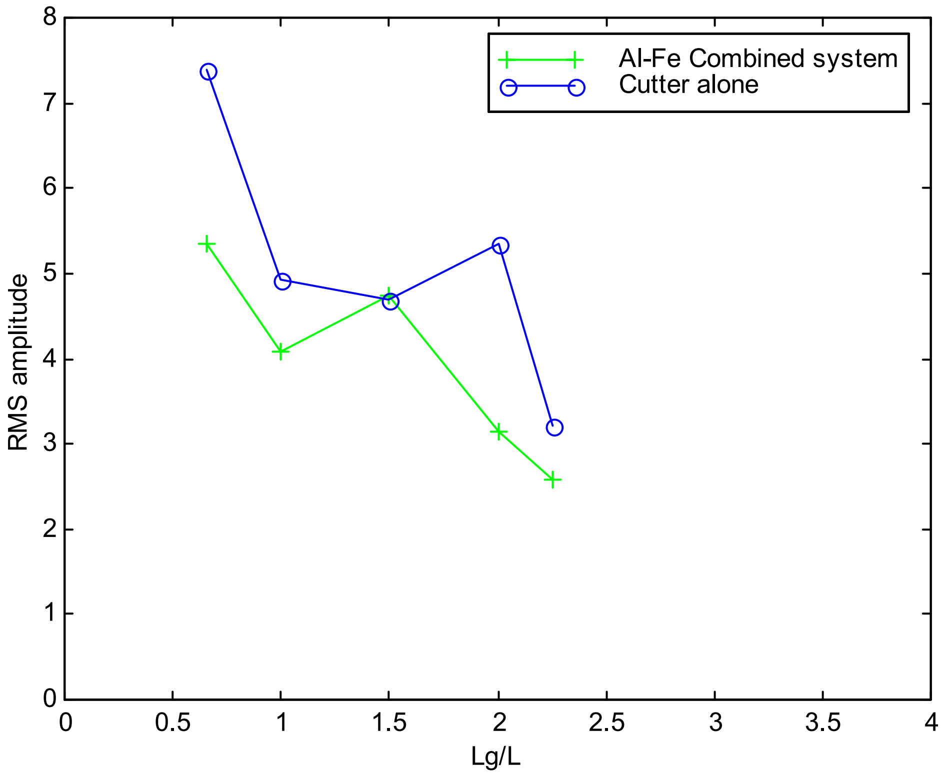

Figure 4.15. Variation of the rms acceleration with the length ratio, L_g/L.

Variation of the rms acceleration of the cutter tip is shown in Figure 4.15 for different length ratios. Tip accelerations are shown for both the 6-mm cutter alone (+) and with the 30-mm adaptor (o) by maintaining the total length ($L+L_g$) of 150mm. The most significant improvement over the existing geometry is observed at a length ratio of 2 where the inclusion of the adaptor enables an approximately 45% attenuation of the tip acceleration.

The acceleration history of the cutter, where its 50 mm total length alone is clamped from the vice, and its power spectrum are shown in Figures 4.16(a) and 4.16(b), respectively. This 50 mm length corresponds to L_g/L of 2. The Power spectrum is obtained in order to calculate the mean square acceleration after taking the fast Fourier transformation (fft) of the time series. In Figure 4.17, the same information is presented for the case with the inclusion of the 100 mm long adaptor. As indicated in Figure 4.15, the levels of acceleration with the adaptor are about half of those when the cutter alone is excited. In addition, the fundamental frequency of the cutter is suggested to be almost the sole contributor to the accelerations in Figure 4.16(b), since the second resonance peak can be seen just above 0.5kHz. In Figure 4.17(b), however, the spectral peak is made up of two resonances in such close proximity that they cannot be separately identified. Spectral peaks of these two modes can reach only a fraction of the amplitude of the case when the cutter is alone.

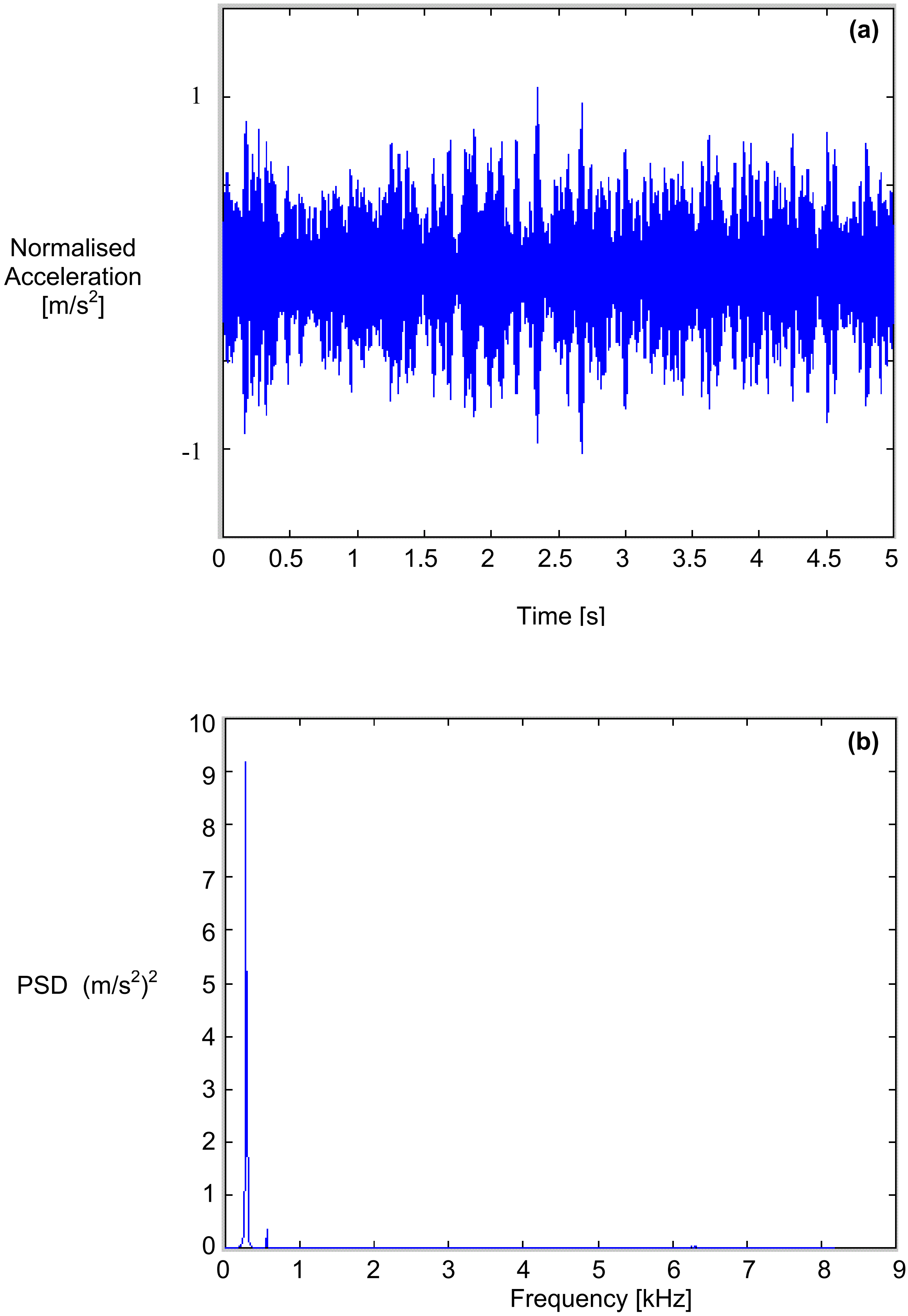

Figure 4.16. Acceleration **(a)** history and **(b)** power spectrum of the 6mm diameter cutter of 50 mm length (for L_g/L = 2).

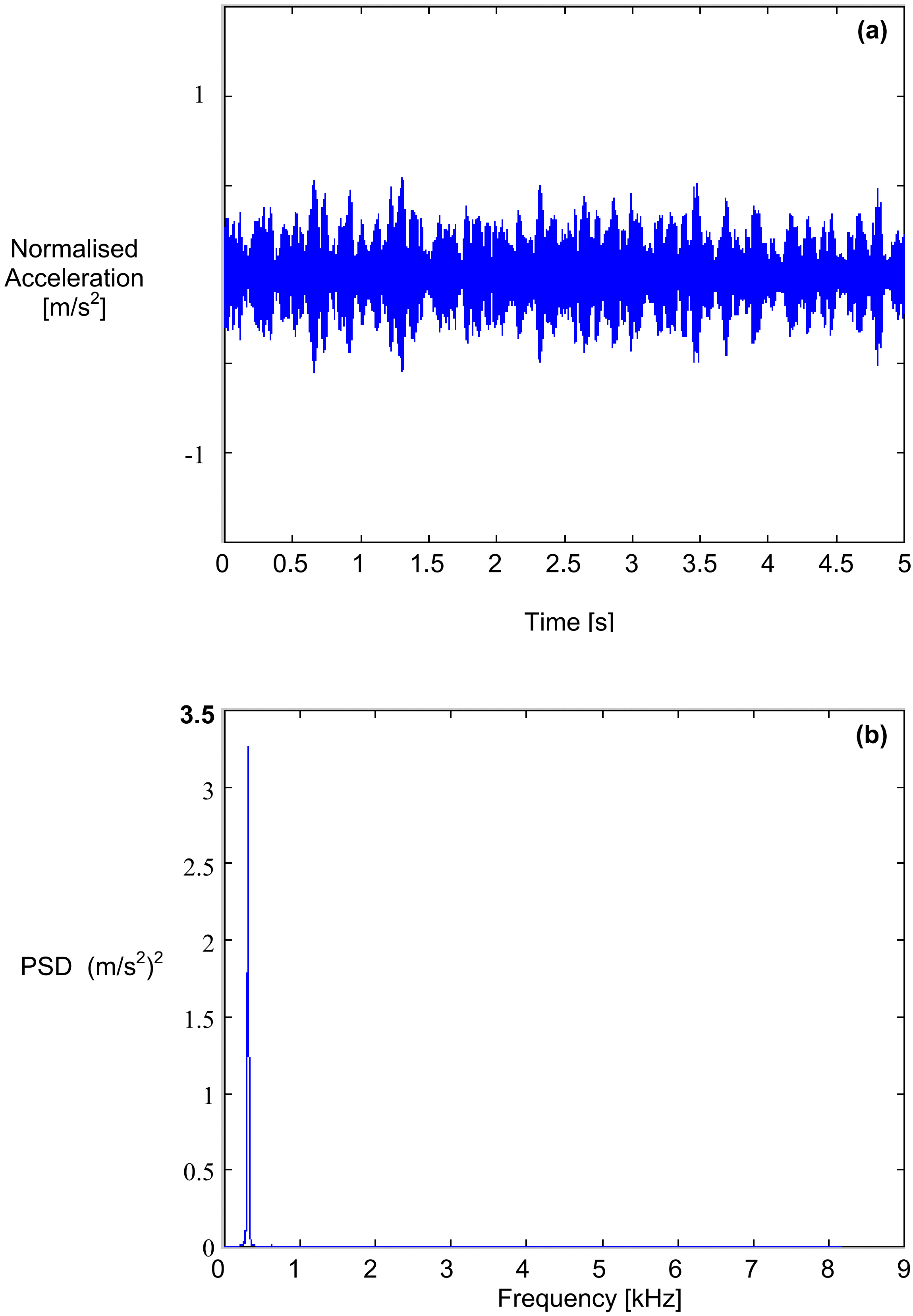

Figure 4.17. Same conditions as in Figure 4.16 but with the 30mm diameter adaptor.

4. 4 Conclusions

Results are presented in this chapter to include numerical predictions, using standard finite elements approximation, and experimental observations to check the validity of the predictions. It appears that by making a simple geometric change, such as including a stepped adapter, it may be possible to obtain a resulting structure with its first two natural modes virtually coincident. The benefit of such coincidence is to take advantage of the suppression effect of the contribution of the second mode on that of the first mode. Such suppression effect may result in a cantilevered cutter, which is significantly less prone to chatter instability. The next stage of this work is cutting tests to verify such a premise.

Chapter 5

TRANSVERSE ARROW VIBRATION

5.1 Introduction

As discussed in the previous chapters, the control technique developed in this thesis is applicable to problems where the first mode is prevalent. The problem discussed in this chapter is transverse arrow oscillation. Presented results are limited to a preliminary numerical investigation.

The bow, as shown in Figure 5.1(a), consists of two ‘limbs’, a ‘handle’ and a ‘string’. The limbs provide the spring energy (potential energy) of the bow to the arrow via the string. The arrow rests between the bow handle and the string. Figure 5.1(b) and Figure 5.1(c) show the bow in the ‘strung’ and ‘drawn’ states, respectively. The arrow, as shown in Figure 5.1(d), has a ‘pile’ at the tip of the arrow, and a ‘nock’ at the trailing end. A groove in the trailing end of the nock allows it to fit onto the bowstring. Archers ‘draw’ the arrow back with their right hand, for a right handed archer, while holding the bow handle in their left hand. An archer holds the arrow at ‘full draw’ while aiming the bow, and then releases the string to fire the bow. This process is called the ‘loose’.

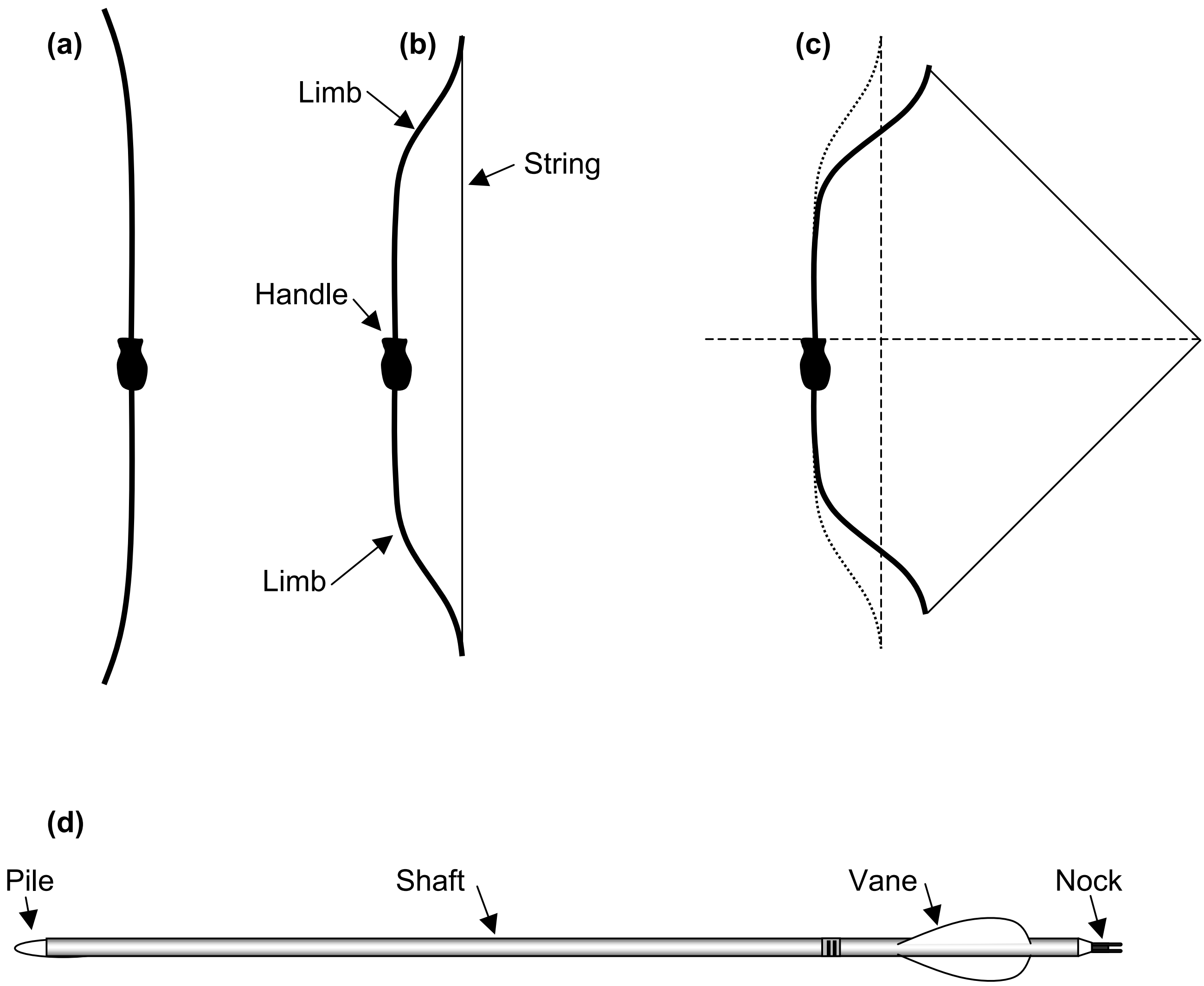

Figure 5.1. **(a)** The unstrung bow, **(b)** strung bow, **(c)** fully drawn bow, and **(d)** arrow.

Following the release, the nock end of the arrow initially bends away from the bow. Then, it moves back towards the bow and then, away again, completing 1.5 cycles of bending oscillations. The objective is to have the nock end of the arrow bending away from the bow as it passes the handle of the bow. If this objective is not realised, and if the arrow slaps the handle as it passes, the shot will be inaccurate [41]. The phenomenon of the arrow snaking around the handle of the bow is called the ‘Archer’s Paradox’ [42]. Hence, the paradox is that bending of the arrow during release is essential for the arrow to clear the bow. However, such bending will inevitably continue during the free flight to cause deviations from the target.

Earlier work by Kooi and Sparenberg [42] discussed two causes for the transverse bending of the arrow. The first cause relates to the style of the Mediterranean release, which involves the string being retained by three fingers; the index finger above the arrow and two fingers below the nock of the arrow. At the release, the string slips off the fingertips, the nock of the arrow is moved sideways swiftly (away from the bow), and the arrow bends due to its inertia. The second cause relates to having a finite width of the bow handle. At full draw, the arrow makes a small angle, in the horizontal plane, with the bow handle. The archer deliberately sets this angle to give a bias to the arrow for its first bending mode. After release, this angle increases swiftly due to the forward velocity of the arrow, once again causing the arrow to bend away from the bow due to its inertia. This bending is a result of the large longitudinal force that may also be interpreted as the buckling of the arrow, which is a slender column under compression.

Reference [41] states that if the pile of the arrow in free flight moves from side to side significantly, then there is a variation of where the arrow actually hits the target. This is clearly seen from the first bending mode shape of a free-

free beam, shown in Figure 5.2. If the arrow happens to make contact with the target as it assumes the largest deflection, the deviation of the tip from the mean arrow position will be the largest. The mean arrow position may be considered to be the average path during flight.

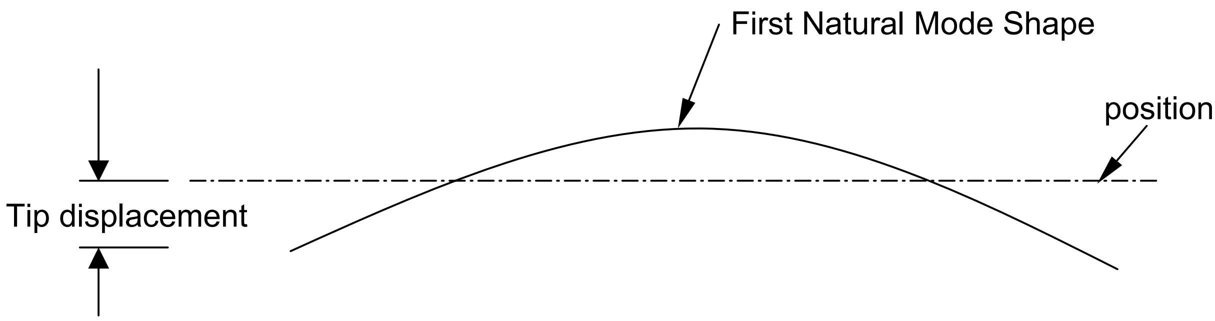

Figure 5.2. First mode shape, corresponding to the first natural frequency, of an arrow.

Ideally, archers want to have everything consistent so that any deviation from one shot to the next is due to the archers themselves. If the equipment has its own deviation, then the final 'grouping' is a compounded result of both deviations. The term 'grouping' refers to the area covered by a series of consecutive shots. A small grouping means that all the arrows hit the target close to one another, and hence, the archer is consistent. Naturally, a large grouping means that the archer has no consistency.

On the archery field, one can easily detect the presence of arrow vibration at the point of target impact by noting the deviation in the entry angles of different arrows. Supposedly, the arrows in a purchased set of 12 will have an extremely tight weight tolerance (weight sorted to ± 0.5 grains). The units of 'grain' is thought to have originated from the weight of an average grain of wheat, equivalent to 1/7000th of a pound (0.0648 grams). Therefore, according to the manufacturer's claims, the archer can expect each arrow to behave similarly. Unfortunately, this is not the case. Olympic grade archers learn the characteristics of each arrow and compensate their aim accordingly.

The length of an arrow is dependent on the draw length of the bow being used. The draw length of a bow must fit the archer's arm length so that a comfortable arm position is reached at full draw. The bow considered for this analysis has an adjustable draw length of 30 to 32inches, currently set at 31.5 inches. Hence, the arrow length is 31.5 inches, or 800mm.

A typical arrow currently being sold throughout the world is the 'Carbonhawk'. Its shaft is a carbon fibre tube having a nominal outside diameter of 6.18mm and a wall thickness of 0.92mm. The point mass at the pile end is 100 grains or 0.0064kg.

The approach here is to modify the Carbonhawk arrow geometry to reduce its proneness to large amplitude transverse oscillations. To this end, an add-on solution is presented, in keeping with the method discussed in Chapter 4. The next section discusses the suggested modifications. Then, a preliminary model and numerical predictions are presented.

5.2 Numerical Modelling

The geometry of the Carbonhawk arrow, outlined in the previous section, is modelled here as a homogeneous, isotropic tube of carbon fibre with a density of 1436 kg/m^3 and a Young's modulus of 102 GPa, as measured from the purchased arrow. Figure 5.3 shows the numerical model with its free-free boundary conditions.

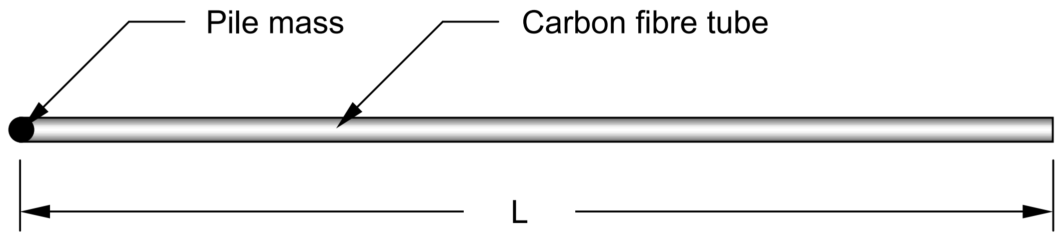

Figure 5.3. Model of the Carbonhawk arrow made from a carbon fibre tube having an outside diameter of 6.18mm and a wall thickness of 0.92mm.

The model, shown in Figure 5.3, has 30 standard beam elements distributed along its length to accurately predict its dynamics in the first five bending modes. The natural frequencies and mode shapes of the arrow were provided by the solution of the resulting eigenvalue problem in Matlab®[10]. The first two natural frequencies calculated are zero, due to the lack of boundary constraints, and are not included in the following discussion. Therefore, the first bending frequency corresponds to the third eigenvalue.

This investigation is concerned with the vibration characteristics of the arrow after it has cleared the bow. Rather than using a broadband excitation force, as was the case for the two previous applications, here the excitation input is a transient unit impulse applied perpendicularly to the centre of gravity (COG) of the arrow. The ensuing transient response of the arrow to this force was obtained by numerically integrating the system differential equations of motion using the Newmark-β technique [2]. Once again, 50,000 steps of integrations were performed with a time step of 1/60th of the period of the first natural bending frequency.

The starting geometry of the existing Carbonhawk arrow has well separated first, second and third natural frequencies of 100 Hz, 308 Hz and 635 Hz, respectively. As mentioned in the previous chapters, well separated natural frequencies is a problem, since the first natural frequency dominates the deflection, and consequently, the amplitude builds up to resonance. The objective here is, once again, to push the first and second natural frequencies together. If these two modes can co-exist, then the higher stiffness and the additional nodes of the second mode may suppress the contribution of the first mode. This suppression effect is suggested by the average of the first two mode shapes shown in Figure 5.4. This average mode shape is based on the assumption that the first and second mode shapes have equal contributions. As mentioned in Chapter 2, the first two modes will have slightly different natural frequencies causing travelling, rather than stationary, nodes to exist in the average mode shape.

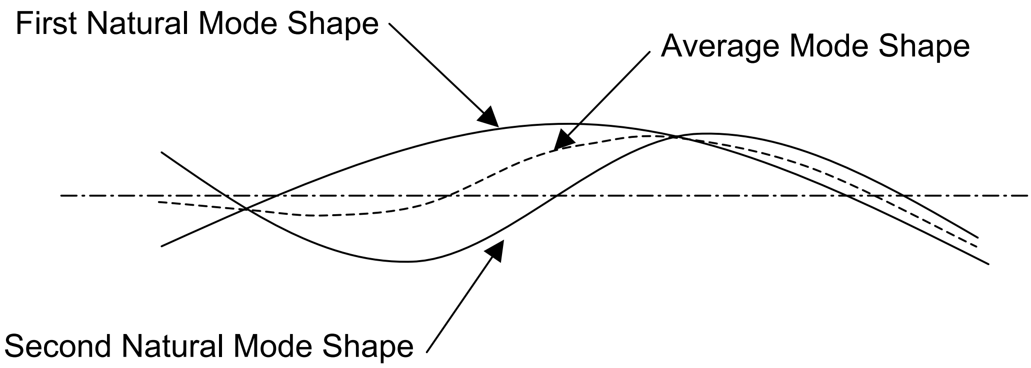

Figure 5.4. First and second mode shapes for a free-free uniform beam. The dashed line represents the average of the first two mode shapes.

5.3 Numerical Predictions

The arrow geometry is effectively a uniform, hollow cross section for the entire length. Hence, similar to the milling tool application, an additional structure must be included in order to allow manipulation of the relative proximity of the two lowest natural frequencies. As discussed in the previous chapters, the additional structure must have a significant step change in its cross sectional geometry. Hence, a practical suggestion to achieve a stepped geometry may be to attach a small, ‘needle-like’, structure to the nock of the arrow.

The length of the ‘needle’ was fixed at 60mm. This length was considered to be reasonable when compared to the 800mm length of the arrow. Hence, the manipulation of natural frequency separation was done by changing the only design parameter, the diameter of the ‘needle’. Variation of the first five natural frequencies of the suggested design is shown in Figure 5.5 as a function of the needle diameter.

In Figure 5.5, the horizontal axis ranges from a needle diameter of 0 to 5mm. For small diameters, the natural frequency separation approaches that of a uniform beam corresponding to the original arrow geometry. The point of interest in Figure 5.5 is the region where the needle diameter is between 0.4mm and 0.5mm. For comparison, a typical domestic sewing needle has a diameter of 0.5mm, whereas a typical diabetic syringe has a diameter of 0.33mm. From Figure 5.5, a needle diameter of 0.43mm yields the closest f_{n2}/f_{n1} of 1.2. The modified arrow has f_{n1} and f_{n2} of 91Hz and 112Hz, respectively, whereas the original arrow had corresponding values of 100Hz and 308Hz.

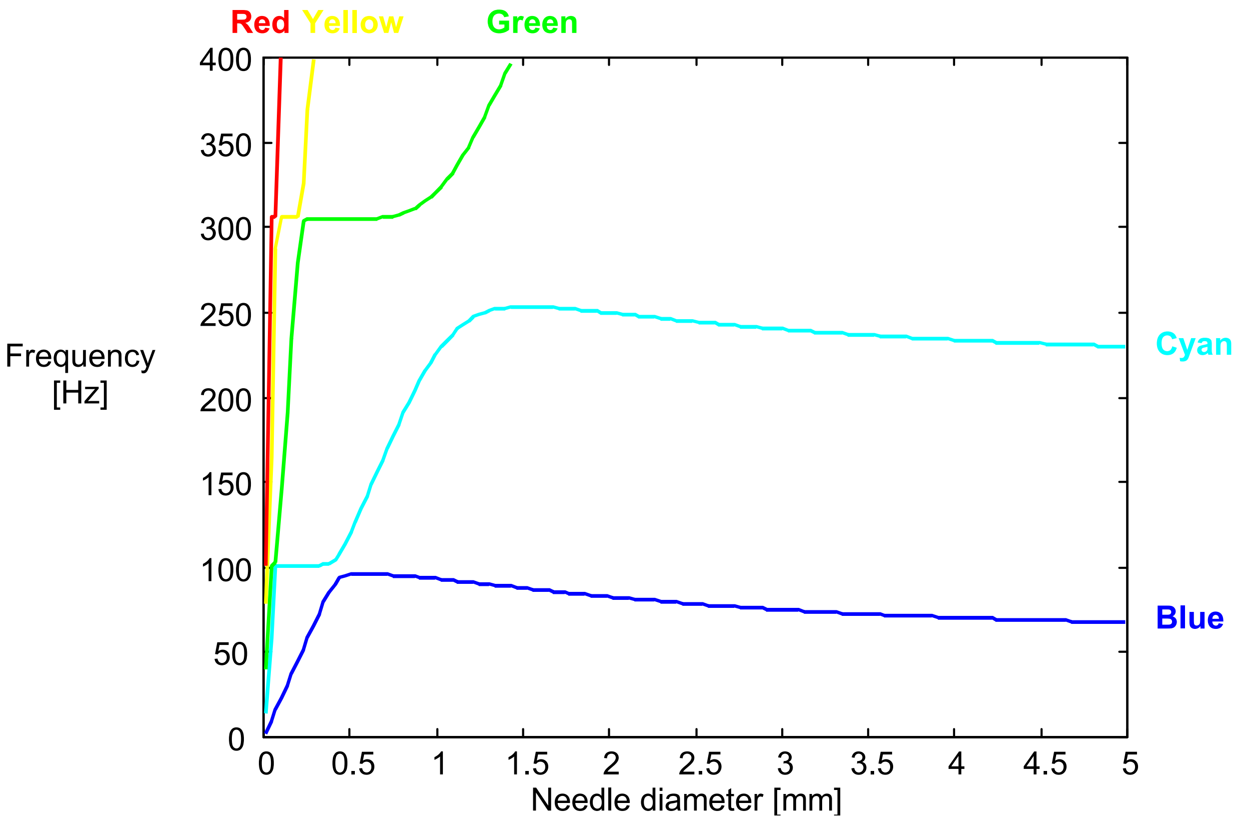

Figure 5.5. Natural frequency against needle diameter for a 800mm long Carbonhawk arrow. The blue line represents the first natural frequency (f_{n1}), cyan and green represent the second (f_{n2}) and third (f_{n3}) natural frequencies, yellow and red represent the fourth (f_{n4}) and fifth (f_{n5}) natural frequencies, respectively.

It may also be of interest here to note that the 'best' geometry suggested in Figure 5.5 corresponds to that of a tuned absorber. For the given length of 60mm, a diameter of 0.43 mm yields the same fundamental frequency as that of the arrow alone. Hence, an absorber tuned at the critical frequency of the arrow, is able to produce the largest interference with the fundamental mode of the arrow.

For a transient excitation force, an rms comparison is less relevant than it was for the previous applications. Here, the rate of decay is more relevant since the objective is to have the transverse arrow vibration settle before the arrow hits the target. Hence, observing the nodal point displacement histories of the original and the modified arrows allows clear comparisons to be made. Of primary concern is the tip, or pile, displacement history as shown in Figure 5.6. The numerical models of the original arrow, and the modified arrow have 1% structural damping, calculated according to the procedure given in Rao [2].

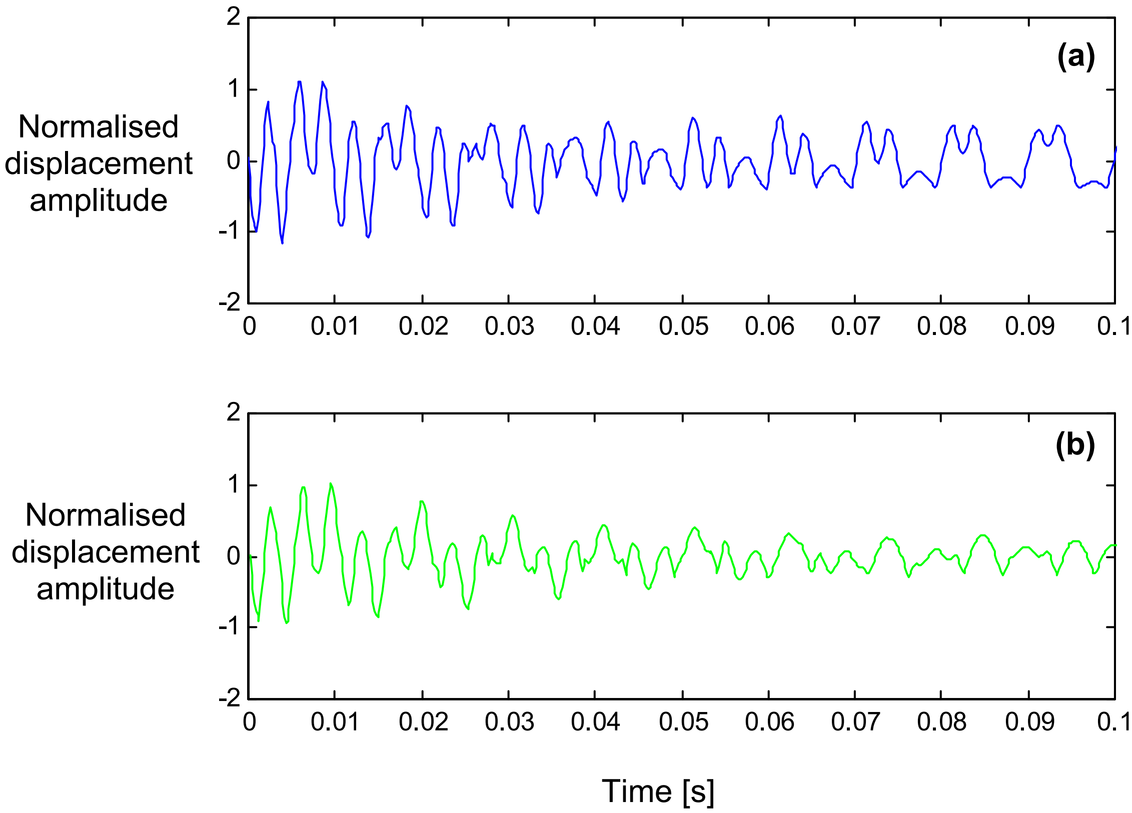

Figure 5.6. Normalised tip displacement histories for **(a)** the original arrow, and **(b)** the modified arrow.

In Figure 5.6(a), a typical decay time is shown due to light structural damping for a free-free beam, representing the original arrow configuration. The vertical axes of Figure 5.6 (a) and (b) are normalised by scaling the peak positive displacement of the original arrow geometry to unity. Figure 5.6(b) shows the tip displacement history for the modified arrow, with a clearly greater decay rate than that of the original arrow. After 0.1 seconds, the modified arrow has less than half of the tip displacement amplitude of the original arrow. For the bow and arrow set up considered here, the arrow exit velocity from the bow was measured experimentally at around 65m/s. Hence, after 0.1 seconds the arrow would have travelled 6.5m from the bow.

Of further interest from Figure 5.6 is that for the first 0.02 seconds, both arrows appear to have similar displacement histories. This is an unexpected bonus, since this similarity suggests that adding a needle to an arrow will not interfere with the Archer's Paradox discussed earlier. Therefore, an archer who has 'tuned' his/her bow and arrow equipment to give good arrow clearance will not have to retune the equipment after applying the needle to the arrow nock. Also of interest is the displacement amplitude of the arrow 's centre of gravity (COG) shown in Figure 5.7. The vertical and horizontal axes in Figure 5.7 are the same as in Figure 5.6.

The COG displacement histories for the original and modified arrows are similar in amplitude. This similarity is mostly due to the fact that the COG is close to a node of the second bending mode, masking the interference of the second mode for the modified arrow. Furthermore, the average mode shape shown in Figure 5.4 has comparable amplitude to the first mode shape around the mid-point of the arrow, where the COG is located. Therefore, the COG displacement amplitude of the modified arrow is expected to be comparable to the original amplitude. The modified arrow makes one less period in the time interval shown, since it has a slightly lower fundamental frequency than the original arrow.

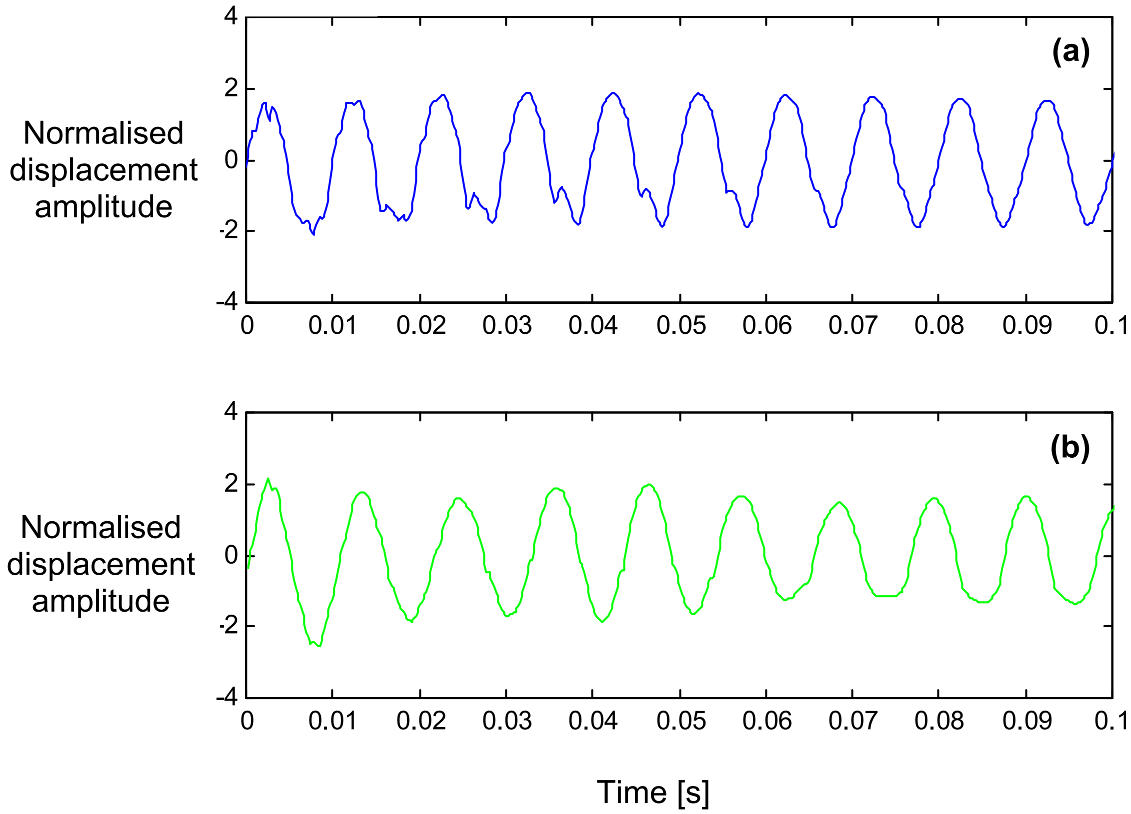

Figure 5.7. Normalised COG displacement histories for **(a)** the original arrow, and **(b)** the modified arrow.

5.4 Conclusions

The suggested modification to the arrow here is that an after-market nock be made with a needle attachment. The practical solution would be to set a fixed diameter for the needle, then trim the length of the needle to get the correct tuning for each length of the arrow.

The numerical predictions suggest that a needle applied to the nock of the arrow may significantly reduce the tip displacement of the arrow. It must be stressed that these numerical predictions need to be followed up with experimental verification.

Numerical simulations presented here assumed a 1% equivalent viscous damping to represent structural damping of the material. Any material chosen for the suggested needle with a higher capacity of energy dissipation would certainly improve the control effect. An optimum value for a tuned absorber is suggested to be approximately 20% in Snowden [43] for most effective control in transient motion.

Chapter 6

CONCLUSIONS

This thesis is focused on reducing the undesirable transverse oscillations of slender beam like structures using a novel technique of imposing two coincident natural frequencies. At the commencement of this thesis, no published results existed to control vibration in beams by imposing two coincident frequencies.

In this chapter, the conclusions and novel findings of each chapter of the thesis are summarised. The novel vibration control technique developed in this thesis is introduced in Chapter 1. This technique involves imposing multiple coincident natural frequencies to reduce the vibration amplitude of slender beams. The technique is applied here to three problems, namely, hot-wire probes, milling tool chatter and archery. The first of these problems, hot-wire probe sensing wire vibration, has had no previous attempts made at reducing its undesirable oscillations.

In Chapter 2, the control technique is described in detail. The technique requires the first two natural frequencies being forced together, while the third natural frequency is pushed as far away as possible. When this condition is achieved, the beam can not clearly exhibit either mode. Neither mode is able to build to resonance, since the beam attempts to have both modes coexist. Hence, the overall vibration amplitude is reduced.

There are many advantages of this technique over existing forms of vibration control. The technique can be applied to displacement sensitive problems, such as the three under investigation here, where space or boundary constraints disallow the traditional forms of vibration control. Furthermore, this technique does not involve a secondary control system, such as those in actively controlled machines, vibration absorbers and dampers.

The relative distribution of the natural frequencies of a slender beam can be modified if the beam has a significant cross sectional step change. Then, by manipulating the relative length of each of these sections, the first and second natural frequencies can be pushed together, while the third is pushed away. The trends of this manipulation are discussed, along with methods to scale the results to make the numerical analysis more efficient.

In Chapter 3, the control technique is applied to the first problem of the sensing wire vibration of hot-wire probes. The sensing wire of a hot-wire probe is susceptible to large amplitude transverse oscillations in turbulent flow conditions. Previous research suggested that these vibrations may lead to measurement inaccuracies. Flow measurements conducted in this thesis clearly show the measurement anomalies of vibrating wires. New wire geometries were manufactured after numerical modelling suggested that significant reductions, up to 90%, in transverse vibration amplitude were predicted. The new designs were used to take measurements in the same flow conditions as the poorly designed wires and were seen to be free from measurement anomalies. These improved designs are easily manufactured using the standard DANTEC wire repair station and 5 μm Wollaston wire.

In Chapter 4, the control technique is applied to the second problem under investigation here, milling tool chatter during surface machining. Milling tool chatter causes surface roughness and reduces machining speeds. The approach discussed here is a unique one, since it involves an 'add-on' solution. An 'adaptor' is proposed to be added between the rigid chuck and the cutting tool. This adaptor gives the desired cross sectional step change required for this technique to be employed. Laboratory experiments confirmed the numerical predictions that a reduction in tip displacement amplitude of around 45% is possible. This suggested solution would be easily implemented into practice since the existing plant equipment would not need to be replaced or modified.

Chapter 5 discusses the last of the three problems investigated in this thesis, that of arrow oscillation when released from an archer's bow. Upon release, the arrow experiences a large axial force, causing it to buckle. This buckling induces free vibrations once the arrow is clear from the bow. Such oscillations lead to shot inaccuracy and poor flight. The arrow is not suitable for the existing forms of vibration control, since it is a projectile, and hence, free from any constraints. The technique developed in this thesis enables the application of another 'add-on' solution. Once again, the addition requires a significant step change in cross sectional diameter. The numerical simulations suggest that, after 0.1 seconds, the tip displacement of a modified arrow is half that of the original arrow. Time did not permit experimental verification of this prediction.

The candidate would like to see this work continued by the next generation of postgraduate students and would be happy to work alongside any future resurgence in this work.

REFERENCES

[1] **Hain, H. L., Heintzel, J. L. and Lenigang, C. C.,** 1988 Shock vibration handbook, 3rd ed., Chapter 34 McGraw-Hill book Company.

[2] **Rao, S. S.,** 1995 Mechanical Vibrations 3rd Ed. Addison-Wesley Publishing, p 603.

[3] **Panossian, H. V.,** 1992 Structural damping enhancement via non-obstructive particle damping technique, Journal of Vibration and Acoustics, January, Vol 114, pp 41-105.

[4] **Ogata, K.,** 1997 Modern Control Engineering. Prentice Hall, Minnesota. 3rd ed.

[5] **Li, Y. Q.,** 1994 Analysis of vibration reduction via local structural modification, Masters thesis, Victoria University of Technology, Melbourne.

[6] **Cha, P. D. and Pierre, C.,** 1999 Imposing nodes to the normal modes of a linear elastic structure. Journal of Sound and Vibration (1999), Issue 219(4), pp 669-687.

[7] **Mottershead, J. E.** and **Lallement, G.,** 1999 Vibration nodes, and the cancellation of poles and zeros by unit-rank modifications to structures. Journal of Sound and Vibration (1999), Issue 222(5), pp 833-851.

[8] **Turan, Ö. F.**, **Semercigil, S. E.** and **Chukkapalli, G.,** 1993 Effect of structural vibrations on hot-wire probe response. Measurement Science and Technology, vol. 4, pp. 1416-1425.

[9] **Anderson, C. S., Semercigil, S. E.** and **Turan, Ö. F.** 1998 An investigation of the structural dynamics of hot-wire probes. Proceedings of the 13th Australasian Fluid Mechanics Conference, pp. 75-78, Melbourne, Australia.

[10] **MATLAB®**, 1995, *The student edition of Matlab*, Mathworks Inc., Prentice Hall. Version 5.1.

[11] **DANTEC** Electro Medical and Scientific Equipment Ltd *Probe Catalogue* Publication No. 2201 E (Denmark) 1982, 10.

[12] **Turan, Ö. F.**, 1988 Further study of a New Method of Evaluating Turbulence Dissipation. Ph.D. Thesis, University of Manitoba, Winnipeg, Manitoba, Canada.

[13] **Lomas, C. G.,** 1986 Fundamentals of hot-wire anemometry. Cambridge University Press, New York.

[14] **Bruun, H. H.,** 1995 Hot-wire anemometry: Principles and signal analysis. Oxford University Press, New York.

[15] **Perry A. E. and Morrison G. L.,** 1971. *Journal of Fluid Mechanics*, 50, 815-925. Vibration of hot-wire anemometer filaments.

[16] **Perry A. E. and Morrison G. L.,** 1972. *Journal of Physics E: Scientific Instruments*, **5**, 1005-1008. Errors caused by hot-wire filament vibration.

[17] **Champagne, F. H.,** 1966. Ph.D. thesis, University of Washington. Turbulence measurements with inclined hot-wires.

[18] **Comte-Bellot, G.,** 1976. *Annual Review of Fluid Mechanics*, 8, 209-230. Hot-wire anemometry.

[19] **Turan, Ö.F. and Azad, R. S.,** 1993. *Experimental Thermal Fluid Sci*. 6, 292-308. Comparison of the zero-wire-length dissipation technique with spectral corrections and the effect of high turbulence intensity.

[20] **HP VEE** (Hewlett Packard Visual Engineering Environment Software), Version 4.01. This software is used for data acquisition.

[21] **Dang, T.,** 1987 Experimental Investigation of the Hot-Film Anemometry in Fully-Developed Turbulent Pipe Flow. M. Sc. Thesis, University of Manitoba, Winnipeg, Manitoba, Canada.

[22] **Anderson, C. S., Semercigil, S. E., and Turan Ö. F.,** International Fluids and Anemometry Symposium, Melbourne Australia, 2000.

[23] **Anderson, C. S., Semercigil, S. E., and Turan Ö. F.,** 19^{th} international Model Analysis Conference, Orlando, 2001

[24] **R.N. Arnold,** The mechanism of tool vibration in the cutting of steel, Proceedings, Institute of Mechanical Engineers 154 (1946) 261–276.

[25] **M.E. Merchant,** Basic Mechanics of the Metal-Cutting Process, Journal of Applied Mechanics, II, (Transactions of the ASME, 66) (1944) A-168.

[26] **S.A. Tobias,** Machine Tool Vibration, Blackie and Sons Ltd, Glasgow, 1965.

[27] **F. Koenigsberger** and **J. Tlusty,** Machine Tool Structures—Stability Against Chatter, vol. 1, Pergamon Press, Oxford, 1967.

[28] **J. Tlusty,** Machine Dynamics, in R. I. King (editor), Handbook of High Speed Machining Technology, Chapman and Hall, New York, 1985.

[29] **R. Teltz,** and **M. A. Elbestawi,** Hierarchical, Knowledge-Based Control in Turning, Journal of Dynamics Systems, Measurement, and Control 115 (1993) 122 – 132.

[30] **S. C. Lin** and **M. R. Hu,** Low Vibration Control System in Turning, International Journal of Machine Tools and Manufacture 35(5) (1992) 629 – 640.

[31] **L. Hakansson, I. Claesson** and **T. Lago** Active Control of Machine Tool Chatter, Proceedings of the International Modal Analysis Conference – IMAC v2. SEM, Bethel, CT, USA (1999) pp1826 – 1831

[32] **S. K. Choudhury, N. N. Goudimenkos V. A.** and **Kudinov,** On-Line Control of Machine Tool Vibration in Turning, International Journal of Machine Tools and Manufacture, 37(6) (1997) 801 – 811.

[33] **Y. S. Liao** and **Y. C. Young,** A New On-Line Spindle Speed Regulation Strategy for Chatter Control, International Journal Machine Tools and Manufacture, 36 (1996) 651 – 660.

[34] **Y. S. Tarng** and **E. C., Lee,** A Critical Investigation of the Phase Shift Between the Inner and Outer Modulation for the Control of Machine Tool Chatter, International Journal of Machine Tools and Manufacture 37(12) (1997) 1661-1672.

[35] **Y. S. Tarng, J. Y Kao** and **E. C.,** Lee, Chatter Suppression in Turning Operations with a Tuned Vibration Absorber, Journal of Materials Processing Technology, 105(2000) 55 –60

[36] **M. Wang** and **R. Fei,** On-line Chatter Detection and Control in Boring Based on an Electorheological Fluid, Mechatronics 11 (2001) 779-792.

[37] **J. H. Wang** and **K. N. Lee** Suppression of Chatter Vibration of a CNC Machine Centre – An Example, Mechanical Systems and Signal Processing, 10(50) (1996) 551 – 560.

[38] **J. K. Choi** and **D. G. Lee** Manufacture of a Carbon Fibre-Epoxy Composite Spindle-Bearing System for a Machine Tool, Composite Structures, 37 (1997) 241 – 251.

[39] **C. S. Anderson, S. E. Semercigil** and **Ö. F. Turan,** Vibration control of stepped beams: new designs for hot-wire probes, Journal of Sound and Vibration (in press).

[40] **C. H. Lee** and **K. P. Byrne,** Impact Statistics for a Random Rattling System, Journal of Sound and Vibration, 119(3) (1987) 529-543.

[41] **Tapley, J.,** http://homepage.ntworld.com/joetapley/vt.html.

[42] **Kooi, B. W. and Sparenberg, J. A.,** On the Mechanics of the Arrow: Archer's Paradox, Journal of Engineering Mathematics, 31(4) (1997) pp 285-306.

[43] **J. C. Snowden**, Vibration and Shock in Damped Mechanical Systems, New York, Wiley International, 1968.

APPENDIX A

MATLAB® PURPOSE WRITTEN PROGRAM AND USERS NOTES

Software for the
Numerical simulation of vibration response of beam like structures to broadband random excitation

Christopher S. Anderson and S. Eren Semercigil

School of the Built Environment
Victoria University of Technology

Footscray Campus
PO BOX 14428 MCMC
Melbourne, Victoria 8001
AUSTRALIA

E-mail; eren@dingo.vu.edu.au

INTRODUCTION

This MATLAB® m-file calculates the natural frequencies of particular beam geometries as one parameter, such as overall length is varied. Furthermore, it takes specific geometries, and determines their vibration response to a broad-band random excitation force.

The numerical model of the beam is shown below. In this figure, the middle section has d and L for diameter and length, whereas d_g, L_g and L_o represent the diameter and the length of the thicker ends and the total length of the beam, respectively.

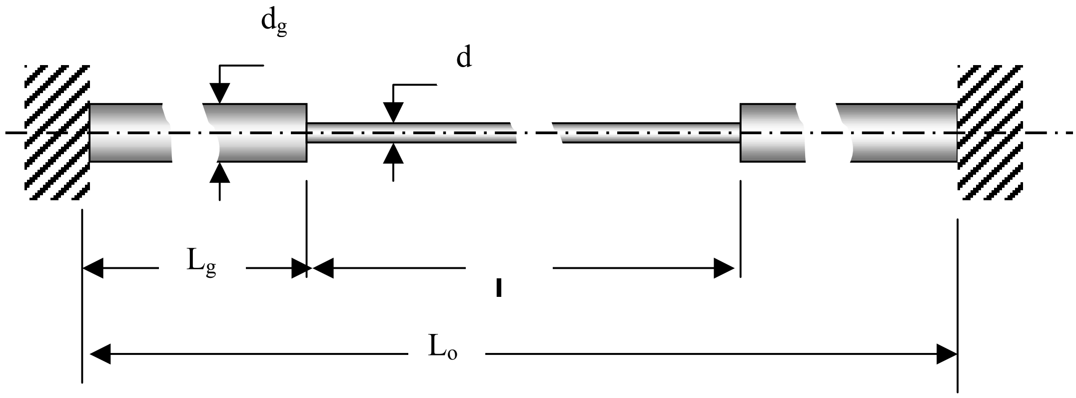

Modifications to the model available within the program are:

- Boundary conditions (pinned, fixed, slider, free)
- Concentrated point loads
- Additional supports (pinned, fixed, slider)
- Type of excitation input (random, sinusoidal, static)
- Beam geometry (L, Lg/l, dg, d)
- Beam properties (E, I, ρ,A)
- Number of nodes along beam length

Each of these options will be discussed individually in the following sections.

BOUNDARY CONDITIONS

The boundary conditions for the beam can be easily modified in the program at this location:

```
%*********BOUNDARY CONDITIONS*************%
%m(2*node,:)=[];% remove this line if you want the RHS support to
pivot
%m(:,2*node)=[];% remove this line if you want the RHS support to
pivot
m(2*node-1,:)=[];% remove this line if you want the RHS support to
move
m(:,2*node-1)=[];% remove this line if you want the RHS support to
move
m(1,:)=[];       % remove this line if you want the LHS support to
move
m(:,1)=[];       % remove this line if you want the LHS support to
move
m(1,:)=[];     % remove this line if you want the LHS support to
pivot
m(:,1)=[];     % remove this line if you want the LHS support to
pivot
%k(2*node,:)=[];% remove this line if you want the RHS support to
pivot
%k(:,2*node)=[];% remove this line if you want the RHS support to
pivot
k(2*node-1,:)=[];% remove this line if you want the RHS support to
move
k(:,2*node-1)=[];% remove this line if you want the RHS support to
move
k(1,:)=[];     % remove this line if you want the LHS support to move
k(:,1)=[];     % remove this line if you want the LHS support to move
k(1,:)=[];     % remove this line if you want the LHS support to
pivot
k(:,1)=[];     % remove this line if you want the LHS support to
pivot
```

The example shown above is for a beam that has a fixed or built-in support at the left hand side, while the right hand side is a pinned connection. As the text in green shows, the boundary conditions can be tailored to specific needs.

ANY MODIFICATIONS TO BOUNDARY CONDITIONS MUST BE DONE IN TWO PLACES, ONCE FOR THE NATURAL FREQUENCY SECTION AND ONCE FOR THE VIBRATION RESPONSE SECTION.

CONCENTRATED POINT LOADS

Point loads can be used to model lumped mass in the system such as gears, motors etc. that are present on the beam axis. The mass, in kg, of the point load is entered at the top of the program:

```
M=0                 %Mass of the extra mass [kg] (zero for not
attached)%
```

The point load can be maintained at a given node, or shifted from node to node as the program progresses as shown below:

```
nodem=z;
Xm=2*nodem+1;                      % The node axis of extra mass%
m(Xm,Xm)=m(Xm,Xm)+M;                     % Add extra mass at the nodem%
```

The point load can be kept at a constant node by letting 'nodem=?' where '?' is the node desired.

ADDITIONAL SUPPORTS

Additional supports can be added as follows:

```
if z>1 & z<request,
%m(2*z,:)=[];% add this line if you want the znode support to not
pivot
%m(:,2*z)=[];% add this line if you want the znode support to not
pivot
%k(2*z,:)=[];% add this line if you want the znode support to not
pivot
%k(:,2*z)=[];% add this line if you want the znode support to not
pivot
m(2*z-1,:)=[];% add this line if you want the znode support to not
move
m(:,2*z-1)=[];% add this line if you want the znode support to not
move
k(2*z-1,:)=[];% add this line if you want the znode support to not
move
k(:,2*z-1)=[];% add this line if you want the znode support to not
move
end;
```

The example shown is for a pinned support to be placed at a different node 'z' for each pass through the loop. Again, if the point of application is desired to be constant, simply change the 'z' in the above expressions to the desired node number.

ANY MODIFICATIONS TO ADDED SUPPORTS MUST BE DONE IN TWO PLACES, ONCE FOR THE NATURAL FREQUENCY SECTION AND ONCE FOR THE VIBRATION RESPONSE SECTION.

TYPE OF EXCITATION INPUT

The force data is loaded into the program as follows:

```
% Step #1%
load force;
force=real(force);
delti=1e-5;
```

This example gives a broad-band random excitation. If a sinusoidal force is required, replace the force data with sinusoidal data. Also if a static load is desired, simply make the force data constant, at the desired value.

BEAM GEOMETRY

The beam geometry can be altered in many ways using the following:

```
%********Input of parameters********%
blocks=1;                % Number of step changes in cross section%
Lo=1;                    % Total length of the beam [m]%
E=207e9;                 % Young's Modulus for each block [Pa]%
dia=30e-3;               % Diameter for each block [m]%
density=7850;            % Density for each block [kg/m^3]%

%********Natural frequency distribution****************%
smoothness=30;        % number of calc's to be performed for range%
l=Lo;
freq(1:smoothness,5)=0;           %Initialise a matrix for later use%
beammass=(pi*dia^2*l*density/4)   %Calculate mass of each beam
geometry%
M=0                %Mass of the extra mass [kg] (zero for not
attached)%


for z=1:smoothness,%start loop for natural frequency for each
geometry%

   S=0;
   start=1;                % Which node to start at (must be 1)%
   data=zeros((5000),3);   % Parameter matrix (row node-1, column 3)%
   for i=1:blocks,
      request=smoothness;  % Number of nodes in each block%
      S=S+request;         % Cumulative node number for end of loop%
      for j=start+request-1,
         EI=E*(4*atan(1)*(dia^4)/64);        % Calculate EI %
         pA=density*(4*atan(1)*(dia^2)/4);   % Calculate
density*Area%
         data(start:j,1)=data(start:j,1)+EI; % Fill matrix%
         data(start:j,2)=data(start:j,2)+pA; % fill matrix%
         data(start:j,3)=data(start:j,3)+l/request;   % Fill matrix%
         start=j+1;
      end

   end
```

Firstly, the number of blocks is the number of step changes required in cross sectional area. If using a uniform beam, then blocks=1, whereas for the beam shown in the introduction, blocks=3. Lo is simply the total beam length, if the length changes for each beam, simply make it Lo(z) and place it in the loop.

BEAM PROPERTIES

The beam properties can be changed simply by entering them into the following:

```
E=207e9;                    % Young's Modulus for each block [Pa]%
dia=30e-3;                  % Diameter for each block [m]%
density=7850;               % Density for each block [kg/m^3]%
```

The example shown above is for blocks=1. If there are more blocks, then there must be an equivalent number of entries into each of the above matrices. An example below shows the layout for three blocks, where the first blocks is aluminum at 45mm diameter, the next block is steel at 6 mm diameter, and the last is aluminum at 45mm diameter again:

```
blocks=3;
L=3;
E=[71e9,210e9,71e9];
dia=[45e-3,6e-3,45e-3];
density=[2745,7874,2745];
ratio=[0.5 0.77 1 1.13 1.5 2 2.5 3];
l(length(ratio),3)=0;
for g=1:length(ratio),
   l(g,2)=L/(2*ratio(g)+1);
   l(g,1)=ratio(g)*l(g,2);
   l(g,3)=l(g,1);
end

for z=1:length(ratio),
   S=0;
   start=1;
   data=zeros((5000),3);     % parameter matrix (row node-1, column 3)
   for i=1:blocks,
      request=10;
      S=S+request;
      for j=start+request-1,
         EI=E(i)*(4*atan(1)*(dia(i)^4)/64);
         pA=density(i)*(4*atan(1)*(dia(i)^2)/4);
         data(start:j,1)=data(start:j,1)+EI;
         data(start:j,2)=data(start:j,2)+pA;
         data(start:j,3)=data(start:j,3)+l(z,i)/request;
         start=j+1;
      end %from for j=start...

   end %from for i=1:blocks...
```

The above example performs the loop for eight different ratios of end length to middle length (lg/l). As many blocks can be added as desired, provided the same number of data entries appear in all of the matrices called in the above lines.

ANY MODIFICATIONS TO THE NUMBER OF BLOCKS MUST BE DONE IN TWO PLACES, ONCE FOR THE NATURAL FREQUENCY SECTION AND ONCE FOR THE VIBRATION RESPONSE SECTION.

NUMBER OF NODES ALONG THE BEAM LENGTH

This can easily be changed by entering the desired number into the program as follows:

```
request=10;
```

ANY MODIFICATIONS TO THE NUMBER OF NODES MUST BE DONE IN TWO PLACES, ONCE FOR THE NATURAL FREQUENCY SECTION AND ONCE FOR THE VIBRATION RESPONSE SECTION.

EXAMPLE OF EXPECTED OUTPUT

The expected output for the program in the form attached is shown below. The program is begun by typing 'beamanalysis' at the Matlab® command prompt, provided that the beamanalysis.m file is in the Matlab® path. Firstly, the program displays the following:

beammass = 5.5488
M = 0

z = 1
z = 2
z = 3
:
:
z = *smoothness value*

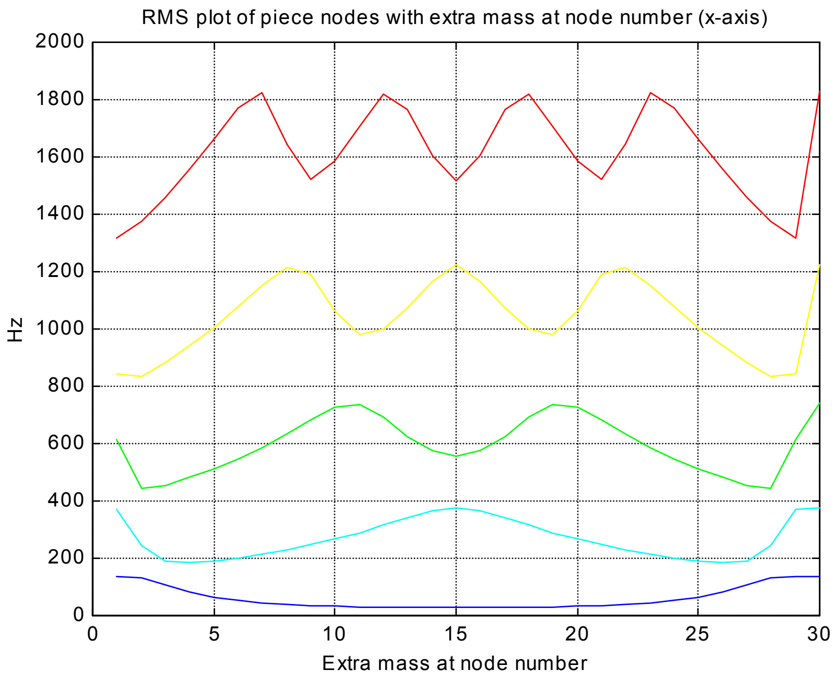

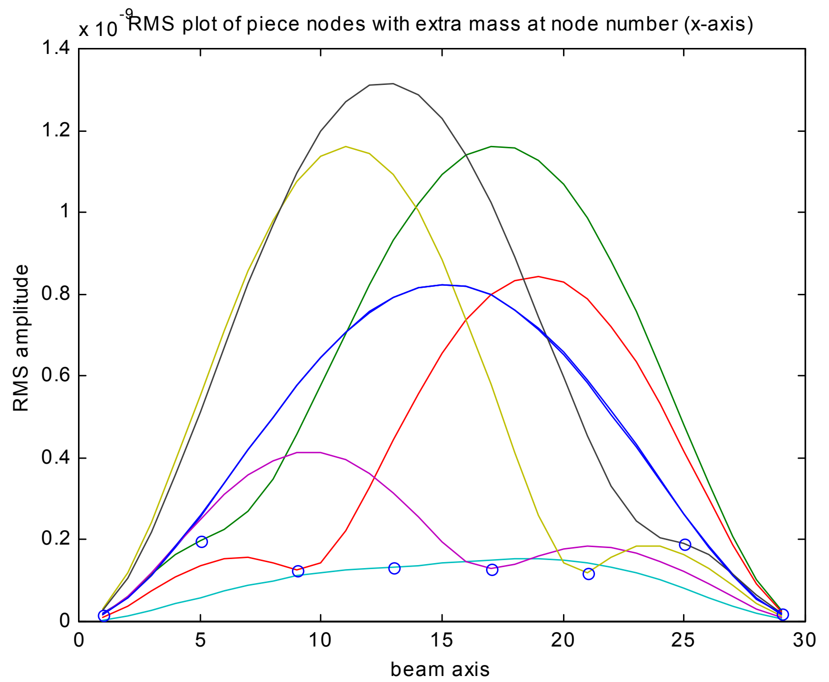

A copy of the program (BEAMANALYSIS) is attached. Supplementary to this software manual, the program itself offers individual explanations for each line, with suggestions of how to tailor the program to the users specific needs. Should any further questions arise, contact can be made with the author, Chris Anderson, via Victoria University of Technology, School of the Built Environment (Mechanical Engineering).

ACKNOWLEDGMENTS

The assistance of Dr Semercigil is greatly appreciated, further appreciation goes to Qimming Moa who provided the starting point and inspiration for this software.

```
%*********************************************************************
%*********************************************************************
%************************ BEAMANALYSIS ****************************
%*********************************************************************
%************************* Written by ****************************
%*********************************************************************
%******************* Chris Anderson 1998 *************************
%*********************************************************************
%*********************************************************************
%*********************************************************************

% This program can calculate the natural frequencies of different
beam geometries as one beam parameter is varied.  It also calculates
the displacement response to an input force (force.mat).%



close all;
clear all
clc;


%********Input of parameters********%
blocks=1;                % Number of step changes in cross section%
Lo=1;                    % Total length of the beam [m]%
E=207e9;                 % Young's Modulus for each block [Pa]%
dia=30e-3;               % Diameter for each block [m]%
density=7850;            % Density for each block [kg/m^3]%


%********Natural frequency distribution****************%

smoothness=30;           % number of calc's to be performed for range%
l=Lo;
freq(1:smoothness,5)=0;           % Initialise a matrix for later use%
beammass=(pi*dia^2*l*density/4); % Calculate mass of beam geometry%
M=50;                             % Extra mass
fprintf('beammass=%2.2f\n',beammass);
fprintf('M=%3.1f\n',M);


for z=1:smoothness,%start loop for natural frequency for each
geometry%

   S=0;
   start=1;                  % which node to start at (must be 1)%
   data=zeros((5000),3);     % parameter matrix (row node-1, column 3)%
   for i=1:blocks,
      request=smoothness;       % Number of nodes in each block%
      S=S+request;              % cumulative node number for end of
loop%
      for j=start+request-1,
         EI=E*(4*atan(1)*(dia^4)/64);      % calculate EI %
         pA=density*(4*atan(1)*(dia^2)/4);% claculate density*Area%
         data(start:j,1)=data(start:j,1)+EI; % fill matrix%
         data(start:j,2)=data(start:j,2)+pA; % fill matrix%
         data(start:j,3)=data(start:j,3)+l/request;    % fill matrix%
         start=j+1;
      end
```

```
   end


data(max(find(data(:,1)))+1:end,:)=[];%attenuate unused matrix cells%

%fprintf('Notes:node number is from 0 to  %6.2f \n',S);
node=S+1;                    % total number of node

%***[calculation of the globe mass/stiffness matrices by FEM]****%
mi=zeros(4*(node-1),4);      % zeros matrix for basic mass matrix
ki=zeros(4*(node-1),4);      % zeros matrix for basic stiffness matrix

%----define basic mass/stiffness matrix of all elements---%
for i=1:(node-1)
    m0=data(i,2:2).*data(i,3:3)/420;      % pA=data(i,2:2)
l=data(i,3:3)

    m2=[156            22*data(i,3:3)      54              -
13*data(i,3:3);
       22*data(i,3:3)  4*(data(i,3:3).^2) 13*data(i,3:3) -
3*(data(i,3:3).^2);
       54          13*data(i,3:3)      156             -
22*data(i,3:3);
      -13*data(i,3:3) -3*(data(i,3:3).^2) -22*data(i,3:3)
4*(data(i,3:3).^2)];

    mi((1+4*(i-1)):4*i,1:4)= ...
    mi((1+4*(i-1)):4*i,1:4)+m0*m2;     %mass matrix of all elements

    k2=[12,          6*data(i,3:3),     -12,             6*data(i,3:3);
       6*data(i,3:3), 4*(data(i,3:3).^2), -6*data(i,3:3),
2*(data(i,3:3).^2);
       -12,        -6*data(i,3:3),      12,            -6*data(i,3:3);
       6*data(i,3:3), 2*(data(i,3:3).^2), -6*data(i,3:3),
4*(data(i,3:3).^2)];

    k0=data(i,1:1)/(data(i,3:3).^3);      % EI=data(i,1:1)

    ki((1+4*(i-1)):4*i,1:4)= ...
    ki((1+4*(i-1)):4*i,1:4)+k0*k2;     % stiffness matrix of all
elements
end

%-------glob matrics of mass and stiffness--------%
m=zeros(2*node,2*node);
k=zeros(2*node,2*node);

for n=0:(node-2)
    m((1+2*n):(4+2*n),(1+2*n):(4+2*n))= ...
    m((1+2*n):(4+2*n),(1+2*n):(4+2*n))+mi((1+4*n):4*(n+1),1:4);
    k((1+2*n):(4+2*n),(1+2*n):(4+2*n))= ...
    k((1+2*n):(4+2*n),(1+2*n):(4+2*n))+ki((1+4*n):4*(n+1),1:4);
end

nodem=z;
Xm=2*nodem+1;                 %the node axis of extra mass
m(Xm,Xm)=m(Xm,Xm)+M;          %add extra mass at nodem
```

```
%**********BOUNDARY CONDITIONS*************%
m(2*node,:)=[];% remove this line if you want the RHS support to
pivot
m(:,2*node)=[];% remove this line if you want the RHS support to
pivot
m(2*node-1,:)=[];% remove this line if you want the RHS support to
move
m(:,2*node-1)=[];% remove this line if you want the RHS support to
move
m(1,:)=[];      % remove this line if you want the LHS support to move
m(:,1)=[];      % remove this line if you want the LHS support to move
m(1,:)=[];      % remove this line if you want the LHS support to
pivot
m(:,1)=[];      % remove this line if you want the LHS support to
pivot
k(2*node,:)=[];% remove this line if you want the RHS support to
pivot
k(:,2*node)=[];% remove this line if you want the RHS support to
pivot
k(2*node-1,:)=[];% remove this line if you want the RHS support to
move
k(:,2*node-1)=[];% remove this line if you want the RHS support to
move
k(1,:)=[];      % remove this line if you want the LHS support to move
k(:,1)=[];      % remove this line if you want the LHS support to move
k(1,:)=[];      % remove this line if you want the LHS support to
pivot
k(:,1)=[];      % remove this line if you want the LHS support to
pivot

% apply a support at node z%
if z>1 & z<request,
%m(2*z,:)=[]; %add this line if you want the znode support to not
pivot
%m(:,2*z)=[]; %add this line if you want the znode support to not
pivot
%k(2*z,:)=[]; %add this line if you want the znode support to not
pivot
%k(:,2*z)=[]; %add this line if you want the znode support to not
pivot
%m(2*z-1,:)=[];%add this line if you want the znode support to not
move
%m(:,2*z-1)=[];%add this line if you want the znode support to not
move
%k(2*z-1,:)=[];%add this line if you want the znode support to not
move
%k(:,2*z-1)=[];%add this line if you want the znode support to not
move
end;

%*****[Solver of eigenvalue, eigenvector and natural frequency]*****%
la=length(m);                     % dimension of mass matrix
[eigenvector,d]=eig(k,m);         % eigenvalue and eigenvector
d1=(d.^(1/2));                    % natural frequency

for i=1:1:la                   % eigenvalue/natural frequency matrix
   eigenvalue(i)=d(i,i);
   frequency(i)=d1(i,i);
end
```

```
eigenvalue=sort(eigenvalue);
frequency=sort(frequency);
%for i=1:la
%fprintf('eigenvalue:%6.2e natural frequency:%6.2f
\n',eigenvalue(i),frequency(i));
%end

w1=frequency(1);w2=frequency(2);w3=frequency(3);w4=frequency(4);w5=fr
equency(5);
W1=w1/2/pi;
W2=w2/2/pi;
W3=w3/2/pi;
W4=w4/2/pi;
W5=w5/2/pi;

freq(z,1)=W1;
freq(z,2)=W2;
freq(z,3)=W3;
freq(z,4)=W4;
freq(z,5)=W5;

fprintf('z=%0.0f\n',z);
end %from for z=1:smoothness;

scale=1:request;
figure,...
plot(scale,freq(1:smoothness,1),'b-',scale,freq(1:smoothness,2),'c-
',scale,freq(1:smoothness,3),'g-',scale,freq(1:smoothness,4),'y-
',scale,freq(1:smoothness,5),'r-'),...
ylabel('Hz'),...
xlabel('Extra mass at node number'),...
title('RMS plot of piece nodes with extra mass at node number (x-
axis)'),...
%axis([0 30 0 2000]),...
grid on,...
zoom on;
drawnow;



%*********************************************************************
%*********************************************************************
%*******  NEWMARK-B Method (Average Acceleration Method)   **********
%*********************************************************************
%*********************************************************************
%***********************  By Chris Anderson   ***********************
%*********************************************************************
%*********************************************************************
%*********************************************************************
%*********************************************************************

clc;
fclose all;
format long;

%********[Input of parameter]********%
steps=5000;
ratio=[1 1 1 1 1 1 1 1];

for z=1:8,
```

```
   S=0;
   start=1;
   data=zeros((5000),3);     % parameter matrix
   for i=1:blocks,
      request=30;
      S=S+request;
      for j=start+request-1,
         EI=E*(4*atan(1)*(dia^4)/64);
         pA=density*(4*atan(1)*(dia^2)/4);
         data(start:j,1)=data(start:j,1)+EI;
         data(start:j,2)=data(start:j,2)+pA;
         data(start:j,3)=data(start:j,3)+l/request;
         start=j+1;
      end %from j=start...

   end %from i=1:blocks...

   data(max(find(data(:,1)))+1:end,:)=[];

node=S+1;                    % total number of node

%***[calculation of the globe mass/stiffness matrices by FEM]****%
mi=zeros(4*(node-1),4);      % zeros matrix for basic mass matrix
ki=zeros(4*(node-1),4);      % zeros matrix for basic stiffness matrix

%----define basic mass/stiffness matrix of all elements---%
for i=1:(node-1)
    m0=data(i,2:2).*data(i,3:3)/420;      % pA=data(i,2:2)
l=data(i,3:3)

    m2=[156           22*data(i,3:3)      54             -
13*data(i,3:3);
       22*data(i,3:3)  4*(data(i,3:3).^2) 13*data(i,3:3) -
3*(data(i,3:3).^2);
       54          13*data(i,3:3)      156             -
22*data(i,3:3);
      -13*data(i,3:3) -3*(data(i,3:3).^2) -22*data(i,3:3)
4*(data(i,3:3).^2)];

    mi((1+4*(i-1)):4*i,1:4)= ...
    mi((1+4*(i-1)):4*i,1:4)+m0*m2;     %mass matrix of all elements

    k2=[12,          6*data(i,3:3),     -12,             6*data(i,3:3);
       6*data(i,3:3), 4*(data(i,3:3).^2), -6*data(i,3:3),
2*(data(i,3:3).^2);
       -12,         -6*data(i,3:3),      12,             -6*data(i,3:3);
       6*data(i,3:3), 2*(data(i,3:3).^2), -6*data(i,3:3),
4*(data(i,3:3).^2)];

    k0=data(i,1:1)/(data(i,3:3).^3);      % EI=data(i,1:1)

    ki((1+4*(i-1)):4*i,1:4)= ...
    ki((1+4*(i-1)):4*i,1:4)+k0*k2;     % stiffness matrix of all
elements
end


%-------glob matrics of mass and stiffness--------%

m=zeros(2*node,2*node);
k=zeros(2*node,2*node);
```

```
for n=0:(node-2)
    m((1+2*n):(4+2*n),(1+2*n):(4+2*n))= ...
    m((1+2*n):(4+2*n),(1+2*n):(4+2*n))+mi((1+4*n):4*(n+1),1:4);
    k((1+2*n):(4+2*n),(1+2*n):(4+2*n))= ...
    k((1+2*n):(4+2*n),(1+2*n):(4+2*n))+ki((1+4*n):4*(n+1),1:4);
end

nodem=z*4-3;
Xm=2*nodem+1;                %the node axis of extral mass
m(Xm,Xm)=m(Xm,Xm)+M;         %add extral mass at the nodem



%**********BOUNDARY CONDITIONS*************%
m(2*node,:)=[];% remove this line if you want the RHS support to
pivot
m(:,2*node)=[];% remove this line if you want the RHS support to
pivot
m(2*node-1,:)=[];% remove this line if you want the RHS support to
move
m(:,2*node-1)=[];% remove this line if you want the RHS support to
move
m(1,:)=[];      % remove this line if you want the LHS support to move
m(:,1)=[];      % remove this line if you want the LHS support to move
m(1,:)=[];      % remove this line if you want the LHS support to
pivot
m(:,1)=[];      % remove this line if you want the LHS support to
pivot
k(2*node,:)=[];% remove this line if you want the RHS support to
pivot
k(:,2*node)=[];% remove this line if you want the RHS support to
pivot
k(2*node-1,:)=[];% remove this line if you want the RHS support to
move
k(:,2*node-1)=[];% remove this line if you want the RHS support to
move
k(1,:)=[];      % remove this line if you want the LHS support to move
k(:,1)=[];      % remove this line if you want the LHS support to move
k(1,:)=[];      % remove this line if you want the LHS support to
pivot
k(:,1)=[];      % remove this line if you want the LHS support to
pivot

% apply a support at node z%
z=(z*4)-3;
if z>1 & z<request,
%m(2*z,:)=[]; %add this line if you want the znode support to not
pivot
%m(:,2*z)=[]; %add this line if you want the znode support to not
pivot
%k(2*z,:)=[]; %add this line if you want the znode support to not
pivot
%k(:,2*z)=[]; %add this line if you want the znode support to not
pivot
%m(2*z-1,:)=[];%add this line if you want the znode support to not
move
%m(:,2*z-1)=[];%add this line if you want the znode support to not
move
%k(2*z-1,:)=[];%add this line if you want the znode support to not
move
```

```
%k(:,2*z-1)=[];%add this line if you want the znode support to not
move
end;
z=(z+3)/4;
%end

%*****[Solver of eigenvalue, eigenvector and natural
frequency]******%
la=length(m);                       % dimension of mass matrix
[eigenvector,d]=eig(k,m);           % eigenvalue and eigenvector
d1=(d.^(1/2));                      % natural frequency

for i=1:1:la                     % eigenvalue/natural frequency matrix
   eigenvalue(i)=d(i,i);
   frequency(i)=d1(i,i);
end

eigenvalue=sort(eigenvalue);
frequency=sort(frequency);
%for i=1:la
%fprintf('eigenvalue:%6.2e natural frequency:%6.2f
\n',eigenvalue(i),frequency(i));
%end

w1=frequency(1);w2=frequency(2);w3=frequency(3);w4=frequency(4);w5=fr
equency(5);
W1=w1/2/pi;
W2=w2/2/pi;
W3=w3/2/pi;
W4=w4/2/pi;
W5=w5/2/pi;

% Step #1%
% Load the force data file created by 'Force2.m'%
load force;
force=real(force);
delti=1e-5;
%time=delti:delti:length(force)*delti;
%length(force-1)
%length(time-1)

% DETERMINE damping matrix%
cc=0.01;           % assumed value for first and second mode shapes
a1=(2*cc)/(w1+w2);
a0=w1*((2*cc)-(a1*w1));
c=a0*m+a1*k;

% Step #2
% Convert force data into a force matrix
p(1:length(force),1:length(m))=0;
%for i=1:length(force),
 %  for j=5,
  %    p(i,j)=force(i);   % Change 'force(i)' if non-uniform force
distribution
  %end
%end
p(:,((length(m))/2)-2)=force;


% Step #3
% Solve for kistar
```

```
kistar=k+((2*c/delti)+m*(4/delti^2));

% Step #4
% Set INITIAL BEAM CONDITIONS
x1(1,1:length(m))=0;        % no point on beam has displacement%
dx1(1,1:length(m))=0;       % no point on beam has none-zero gradient%


% Step #5
% Calculate initial acceleration
   ddx1=p(1,:)*inv(m);

% Step #6
% Begin a loop to perform repetative calc's of x, dx and ddx
%delete xprobe13.txt;
fid0 = fopen('p30rms.txt','w');
fid1 = fopen('p3001.txt','w');
fid2 = fopen('p3002.txt','w');
fid3 = fopen('p3003.txt','w');
fid4 = fopen('p3004.txt','w');
fid5 = fopen('p3005.txt','w');
fid6 = fopen('p3006.txt','w');
fid7 = fopen('p3007.txt','w');
fid8 = fopen('p3008.txt','w');
fid9 = fopen('p3009.txt','w');
fid10 = fopen('p3010.txt','w');
fid11 = fopen('p3011.txt','w');
fid12 = fopen('p3012.txt','w');
fid13 = fopen('p3013.txt','w');
fid14 = fopen('p3014.txt','w');
fid15 = fopen('p3015.txt','w');
fid16 = fopen('p3016.txt','w');
fid17 = fopen('p3017.txt','w');
fid18 = fopen('p3018.txt','w');
fid19 = fopen('p3019.txt','w');
fid20 = fopen('p3020.txt','w');
fid21 = fopen('p3021.txt','w');
fid22 = fopen('p3022.txt','w');
fid23 = fopen('p3023.txt','w');
fid24 = fopen('p3024.txt','w');
fid25 = fopen('p3025.txt','w');
fid26 = fopen('p3026.txt','w');
fid27 = fopen('p3027.txt','w');
fid28 = fopen('p3028.txt','w');
fid29 = fopen('p3029.txt','w');



j=1;
rms0=0;
for i=1:steps,
   % Create dpistar
   delpi=p(j+1,:)-p(j,:);
   delpistar=(delpi+(dx1(1,:)*(m*(4/delti)+2*c))+2*ddx1(1,:)*m);

   % Step #7
   % Solve for delxi
   delxi=delpistar*inv(kistar);
   x2(1,:)=x1(1,:)+delxi;

   % Step #8
```

```
   % Solve for VELOCITY(deldxi) and ACCELERATION(delddxi)
   deldxi=delxi*(2/delti)-2*dx1(1,:);
   delddxi=[(delpi)-deldxi*c-delxi*k]*inv(m);

   % Re-initialise start values for next loop calculation. %
   dx2(1,:)=dx1(1,:)+deldxi;
   ddx2(1,:)=ddx1(1,:)+delddxi;
   x1=x2;
   dx1=dx2;
   ddx1=ddx2;

   % Calculate rms values to check stability %
   sqr1=x1(1,27)^2;
   rms=((sqr1+rms0)/i)^(0.5);
   rms0=i*(rms^2);
   xx=x1(1:2:end);


%plot(xx);           %allows video playback of the forced vibration%
%axis([0 30 -5e-6 5e-6]);
%drawnow;


%Write data files, each file will fit onto a 3.5", 1.44M Floppy Disk.
%
   fprintf(fid0,'%e\n',rms);          fprintf(fid1,'%e\n',xx(1));
   fprintf(fid2,'%e\n',xx(2));        fprintf(fid3,'%e\n',xx(3));
   fprintf(fid4,'%e\n',xx(4));        fprintf(fid5,'%e\n',xx(5));
   fprintf(fid6,'%e\n',xx(6));        fprintf(fid7,'%e\n',xx(7));
   fprintf(fid8,'%e\n',xx(8));        fprintf(fid9,'%e\n',xx(9));
   fprintf(fid10,'%e\n',xx(10));      fprintf(fid11,'%e\n',xx(11));
   fprintf(fid12,'%e\n',xx(12));      fprintf(fid13,'%e\n',xx(13));
   fprintf(fid14,'%e\n',xx(14));      fprintf(fid15,'%e\n',xx(15));
   fprintf(fid16,'%e\n',xx(16));      fprintf(fid17,'%e\n',xx(17));
   fprintf(fid18,'%e\n',xx(18));      fprintf(fid19,'%e\n',xx(19));
   fprintf(fid20,'%e\n',xx(20));      fprintf(fid21,'%e\n',xx(21));
   fprintf(fid22,'%e\n',xx(22));      fprintf(fid23,'%e\n',xx(23));
   fprintf(fid24,'%e\n',xx(24));      fprintf(fid25,'%e\n',xx(25));
   fprintf(fid26,'%e\n',xx(26));      fprintf(fid27,'%e\n',xx(27));
   fprintf(fid28,'%e\n',xx(28));      fprintf(fid29,'%e\n',xx(29));


%Loop back through force vector, this allows having a force vector to
% fit onto a floppy disk. %
   if j==8192,
      %disp(rms);
      j=0;
   end
   j=j+1;

end

fclose all;

fid0 = fopen('p30rms.txt','r');
fid1 = fopen('p3001.txt','r');
fid2 = fopen('p3002.txt','r');
fid3 = fopen('p3003.txt','r');
fid4 = fopen('p3004.txt','r');
fid5 = fopen('p3005.txt','r');
fid6 = fopen('p3006.txt','r');
```

```
fid7 = fopen('p3007.txt','r');
fid8 = fopen('p3008.txt','r');
fid9 = fopen('p3009.txt','r');
fid10 = fopen('p3010.txt','r');
fid11 = fopen('p3011.txt','r');
fid12 = fopen('p3012.txt','r');
fid13 = fopen('p3013.txt','r');
fid14 = fopen('p3014.txt','r');
fid15 = fopen('p3015.txt','r');
fid16 = fopen('p3016.txt','r');
fid17 = fopen('p3017.txt','r');
fid18 = fopen('p3018.txt','r');
fid19 = fopen('p3019.txt','r');
fid20 = fopen('p3020.txt','r');
fid21 = fopen('p3021.txt','r');
fid22 = fopen('p3022.txt','r');
fid23 = fopen('p3023.txt','r');
fid24 = fopen('p3024.txt','r');
fid25 = fopen('p3025.txt','r');
fid26 = fopen('p3026.txt','r');
fid27 = fopen('p3027.txt','r');
fid28 = fopen('p3028.txt','r');
fid29 = fopen('p3029.txt','r');


f1=fscanf(fid1,'%e');
f2=fscanf(fid2,'%e');
f3=fscanf(fid3,'%e');
f4=fscanf(fid4,'%e');
f5=fscanf(fid5,'%e');
f6=fscanf(fid6,'%e');
f7=fscanf(fid7,'%e');
f8=fscanf(fid8,'%e');
f9=fscanf(fid9,'%e');
f10=fscanf(fid10,'%e');
f11=fscanf(fid11,'%e');
f12=fscanf(fid12,'%e');
f13=fscanf(fid13,'%e');
f14=fscanf(fid14,'%e');
f15=fscanf(fid15,'%e');
f16=fscanf(fid16,'%e');
f17=fscanf(fid17,'%e');
f18=fscanf(fid18,'%e');
f19=fscanf(fid19,'%e');
f20=fscanf(fid20,'%e');
f21=fscanf(fid21,'%e');
f22=fscanf(fid22,'%e');
f23=fscanf(fid23,'%e');
f24=fscanf(fid24,'%e');
f25=fscanf(fid25,'%e');
f26=fscanf(fid26,'%e');
f27=fscanf(fid27,'%e');
f28=fscanf(fid28,'%e');
f29=fscanf(fid29,'%e');
f0=fscanf(fid0,'%e');

fclose('all');

r1=(mean(f1.^2))^0.5;
r2=(mean(f2.^2))^0.5;
r3=(mean(f3.^2))^0.5;
```

```
r4=(mean(f4.^2))^0.5;
r5=(mean(f5.^2))^0.5;
r6=(mean(f6.^2))^0.5;
r7=(mean(f7.^2))^0.5;
r8=(mean(f8.^2))^0.5;
r9=(mean(f9.^2))^0.5;
r10=(mean(f10.^2))^0.5;
r11=(mean(f11.^2))^0.5;
r12=(mean(f12.^2))^0.5;
r13=(mean(f13.^2))^0.5;
r14=(mean(f14.^2))^0.5;
r15=(mean(f15.^2))^0.5;
r16=(mean(f16.^2))^0.5;
r17=(mean(f17.^2))^0.5;
r18=(mean(f18.^2))^0.5;
r19=(mean(f19.^2))^0.5;
r20=(mean(f20.^2))^0.5;
r21=(mean(f21.^2))^0.5;
r22=(mean(f22.^2))^0.5;
r23=(mean(f23.^2))^0.5;
r24=(mean(f24.^2))^0.5;
r25=(mean(f25.^2))^0.5;
r26=(mean(f26.^2))^0.5;
r27=(mean(f27.^2))^0.5;
r28=(mean(f28.^2))^0.5;
r29=(mean(f29.^2))^0.5;

if z==1,
   p3d301=[r1 r2 r3 r4 r5 r6 r7 r8 r9 r10 r11 r12 r13 r14 r15 r16 r17
r18 r19 r20 r21 r22 r23 r24 r25 r26 r27 r28 r29];
   save p3d301 p3d301
   run=p3d301;
elseif z==2,
   p3d302=[r1 r2 r3 r4 r5 r6 r7 r8 r9 r10 r11 r12 r13 r14 r15 r16 r17
r18 r19 r20 r21 r22 r23 r24 r25 r26 r27 r28 r29];
   save p3d302 p3d302
   run=p3d302;
elseif z==3,
   p3d303=[r1 r2 r3 r4 r5 r6 r7 r8 r9 r10 r11 r12 r13 r14 r15 r16 r17
r18 r19 r20 r21 r22 r23 r24 r25 r26 r27 r28 r29];
   save p3d303 p3d303
   run=p3d303;
elseif z==4,
   p3d304=[r1 r2 r3 r4 r5 r6 r7 r8 r9 r10 r11 r12 r13 r14 r15 r16 r17
r18 r19 r20 r21 r22 r23 r24 r25 r26 r27 r28 r29];
   save p3d304 p3d304
   run=p3d304;
elseif z==5,
   p3d305=[r1 r2 r3 r4 r5 r6 r7 r8 r9 r10 r11 r12 r13 r14 r15 r16 r17
r18 r19 r20 r21 r22 r23 r24 r25 r26 r27 r28 r29];
   save p3d305 p3d305
   run=p3d305;
elseif z==6,
   p3d306=[r1 r2 r3 r4 r5 r6 r7 r8 r9 r10 r11 r12 r13 r14 r15 r16 r17
r18 r19 r20 r21 r22 r23 r24 r25 r26 r27 r28 r29];
   save p3d306 p3d306
   run=p3d306;
elseif z==7,
   p3d307=[r1 r2 r3 r4 r5 r6 r7 r8 r9 r10 r11 r12 r13 r14 r15 r16 r17
r18 r19 r20 r21 r22 r23 r24 r25 r26 r27 r28 r29];
   save p3d307 p3d307
```

```
   run=p3d307;
elseif z==8,
   p3d308=[r1 r2 r3 r4 r5 r6 r7 r8 r9 r10 r11 r12 r13 r14 r15 r16 r17
r18 r19 r20 r21 r22 r23 r24 r25 r26 r27 r28 r29];
   save p3d308 p3d308
   run=p3d308;
end;

fprintf('z=%0.0f\n',z);
fprintf('z=%0.0f\n',z);
end %from for z=1:...



%****************DISPLAY THE FIGURES*****************************%
scale=1:1:29;

figure,...
plot(scale,p3d301,scale,p3d302,scale,p3d303,scale,p3d304,scale,p3d305
,scale,p3d306,scale,p3d307,scale,p3d308,1,p3d302(1),'bo',5,p3d302(5),
'bo',9,p3d303(9),'bo',13,p3d304(13),'bo',17,p3d305(17),'bo',21,p3d306
(21),'bo',25,p3d307(25),'bo',29,p3d308(29),'bo'),...
   title('RMS plot of piece nodes with dg=30mm, for length 1m'),...
   xlabel('beam axis'),...
   ylabel('RMS amplitude'),...
   title('RMS plot of piece nodes with extra mass at node number (x-
axis)'),...
   zoom on;

%maxes=[max(p3d301);max(p3d302);max(p3d303);max(p3d304);max(p3d305);m
ax(p3d306);max(p3d307);max(p3d308)];
%matrix=[ratio' maxes];

%figure,...
%   plot(matrix(:,1),matrix(:,2),'k-',matrix(:,1),matrix(:,2),'k*')
%  title('Peak RMS plot of piece with dg=30mm and L=1m'),...
%   xlabel('mass node position'),...
%   ylabel('RMS amplitude'),...
%   zoom on;
```